Electrical injection and detection of spin polarization in InSb / ferromagnet nanostructures

Yong-Jae Kim

Dissertation submitted to the Faculty of the
Virginia Polytechnic Institute and State University
in partial fulfillment of the requirements for the degree of

Doctor of Philosophy
in
Physics

Jean J. Heremans, Chair
James R. Heflin
Kyungwha Park
Victoria Soghomonian

July 16, 2012
Blacksburg, Virginia

Keywords: spin, semiconductor, ferromagnetism, spintronics, InSb, CoFe, magnetoresistance, Hall effect, spin Hall effect, lateral spin valve, magnetization

Copyright 2012, Yong-Jae Kim

Electrical injection and detection of spin polarization in InSb / ferromagnet nanostructures

Yong-Jae Kim

(ABSTRACT)

We present studies of the electical detection of spin injection and transport in InSb/CoFe heterostructures. As a narrow gap semiconductor, InSb has a high mobility and strong spin-orbit interaction. Using ferromagnetic CoFe, lateral InSb/CoFe devices are fabricated by semiconductor processing techniques. The saturation magnetizations of various CoFe electrodes with different widths are calculated from Hall measurements in which the fringing fields of the CoFe electrodes are detected. A magnetic model provides reasonable estimation of the saturation magnetization for μm scale geometries. The interface magnetoresistance measurements of InSb/CoFe thin film layered structures present a unique peak at low field, having a symmetric behavior in magnetic field with a critical field H_c and a strong temperature dependence. We attribute our signal to a ferromagnetic phase in the InSb induced by spin injection. In a non-local lateral spin valve measurement, we observed the following. Firstly, H_c of the lateral spin valve signals is identical to H_c of interface magnetoresistance signals. Secondly, the non-local lateral spin valve signals are strongly dependent on temperature, which is also a unique characteristic magnetoresistance. Thirdly, the signals are tunable in response to an applied injector bias. Lastly, the signals are dependent on the exact interfaces. Based on these observations, the detected signals may be considered as spin current signals. The Hall and magnetoresistance signals are measured locally and non-locally in InSb/CoFe Hall devices. The non-local magnetoresistance signals exhibit asymmetric behavior in applied magnetic field which are considered as signatures of spin phenomena. The non-local Hall signals present switching behavior with the CoFe magnetization switching at the coercive field. The non-local Hall signals in a perpendicular field show H_c, similarly seen in non-local lateral spin valves. Inverse spin Hall effect measurements with tilted magnetic fields show an in-plane magnetic field dependence in non-local type Hall signal and a perpendicular magnetic field dependence in the local Hall measurement. We have found that the signal can have its origin in a spin current from our observation of H_c and hysteresis in the magnetization traces. As yet, the spin current transport mechanism is unknown.

Dedication

I dedicate this dissertation to my parents who have always supported and encouraged me with unconditional love. I am thankful to them for being with me on each and every step of my life. My father is the one who is happy with my accomplishment more than anyone else. I miss him so much. My mother always encouraged me to have a positive attitude and stay strong in the face of difficult tasks. I also dedicate this dissertation to my sister, Yongah Kim, and her husband, Sejin Kim, for their support. They have taken care of our family in hard times. Most of all, I dedicate my Ph.D. dissertation to my wife, Hyunmi Kang and my baby, Henry.

Acknowledgments

I wish to express my gratitude to my advisor Dr. Jean J. Heremans for help and guidance. I am thankful to him for his insightful advice and suggestions. He is a great teacher and a role model to me in physics and in life. I would like to thank Dr. Victoria Soghomonian for giving me generous help whenever I needed it, and taking care of me to be a successful graduate student. I am grateful to Martin Rudolph with whom I worked during my research. The time I have spent with him and what I have learned from him are priceless. I am thankful to Dr. Ray Kallaher for training me and leading me to valuable results. I feel myself very lucky that I got very friendly colleagues. I am thankful to Yao Zhang for being very helpful, providing keen insight and valuable advice. I also thank Dr. Robert Lillianfeld for much help and many comment. I would like to thank my lab mates, Qifan Yuan, Lingling Xu and Shaola Ren for useful ideas at group meetings. They are always very kind and considerate to me. In addition, I am thankful to Hyunhang Park for giving me broad interests in various fields of physics and philosophy. Lastly, I would like to acknowledge support from the Department of Energy grant DE-FG02-08ER46532.

Contents

1 Introduction **1**

1.1 Review of Semiconductor Spintronics 1

1.2 Principles of Non-Local Lateral Spin Valve 7

1.3 Thin Film InSb 14

2 Experimental Details **21**

2.1 Sample Fabrication Techniques 21

2.2 Device Fabrication-Lateral Spin Valve 25

2.3 Experimental Setup 28

3 Magnetic Characteristics of $Co_{60}Fe_{40}$ **30**

3.1 Device Design and Fabrication 30

3.2 Sensing Fringing Field 32

3.3 Saturation Magnetization 32

4 Interface Magnetoresistance in InSb/CoFe **36**

4.1 Interface Magnetoresistance with In-Plane Rotation 36

4.1.1 Device Structure 36

4.1.2 Interface Magnetoresistance 38

4.1.3 In-Plane Angle Rotation 42

4.1.4 Temperature Dependence 49
4.2 Ferromagnetic Phase Model 49

5 Non-Local Detection of Spin Transport in InSb/CoFe Lateral Spin Valves 53

5.1 Device Fabrication 53
5.2 Non-Local Lateral Spin Valve Measurements 54
5.2.1 Current Dependence 59
5.2.2 Tilting Angle Dependence 63
5.2.3 Temperature Dependence 64
5.2.4 Bias Dependence 64
5.3 Spin Current 68

6 Spin Transport in InSb Hall Devices with CoFe Electrodes 73

6.1 InSb/CoFe Spin Transport I 73
6.1.1 Device Design and Fabrication I 73
6.1.2 Hall Measurement with In-Plane Field 74
6.1.3 Magnetoresistance Measurement with Perpendicular Field . . 78
6.2 InSb/CoFe Spin Transport II 78
6.2.1 Device Design and Fabrication II 78
6.2.2 Hall Measurement with In-Plane Field 82
6.2.3 Magnetoresistance Measurement with In-Plane Field 85
6.2.4 Hall Measurement with Perpendicular Field 88

7 Inverse Spin Hall Effect in InSb with CoFe Electrodes 91

7.1 Device Design and Fabrication 91
7.2 Inverse Spin Hall Effect Measurement 94

7.2.1 Hall Measurement with In-Plane Field 94
7.2.2 Hall Measurement with Tilted Field 94
7.2.3 Relation to the Inverse Spin Hall Effect 96

8 Summary 98

List of Figures

1.1 Schematic diagram of electron transport in Giant Magnetoresistance (GMR) structure (Ref. [1]) 2

1.2 Schematic diagram of magnetic tunnel juction (MTJ). (Ref. [1]) . . . 3

1.3 Schematic diagram of spin field effect transistor (spin-FET). (Ref. [13]) 4

1.4 Schematic electron density of states of normal metal and ferromagnetic metal showing one spin type majority at the Fermi level. (Ref. [1]) . 5

1.5 (a) Schematic N/F lateral spin valve structure with non-local measurement configuration. (b) Schematic electron density of states. (Ref. [17]) 8

1.6 Schematic non-local signal of N/F lateral spin valve with in-plane magnetic field H_y. The magnetization states of F1 and F2 are indicated with pairs of arrows (black). Blue (red) solid line stands for the signal with forward (backward) sweep as indicated with blue (red) arrow. . 11

1.7 Schematic diagram of lateral spin valve including junction connection.(Ref. [19]) 12

1.8 Three types of InSb film layer structure (t:thickness, UD: undoped, and N_D: Te doping.) The active layer is highlighted with red box. (Ref. [23]) 14

1.9 Quantum interference of time reversed paths of electron with perpendicular magnetic field (left). Schematic graph of typical antilocalization. Spin-orbit scattering time τ_{SO} and phase coherence time τ_ϕ is extracted from graph shape (right). 16

1.10 Antilocalization MR measurements in type A, B and C InSb films. Spin-orbit scattering time τ_{SO} and phase coherence time τ_ϕ are extracted from graph shape. (Ref. [23]) 17

1.11 Main panel: the spin coherence times τ_{SO} vs T, extracted from data of Fig. 1.10. Data fit to HLN theory, Eq. 1.24. The dashed lines indicate average τ_{SO} values with phase coherence time τ_ϕ and the spin coherence length in the parentheses. Inset: the phase coherence times τ_ϕ vs T. The dashed line is the $1/T$ fit. (Ref. [23]) 19

2.1 Micrograph of InSb/CoFe lateral spin valve. The width of InSb is 18 μm. The width of CoFe bars: the wide is 1000 nm and the narrow is 200 nm. The thickness of CoFe bar is 55 nm and the thickness of SiO is 1.2 μm 25

2.2 Schematic fabrication procedure of the InSb/CoFe lateral spin valve. The details of photolithography, electron beam lithography and thermal evaporation steps are described in the text. 26

2.3 (a) Schematic illustration of tilting of sample. (b) Operation of the tilting probe controlled mechanically by tension of a wire (indicated). 27

2.4 Block diagram of experimental setup. Solid (Dashed) lines indicate GPIB (electric) signals. 29

3.1 (a) Micrograph of InSb Hall device with two CoFe bars. (b) Schematic Hall device and lithographic dimensions. (c) Sideview of device indicating fringing field profile from the edge of the CoFe bar. 31

3.2 (a) Hall measurement performed in the Hall cross with the two CoFe bars. Applied current is 1 μA and the temperature is 1.3 K. (b) Hall measurement in Hall cross without the CoFe bars. 33

4.1 (a) Micrograph of type A InSb/CoFe spin valve geometry. (b) Modified DIP header allowing in plane rotation of the external magnetic field. (c) Schematic of the interface MR measurement configuration. . 37

4.2 (a) I-V traces at 1.3 K on narrow CoFe electrode and (b) wide CoFe electrode. Both (a) and (b) present ohmic behaviors with small curvature. 39

4.3 (a) I-V traces at 1.3-3.9 K on narrow CoFe bar and(b) wide CoFe bar. Both (a) and (b) present no temperature dependence. The data are offset for clarity. 40

4.4 Interface MR measurement with blue and red indicating opposing magnetic sweep directions for (a) narrow and (b) wide CoFe bars. . . 41

4.5 (a) Angle dependence measured at 2.0 K. (b) Signal amplitude ΔR vs θ of the traces in (a). 43

4.6 Polar plot of ΔR of the interface between the narrow CoFe electrode and the InSb layer, at 2.0 K. The hard axis lies along the 90° to 270° axis. 44

4.7 Interface MR of the 200 wide nm CoFe bar at 2.5 K (a), and at 3.0 K (b). 45

4.8 Interface MR of the 1000 nm wide CoFe bar in the temperature range 1.28-1.35 K (a), and at 2.0 K (b). 46

4.9 Interface MR of the 1000 nm wide CoFe bar at 2.5 K (a), and at 3.0 K (b). 47

4.10 Temperature dependence of interface MR for narrow (a) and wide (b) CoFe bars with θ=0. 48

4.11 For the narrow and the wide CoFe electrodes, extracted signal amplitude (ΔR) and critical H field (H_c) values from Fig. 4.10 are plotted versus temperature. Linear fits are indicated with red dashed lines. . 50

4.12 The ferromagnetic phase model. The MR result of the narrow CoFe bar with the CoFe magnetizations (M) (white arrows), the existence of ferromagnetic phase (black cross) and magnetic fields (purple arrows). At low fields ($H < 300$ Oe), a ferromagnetic phase is induced in the InSb. Insets: The configurations when the hysteresis the MR signal appears. 52

5.1 (a) Micrograph of type C InSb/CoFe LSV. The width of InSb is 18 μm. (b) CoFe ferromagnet electrode geometry. (c) Dimensions of the CoFe electrode and seperation distance, all in nm. Non-local measurement configuration, showing the near (d) and far (e) detector locations. The wide CoFe electrode is 1000 nm in width, and the narrow one, 200 nm. The thickness of the CoFe electrode is 55 nm, while the thickness of the SiO layer is 1.2 μm. 55

5.2 (a) Micrograph of type C InSb/CoFe later spin valve. The width of the InSb is 18 μm. (b) The non-local measurement is performed at 1.3 K and the applied current is 10 μA. 56

5.3 Micrograph of type A InSb/CoFe later spin valve. The width of the InSb is 18 μm. The measurement is performed at 1.3 K and the applied current is 10 μm. 56

5.4 (a) Non-local measurement result of InSb/CoFe LSV with 0.8 μm separation shows two state signal and hysteretic peaks. (b) The signal disappears in 1.8 μm separation spin valve. 58

5.5 Non-local spin valve signal with type C InSb film with varying CoFe electrode separations. Geometry of this device is depicted in Fig. 5.2 (a). The signal amplitudes do not appear to depend on the separations. Upper graph, the wide CoFe electrodes are used as injectors, while the narrow electrodes inject. In the upper graph, the induced voltage is measured at the narrow electrode, in the lower graph at the wide electrode. 60

5.6 Non-local spin valve signal for type A InSb device with wide CoFe injector (a) and narrow CoFe injector (b). The signal amplitudes are not dependent on the separations. In the upper graph, the induced voltage is measured at the narrow electrode, in the lower, at the wide electrode. A current of 10 μA is applied, but due to the higher interface resistance (InSb/CoFe), the effective current values are 6.06 μA for the wide CoFe electrode and 4.85 μA for the narrow one. 61

5.7 Non-Local spin valve signal with three different applied current on type C device. Data is offset for clarity. 62

5.8 Schematic diagram showing the mechanism of tilting the sample to obtain varying out of plane magnetic fields, as well as measurement configuration. 63

5.9 (a) Tilting angle dependence on LSV signal of type A device (1.5 μm separation) and (b) type C device (1.0 μm separation). In (a), the magnetization of the CoFe is allowed to vary, in addition to the tilt angle, resulting in almost symmetric behavior. In (b), the magnetization of CoFe is fixed, and we observe a non-symmetric behavior arising from varying the spin precession axis as a function of tile angle. . . . 65

5.10 (a) Temperature dependence of the type C InSb/CoFe spin valve signal. Signal amplitude variation as a function of temperature, ΔR_s vs T (b) and H_c vs T (c). In both (b) and (c), the MR signal amplitude decrease as T increases, with an extrapolated T value of ~ 3.5 K. . . 66

5.11 (a) Micrograph of type C LSV with bias configuration as described. I-V trace of the interface; (b) narrow CoFe bar of the 0.8 μm LSV, and (c) wide CoFe bar of the 1.0 μm LSV. 67

5.12 (a) Non-local signal of type C InSb LSV separated by 0.8 μm. Narrow CoFe bar (200 nm) injector is biased at 125 mV. (b) Signal amplitude versus applied DC bias voltage. Inset: magnification at low V_{bias}. . . . 69

5.13 Non-local signal of type C InSb with 1.0 μm separation LSV. Using the wide CoFe electrode (500 nm) as injector, several DC bias voltages are applied to InSb/CoFe injector interface, and resulting MR signals plotted. Data is offset for clarity. 70

5.14 Variation of ΔR_s as a function of bias voltage. (a) $R_{\text{baseline}} - R_{H=0}$ versus V_{bias}. (b) $R_{\text{baseline}} - R_{\text{peak}}$ versus V_{bias}. The R_{peak} measured at $\sim$250 Oe and ~ -300 Oe for forward (blue) and backward (red) sweeps, respectively. 71

6.1 (a) Micrograph of the InSb/CoFe spin transport device. The CoFe layer is highlighted with blue color. (b) Lithographic dimensions of the device. 75

6.2 (a) Hall resistance measured in the Hall cross near the CoFe electrode with in-plane external magnetic field. Current I applied through InSb channel under the CoFe layer. (b) Hall measurement at the far Hall cross as a control, 10 μm away from near Hall cross, shows no noticeable signal. Hall slopes are subtracted for clarity. 76

6.3 (a) Hall resistance measured in the Hall cross near the CoFe with in plane external magnetic field. Current I applied through the InSb/CoFe interface. (b) Hall measurement at the far Hall cross as a control, 10 μm away from the near Hall cross, shows no signal. Hall slops are subtracted for clarity. 77

6.4 (a) MR in the InSb channel with a small perpendicular external magnetic field. Current flow under CoFe. WAL signal is suppressed when the CoFe is magnetized. (b) MR in the InSb channel with a small perpendicular external magnetic field. Current applied through the InSb/CoFe interface. 79

6.5 (a) Micrograph of the InSb/CoFe spin transport device patterned by EBL and wet etching. Then a CoFe electrode and Au contact layers are deposited. (b) Schematic of the device with lithographic dimensions. (c) I-V trace of the InSb/CoFe interface. 80

6.6 Schematic of the tilted evaporation. 81

6.7 (a) Hall measurement result in the Hall cross near the CoFe bar with in-plane magnetic field along CoFe bar (Hall slope subtracted). (b) The far Hall cross data is antisymmetrized to remove MR signal. . . . 83

6.8 (a) Local Hall measurement in the Hall cross near CoFe. Current applied through the CoFe/InSb interface. (b) Non-local Hall measurement. Hall slopes are subtracted for clarity. 84

6.9 (a) Comparison of switching fields measured in near Hall cross with different measurement configuration. The switching field of non-local in which current flow through the CoFe is comparable to local Hall signal with current through the CoFe. (b) The subtraction of bottom two traces of (a) shows the difference of the switching fields of local Hall signals with different current applications. 86

6.10 Non-local MR with in-plane H measured at the top contacts (a) and the bottom contacts (b). 87

6.11 (a) Raw data of the non-local MR measured in top contacts and bottom contacts. (b) Signal difference of top contacts and bottom contacts. 89

6.12 Hall resistance under perpendicular magnetic field with magnetized CoFe. CoFe magnetized at in-plane high field which is indicated with white arrows in measurement schematic. 90

7.1 (a) Micrograph of spin Hall device. (b) Lithographic dimensions. (c) Schematic diagram of tilted external magnetic field. (d) I-V data of CoFe/InSb interface. 92

7.2 Spin Hall geometry data with in-plane external magnetic field measured at different Hall crosses; (a) close and (b) far. 93

7.3 Tilting angle ϕ dependence of spin Hall signal measured in different current applications (blue: forward sweep, red: backward sweep). . . 95

7.4 H_{signal} depends on the tilt angle (blue:forward sweep, red:backward sweep and black dashed line: 1/cosϕ fit). 97

List of Tables

1.1 The active-layer transport properties for different InSb film types at T=0.4 K. (Ref. [23]) 15

Chapter 1

Introduction

1.1 Review of Semiconductor Spintronics

For the past century we have witnessed dramatic development in applied physics and engineering, which has been led by fundamental physics research. Particularly, the contributions of condensed matter physics have been remarkable for the electronics industry. The pursuit of technology in electronics is highly competitive among not only companies but also research labs accompanied with the slogan, “The smaller, the faster”. This competition is represented by Moore’s law, in which the rate of growth of integrated circuit components is increased two-fold every 18 months. However, 40 years of law has shrunk devices to tens of nanometers, and the big challenge of working with the quantum effects of electrons has become important. The quantum interference of electron carriers which circuit designers try to manipulate become inevitably significant as the circuit size gets smaller. The spin, a quantum property of electrons and nuclei, has not yet been integrated into the mainstream of charge-based electronics. The fields of condensed matter physics and engineering are at work to utilize the electron spin in conjunction with conventional semiconductor electronics. This relatively new field of study has been coined spintronics. The adoption of spin can offer expansion of information technology from the classical regime to the quantum regime, with the possibility of more degrees of freedom.

Magnetism is an important tool to manipulate the electron spin [1]. As a matter of fact, the field of spintronics was founded when magnetoresistance (MR) was discovered by Lord Kelvin (William Thomson) in 1850 [2]. MR is the effect that the

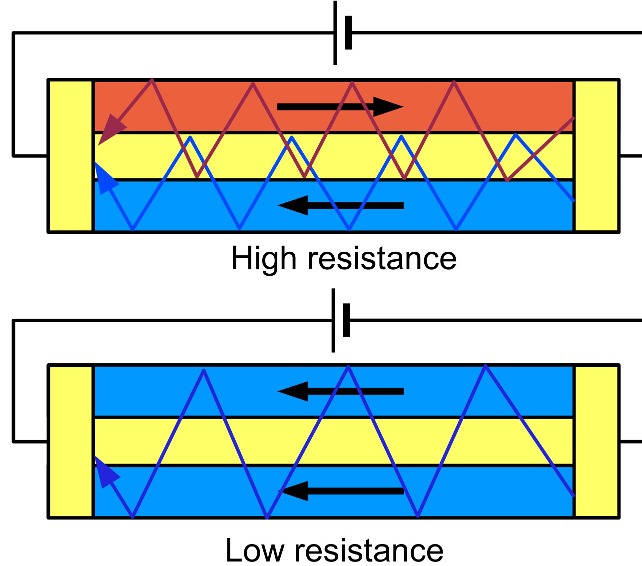

Figure 1.1: Schematic diagram of electron transport in Giant Magnetoresistance (GMR) structure (Ref. [1])

electric resistance changes in response to external magnetic field in solid materials. These days MR is useful to study magnetic and electrical properties of materials. After the Giant Magnetoresistance effect (GMR) [3, 4] was discovered in 1988, there has been remarkable progress in integrating magnetic and non-magnetic materials. It's widely accepted that the discovery of GMR was the beginning of spintronics. In 2007, Albert Fert and Peter Grünberg were awarded the Nobel prize in physics for the discovery of this effect. GMR is the spin-dependent quantum effect observed in alternating layers of non-magnetic and ferromagnetic materials. When the magnetic moments of the ferromagnetic layers are parallel, the material has a low electrical resistance because the spin-dependent carriers have a low scattering rate. For the antiparallel magnetic moments of ferromagnetic layers, the carriers have a high scattering rate, corresponding to a high resistance (Fig. 1.1). The alignment of the magnetic moment of the ferromagnets can be manipulated by an external magnetic field. This layer structure material has a high sensitivity to magnetic fields (100 to 1000 Oe) in changing its resistance [5]. The current can be applied to this structure in two ways, parallel to the interface (current in-plane, CIP) and perpendicular to the interface (current perpendicular-to-plane, CPP).

The common device using GMR is the spin valve where a single non-magnetic metal

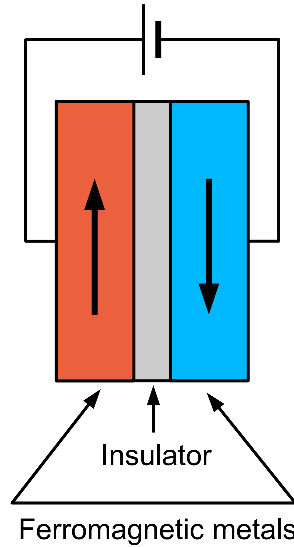

Figure 1.2: Schematic diagram of magnetic tunnel juction (MTJ). (Ref. [1])

layer is sandwiched by two ferromagnetic layers (alloys of iron, nickel and cobalt). One ferromagnetic layer, called the free layer, can change its magnetization at relatively low magnetic field, while the other ferromagnetic layer is a pinned layer which requires a much larger magnetic field to change its magnetization [6]. The pinning typically can be obtained by adding an antiferromagnetic layer on top of the ferromagnetic film. The two layers form an interface that resists the change of the magnetization. This structure helps the GMR spin valve device during room temperature operation.

The magnetic tunnel junction (MTJ) [7, 8] is a spintronic device which uses tunneling magnetoresistance (TMR) [9]. In any tunneling device, charge carriers in conducting layers tunnel through the potential barrier created by very thin insulating layer. If the conducting layers are also ferromagnetic, the carriers are spin-polarized, and the tunneling probability can be manipulated by magnetization of the ferromagnetic layers. The insulating layer does not flip the spin polarization of tunneling electrons. In MTJs, the tunneling resistance shows 20-40% difference between parallel and antiparallel magnetization of pinned (hard) and free (soft) ferromagnetic layers at room temperature. Generally, tunnel devices require lower current than the all metallic GMR devices. In decreasing the size of tunnel devices, the power consumption decreases. However, the impedance of the CPP structure is increased, which causes an

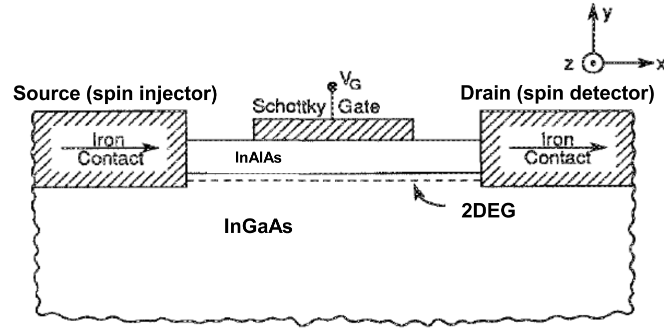

Figure 1.3: Schematic diagram of spin field effect transistor (spin-FET). (Ref. [13])

increase in response time and noise.

Examples of the successful application of GMR and MTJ are magnetic field sensors, hard drive read heads, and magnetic random access memories (MRAM) [10, 11]. However these spintronic devices are metal-based, which have several intrinsic issues that cannot be solved, such as high power consumption, difficulty of conductivity modulation, and fragility for electrostatic discharge caused by the insulating material (for the MTJ device). In addition, the metallic devices have a short spin life time (<10 ps) and small spin coherence length (∼100 nm), which are large obstacles when it comes to manipulating spin-polarized electrons for advanced spin devices. The adoption of semiconductor materials is necessary to overcome these weaknesses. Semiconductors are also good spin transport materials because they have strong spin-orbit interaction (tunability of spin), and longer spin life time and spin coherence length. For example, n-GaAs which is commonly used in many research labs, has a ∼50 ns spin life time and a ∼10 μm spin diffusion length at low temperature (∼10 K) [12]. The first semiconductor spin device proposed was the spin field effect transistor (spin-FET), by Datta and Das in 1990 [13].

Datta and Das' spin-FET became a representative model of semiconductor spintronic devices. The spin-FET has a similar structure to a typical charge-based FET. As shown in Fig. 1.3, the spin-FET is composed of a two-dimensional electron gas (2DEG) narrow gap semiconductor as a carrier transport material, a Schottky gate, and two ferromagnets, one injector (source) and one detector (drain).

The magnetization directions of ferromagnetic injector and detector determines the specific orientation of the spin. As depicted in Fig. 1.4, in ferromagnetic metals such

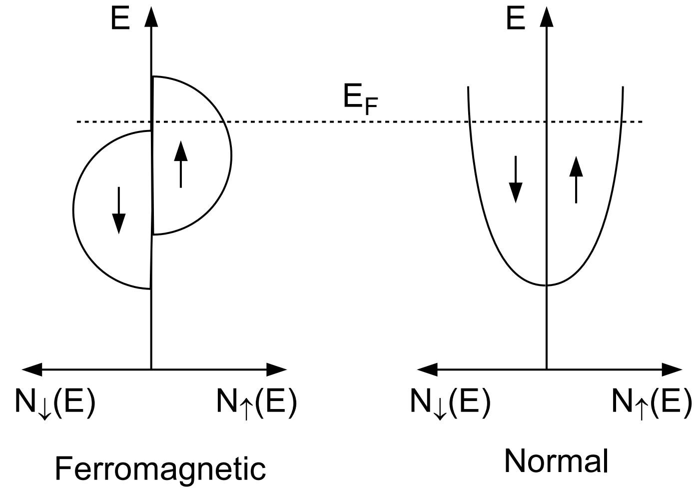

Figure 1.4: Schematic electron density of states of normal metal and ferromagnetic metal showing one spin type majority at the Fermi level. (Ref. [1])

as Fe or Co, the density of states for electrons with one type of spin exceeds that for the other at the Fermi level (E_F).

Above the transport channel, the Schottky gate applies a vertical electric field to the 2DEG channel. The tunable electric field by gate voltage V_G induces an energy splitting between up-spin and down-spin of electrons in the 2DEG channel without external magnetic field. Essentially, the gate is inducing spin-orbit coupling in the 2EDG. The spin transport mechanism in 2DEG channel is described by the Rashba spin-orbit interaction Hamiltonian,

$$H_R = \alpha(\sigma_z k_x - \sigma_x k_z) \tag{1.1}$$

Here, α is spin-orbit coefficient, $\vec{\sigma}$ is spin vector and $\vec{k}$ is wave vector. As shown in Fig. 1.3 the electrons are initially spin polarized in the $\hat{x}$-direction and are injected from the Fe injector into the 2DEG channel with non-zero k_x and k_z=0. The Rashba Hamiltonian can then be simplified to,

$$H_R = \alpha \sigma_z k_x. \tag{1.2}$$

The Rashba spin-orbit coupling leads to $+\hat{z}$ and $-\hat{z}$ polarizations of the electrons with momentum in the $\hat{x}$-direction. Although there is no actual field applied, the effect is similar to that of a magnetic field in the $\hat{z}$-direction with Hamiltonian,

$$H_B = \frac{1}{2} g\mu_B B. \tag{1.3}$$

Comparison of Eq. 1.2 and Eq. 1.3 gives an expression for the effective Rashba magnetic field, denoted, B_R,

$$B_R = \frac{2\alpha k_x}{g\mu_B} \tag{1.4}$$

For the spins initially polarized in $\hat{x}$, B_R induces spin precession along $\hat{z}$. Eventually, the Rashba Hamiltonian causes an energy shift $\pm\alpha k_x$ as shown in Eq. 1.5a and 1.5b. Here m* is effective mass.

$$E(+z \text{ polarized}) = \hbar^2 k_{x1}^2/2m^* - \alpha k_{x1} \tag{1.5a}$$
$$E(-z \text{ polarized}) = \hbar^2 k_{x2}^2/2m^* + \alpha k_{x2} \tag{1.5b}$$

From Eq. 1.5a and 1.5b, we obtain,

$$k_{x1} - k_{x2} = 2m^*\alpha/\hbar^2 \tag{1.6}$$

Thus, the phase shift of the electron spin caused by spin-orbit coupling is given by,

$$\Delta\theta = (k_{x1} - k_{x2})L = 2m^*\alpha L/\hbar^2 \tag{1.7}$$

The spin-orbit coefficient α determines the magnitude of the phase shift. The estimated α for InGaAs/InAlAs heterostructure is $\sim 4\times 10^{-12}$ eVm so that the calculated length scale for a spin flip ($\Delta\theta = \pi$) is L=0.67 μm, which is shorter than the typical mean free path ($\geq$1 μm) of high mobility semiconductors at low temperatures. If we assume ballistic transport for electrons in the 2DEG, the phase shift can be expressed with Larmor frequency ω_L and ballistic spin transport time t in Eq. 1.8.

$$\Delta\theta = \omega_L t = \frac{g\mu_B B_R}{\hbar}\frac{m^* L}{\hbar k_x} \tag{1.8}$$

Upon insertion of Eq. 1.5 into Eq. 1.8, we obtain Eq. 1.7. The resistance modulation can be achieved by changing not only the relative magnetization direction of the Fe injector and detector but also by tuning Schottky gate voltage V_G to change the direction of the spin in transport channel. To realize the fully operational spin-FET that Datta and Das suggested, it is necessary to further study three main obstacles: spin-polarized electron injection into semiconductors with high efficiency, manipulation of spin carriers in semiconductors, and electrical detection of electron spin in semiconductor.

1.2 Principles of Non-Local Lateral Spin Valve

Up until recently, commercialized spintronic devices such as MTJ or GMR spin valve, had vertical structures of ferromagnetic and non-magnetic alternating layers and utilized the two contact CPP geometry. Ultimately, the adoption of spin into the semiconductor industry i.e. semiconductor integrated circuits operating with spin-polarized carriers, cannot be accomplished without the multi-terminal lateral design that most electronic devices use today. In addition, to investigate spin-transport in metals or semiconductors, lateral spin valves (LSV) are advantageous due to their simplicity in fabrication [14–16]. The ferromagnetic and non-magnetic LSV structure is similar to the spin-FET of Datta and Das as described in Sec. 1.1.

The 4-contact non-local LSV structure for spin injection and detection was first suggested and experimentally proven by Johnson and Silsbee [17]. The non-local measurement structure provides the solutions of two problems that the spin-FET has by excluding charge current in the non-magnetic transport channel. As shown in Fig. 1.5(a) the LSV is comprised of two ferromagnetic electrodes with different widths (F1 and F2) on top of a non-magnetic channel (N). One electrode (F1) is used as an injector, where a current source is connected, and the other electrode (F2) is the detector. The connected voltmeter measures a potential difference across the N/F2 interface. The crucial point of this measurement is that there is only spin current I_s in the transport material between F1 and F2 because there are no electrical connections between F1 and F2, so that no net current on the right side of F1 exists. Thus, if there is a non-zero potential reading in the voltmeter, it must be induced by spin current.

The working mechanism of the LSV is as follows [17, 18]. A bias current I (or bias V_0) applied from F1 to N drives the spin polarized current in N across the interface into N with the rate,

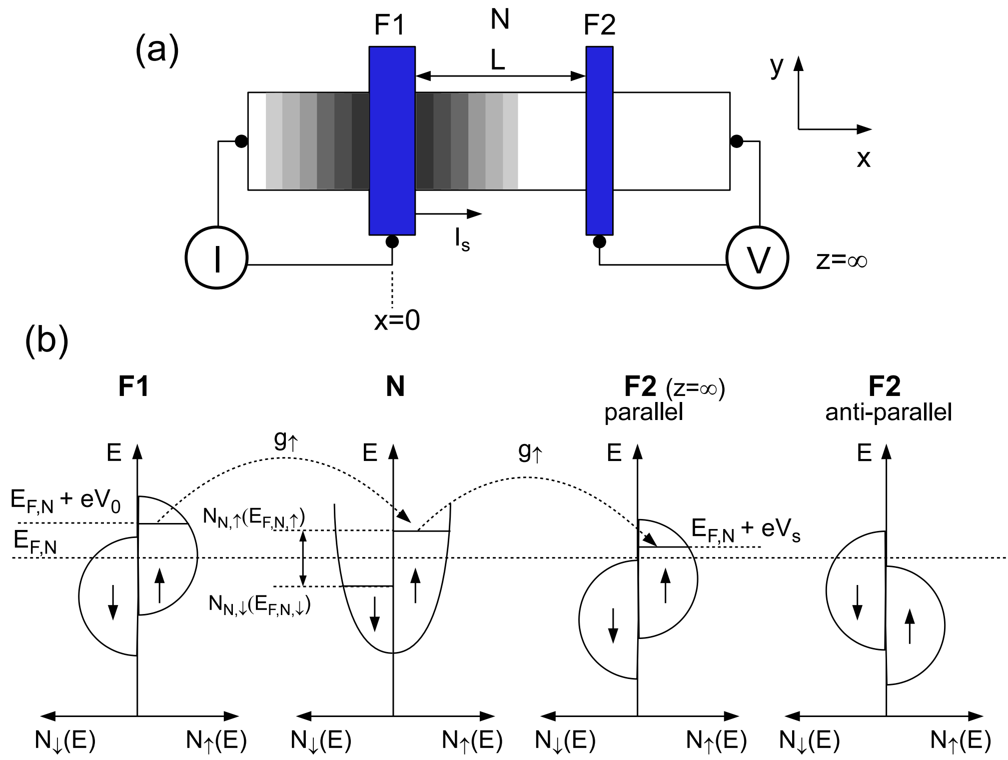

Figure 1.5: (a) Schematic N/F lateral spin valve structure with non-local measurement configuration. (b) Schematic electron density of states. (Ref. [17])

$$I_s = \eta_1 \mu_B \frac{I}{e} \tag{1.9}$$

where η_1 is fractional polarization across the interface, and μ_B is the Bohr magneton. In the steady state, J_s, the spin current density, is balanced with spin relaxation rate $1/\tau_s$, where τ_s is the spin relaxation time. Therefore, the non-equilibrium spin accumulation ($\tilde{M}$) in N is given by,

$$\tilde{M} = \frac{I_s \tau_s}{\text{vol.}} \tag{1.10}$$

In Eq. 1.10, vol.$=A\delta_s$ is the volume occupied by the non-equilibrium spin polarization on the right side of F1 ($x > 0$), where A is the cross-section area of the interface and δ_s is the diffusion length given by $\delta_s = \sqrt{D\tau_s}$. Here D is the electron diffusion constant. The spin accumulation is proportional to the difference of spin subband chemical potential of the majority and minority spin in N, as shown in Eq. 1.11

$$\tilde{M} \propto N_{N,\uparrow}(E_{F,N,\uparrow}) - N_{N,\downarrow}(E_{F,N,\downarrow}) \tag{1.11}$$

where $N_{N,\uparrow}(E_{F,N,\uparrow})$ is the spin-up subband density of states at the chemical potential of spin-up sub-band and $N_{N,\downarrow}(E_{F,N,\downarrow})$ is for spin-down. In the detector ferromagnetic electrode (F2), the high impedance voltmeter reads V_s, the development of the potential due to extra electrons to equilibrate the magnetic energy gain ($\eta_2 \mu_B \tilde{M}/\chi$) in the N/F2 interface by spin accumulation.

$$V_s = \frac{\eta_2 \mu_B}{e} \frac{\tilde{M}}{\chi} \tag{1.12}$$

Here, the χ is the magnetic susceptibility of N, so the ratio $\tilde{M}/\chi$ is defined as the spin accumulation. η_2 is the fractional polarization efficiency in the N/F2 interface. Now, the Eq. 1.12 can be rewritten with $\chi = \mu_B N(E_F)$, $D = [e^2 \rho N(E_F)]^{-1}$ and $\tilde{M} = \eta_1 \mu_B I \tau_s/(e \text{ vol.})$, where ρ is the resistivity of N and $N(E_F)$ is the density of states at the Fermi level. Combining everything, the measured resistance, called transresistance (R_s), in this non-local geometry is given by,

$$R_s = \eta_1 \eta_2 \frac{\rho \delta_s^2}{\text{vol.}} \tag{1.13}$$

For an open geometry, spins exist in vol.=$2A \cdot \delta_s$, i.e. the spin current diffuses along the $\pm\hat{x}$-direction from injector F1.

$$R_s = \eta_1\eta_2\frac{\rho\delta_s}{2A} \tag{1.14}$$

The Eq. 1.14 is valid when the separation L between F1 and F2 is larger than the spin diffusion length $L < \delta_s$. In case of $L > \delta_s$, the spin accumulation decreases exponentially as the distance x from F1 increases. So, eventually the detected R_s at F2 is given by,

$$R_s = \eta_1\eta_2\frac{\rho\delta_s}{2A}e^{-L/\delta_s} \tag{1.15}$$

As described in Fig. 1.5 (b), when the magnetizations of F1 and F2 are parallel, the high impedance voltmeter on F2 reads high V_s, and for anti-parallel magnetizations of electrodes the detected signal is low. Naturally, the case of no spin accumulation will give $V_s = 0$. The magnetizations of F1 and F2 are controlled by an external in-plane magnetic field H_y. At high field (larger than the coercivity of F1 and F2) both electrodes are magnetized in the same direction and at low field (smaller than the coercivity of F1 and F2) the magnetization doesn't change. To achieve the antiparallel magnetization, the coercivity of F1 and F2 should be different, which means the F1 and F2 electrodes flip their magnetization at different magnitudes of the external magnetic field. The coercivity difference can be induced by an anisotropy property of patterned ferromagnetic films, which is called shape anisotropy. As shown in the Fig. 1.6, the different widths of F1 and F2 induces a difference in coercivity, i.e. the wide electrode (F1) has lower switching field than the narrow one (F2). The R_s has two values depending on the parallel and antiparallel states of the electrodes. Fig. 1.6 shows the measured signal for two directions of the magnetic field sweep represented by a blue and a red line.

A different interpretation of the LSV mechanism is suggested by T.Kimura, J.Hamrle, and Y.Otani [19]. They introduce the concept of a spin characteristic resistance for each material (N, F1 and F2). The spin resistance is defined as a measure of how hard it is to mix or separate the spins, which is derived from the spin dependent Boltzmann equation [20]. The spin mixing resistances for N and F are defined as,

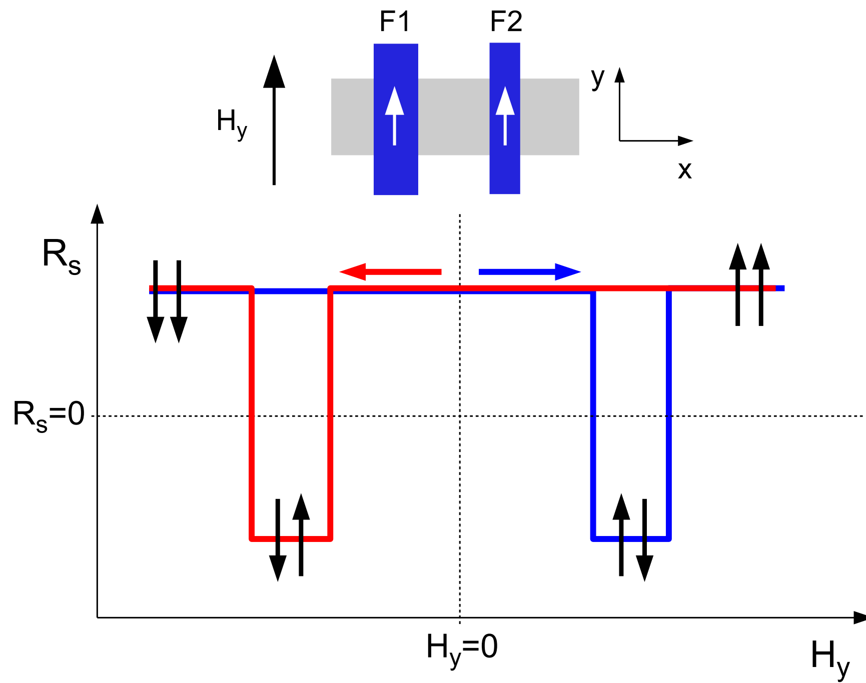

Figure 1.6: Schematic non-local signal of N/F lateral spin valve with in-plane magnetic field H_y. The magnetization states of F1 and F2 are indicated with pairs of arrows (black). Blue (red) solid line stands for the signal with forward (backward) sweep as indicated with blue (red) arrow.

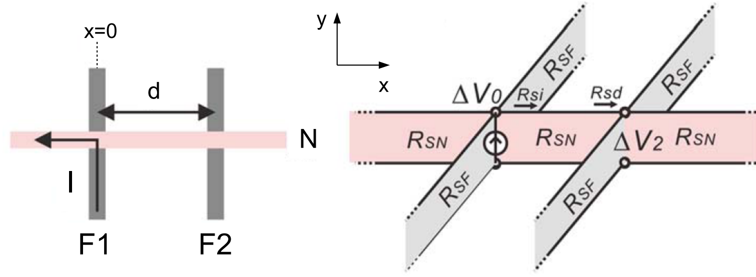

Figure 1.7: Schematic diagram of lateral spin valve including junction connection.(Ref. [19])

$$R_S = \begin{cases} \frac{2\delta_s \rho}{A} & \text{for N} \\ \frac{1}{1-\eta^2}\frac{2\delta_s \rho}{A} & \text{for F} \end{cases} \tag{1.16}$$

The injected spin current I_s into the lateral spin valve diffuses through and obeys a spin dependent Ohmic law, $\Delta V_s = I_s R_{S,T}$, where $R_{S,T}$ is the total R_S of the device.

As illustrated in Fig. 1.7, the spin current I_s from F1 to N is caused by current I with efficiency η_1, $I_s = \eta_1 I$, and induces the potential difference ΔV_0 in the injector junction (x=0). In the detector F2, the spin splitting ΔV_2 is determined by $\Delta V_2 = T\Delta V_0$, where T is the transmission coefficient of the spin signal in the device. At the detector junction, there are four spin resistances playing a role, two $R_{S,N}$ and two $R_{S,F}$. The part of the injected spin current from the injector propagates to the $R_{S,N}$ region ($0 \leq x \leq d$), the $R_{S,N}$ region ($x \geq d$) and also the two vertical $R_{S,F}$ branch across the detector junction. Because the incoming and outgoing spin current is conserved at the junction, it turns out the input spin resistance $R_{S,N}$ ($0 \leq x \leq d$) and the output spin resistance R_{Sd} that is defined by the parallel sum of two $R_{S,F}$ branches and $R_{S,N}(x \geq d)$, $R_{S,d} = (R_{S,N}R_{S,F}/2)/(R_{S,F}/2 + R_{S,N})$, determines the transmission coefficient T as described below,

$$\begin{aligned} T &= \frac{R_{S,d}}{R_{S,N}\sinh(d/\delta_s) + R_{S,d}\cosh(d/\delta_s)} \\ &= \frac{Q}{e^{d/\delta_s}Q + 2\sinh(d/\delta_s)} \end{aligned} \tag{1.17}$$

In the same manner, the total spin resistance $R_{S,T}$ calculated at the injector junction of the device is the parallel sum of $R_{S,N}$, two of $R_{S,F}$ and $R_{S,i}$.

$$R_{S,T} = \left(\frac{1}{R_{S,N}} + \frac{2}{R_{S,F}} + \frac{1}{R_{S,i}} \right)^{-1} \tag{1.18}$$

The $R_{S,i}$ is the output spin resistance through the injector junction, which is given by the series sum of the $R_{S,N}$ and $R_{S,d}$.

$$R_{S,i} = \frac{R_{S,N} \sinh(d/\delta_s) + R_{S,d} \cosh(d/\delta_s)}{R_{S,N} \cosh(d/\delta_s) + R_{S,d} \sinh(d/\delta_s)} R_{S,N} \tag{1.19}$$

using Eq. 1.18 and 1.19 the total spin mixing resistance of the total geometry is calculated as,

$$R_{S,T} = \frac{Q R_{S,N} [e^{d/\delta_s} Q + 2\sinh(d/\delta_s)]}{2[e^{d/\delta_s} Q(2+Q) + 2\sinh(d/\delta_s)} \tag{1.20}$$

where Q is defined as $R_{S,F}/R_{S,N}$. From the results above, the non-local spin valve signal V_s at the detector F2 can be calculated,

$$\Delta V_s = \eta_2 \Delta V_2 = \frac{\eta_2 I_s Q^2 R_{S,N}}{2e^{d/\delta_s}(2+Q) + 4\sinh(d/\delta_s)} \tag{1.21}$$

Therefore, the R_s is given by,

$$R_s = \frac{\Delta V_s}{I} = \frac{\eta_1 \eta_2 Q^2 R_{SN}}{2e^{d/\delta_s}(2+Q) + 4\sinh(d/\delta_s)} \tag{1.22}$$

Here, we assume the spin resistance of N and F are comparable so that $Q = R_{S,N}/R_{S,F} \approx 1$, since the spin diffusion length of N is larger than that of F ($\delta_{s,N} > \delta_{s,F}$), and the resistivity of N is smaller than that of F ($\rho_N < \rho_F$). Also, we assume the separation (d) of F1 and F2 is comparable to the spin diffusion length, $d \approx \delta_s$. From such assumptions, Eq. 1.23 is obtained from Eq. 1.22, which is equivalent to the result of M. Johnson [17], within a factor of 2:

$$R_s = \eta_1 \eta_2 \frac{\delta_s \rho}{4A} e^{-d/\delta_s} \tag{1.23}$$

InSb Cap layer
InSb Active layer
InSb Buffer layer
GaAs (100)

	A	B	C
t (μm)	0.05	0.05	0.05
N_D (10^{22} m^{-3})	15	15	30
t (μm)	1.3	0.6	1.3
N_D (10^{22} m^{-3})	2	3	10
t (μm)	0.2	0.15	0.2
N_D (10^{22} m^{-3})	UD	UD	4

Figure 1.8: Three types of InSb film layer structure (t:thickness, UD: undoped, and N_D: Te doping.) The active layer is highlighted with red box. (Ref. [23])

1.3 Thin Film InSb

The selection of the spin transport material is crucial for the future semiconductor spin-based devices. One promising material is the III-V semiconductor InSb. As a narrow gap (0.236 eV at 4 K) semiconductor, InSb has high mobility (μ) and strong spin-orbit interaction (SOI) [21]. Studies of the spin and phase coherence in InSb films are important in characterizing the spin transport mechanism in InSb. In this section, the characterization of the three types of InSb films, type A, B and C, by Hall measurements and antilocalizaton (AL) [22] analysis of the MR are provided [23]. The films, grown by metal-organic chemical-vapor deposition (MOCVD), have three layers: buffer, cap and active. Figure 1.8 describes the thickness and doping level of each layer in three different films. The 14% lattice mismatch of the interface of InSb and GaAs $\langle 100 \rangle$ substrate builds threading dislocations, which act like n-type dopants and weaken the interface layer mobility. Low doping or no doping in the buffer layer renders it insulating. Additional resistance of the heavily doped cap layer is observed due to the depletion of carriers from the InSb film surface. The average mobility of buffer and the cap layers is significantly lower than that of the active layer, as verified by Hall and MR characterization of films etched to different depths [24]. The assumption made in these measurements is that the active layer gives the dominant contribution in the MR measurement.

Table. 1.1 shows the results of the active layer characterization obtained from Hall and MR measurements at low temperature. The low doped type A film with 1.3 μm thick active layer has high electron mobility (μ) and low electron density (n).

	A	B	C
n (10^{22} m^{-3})	0.6-0.7	2.8-3.1	8.8-9.0
μ (m^2/Vs)	4.0-4.4	3.4-3.5	4.4-4.5
E_F (meV)	8.3-9.2	22.0-23.4	43.5-44.1
λ_F (μm)	0.11	0.07	0.05

Table 1.1: The active-layer transport properties for different InSb film types at T=0.4 K. (Ref. [23])

The type B film results in a lower μ and intermediate n, due to a thinner (0.6 μm) active layer. Similarly to type A, the highly doped thick type C film has high μ and high n. The dependence of μ on temperature T is not monotonic. For type A, B, and C film, the maximum mobility (μ_{max}) is at $T \approx$200 K, $T \approx$300 K and $T \approx$80 K, respectively. The mechanism of suppressing μ at high temperatures can be explained by strong phonon scattering. Coulombic scattering due to ionized dopants is negligible compared to phonon scattering at high temperatures. At low temperature, n-dependent screening partially suppresses Coulombic scattering, and phonon scattering become negligible. Coulombic scattering in the active layer is determined by the competition between increased ionized dopant concentration at higher N_D and increased screening due to the higher n at higher N_D. Therefore, Coulombic scattering is dominant at low temperatures where weak localization (WL) and weak antilocalization (WAL) are observed [22].

To determine the electric and spin properties of each InSb film, such as spin coherence time τ_{SO} and phase coherence time τ_ϕ, the MR with perpendicular external magnetic field is measured at low temperature via standard four-contact low frequency lock-in techniques. The measurement setup is described in detail in Sec. 2.3. Classically, the phase of the conducting electrons are ignored, and the resistivity of the diffusive material is determined by the carrier density and the average elastic scattering time. However, at low temperatures, the phase of the electron may remain intact beyond the elastic scattering time, and a quantum mechanical description of the resistivity is necessary, where one calculates a superposition of all possible electron paths.

The electronic transport under such conditions is considered as quantum diffusive transport [25]. Two important paths to consider are the time-reversed paths depicted in Fig. 1.9. The interference of probability amplitudes of the time-reversed paths provide a quantum correction to the classically estimated resistance. In weak SOI materials, constructive interference contributes to an increase of resistance known

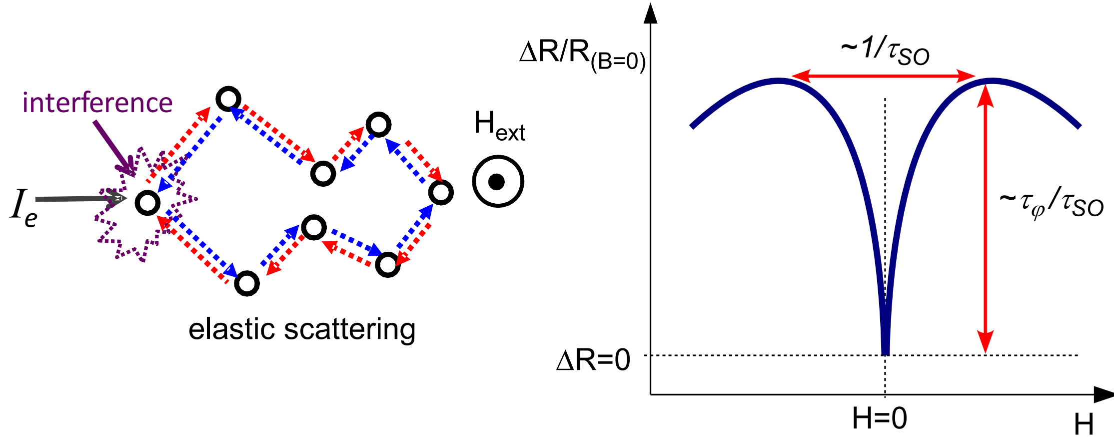

Figure 1.9: Quantum interference of time reversed paths of electron with perpendicular magnetic field (left). Schematic graph of typical antilocalization. Spin-orbit scattering time τ_{SO} and phase coherence time τ_ϕ is extracted from graph shape (right).

as WL. In strong SOI materials such as InSb, destructive interference occurs due to spin rotation over the paths, which contribute an extra phase shift of π. This gives a decrease in resistance, known as AL. In confined structures, such as films and wires, the WL and/or WAL are more prominent due to a larger possibility of time-reversed trajectories. Because they are interference effects, WL and AL are sensitive to Aharanov-Bohm phases, and has a unique dependence on an external magnetic field. The MR measurement is a useful method to extract quantitative information of spin and phase scattering of the electrons. Figure 1.9 presents a schematic MR curve showing AL. The separation of resistance maxima in magnetic field (B) is affected by τ_{SO}. As the separation gets wider, τ_{SO} decreases, indicating an increase in SOI. The depth of the resistance minimum depends on the ratio τ_ϕ/τ_{SO}.

The temperature (T) dependence of the magnetoresistance measurement of InSb films is presented in the Fig. 1.10. Film A, with the lowest dopant density, shows a strong T dependence for the positive MR (AL signal). The signal disappears for $T > 3$ K. In the heavier doped films B and C, the relative broadening of the resistance maxima separation indicates a smaller τ_{SO}, where spin-orbit scattering rate increases as n and E_F increase. The observed AL signal is sensitive to n of the active layer, but not to the thickness of the active layer. For all films, the Fermi velocity v_F and

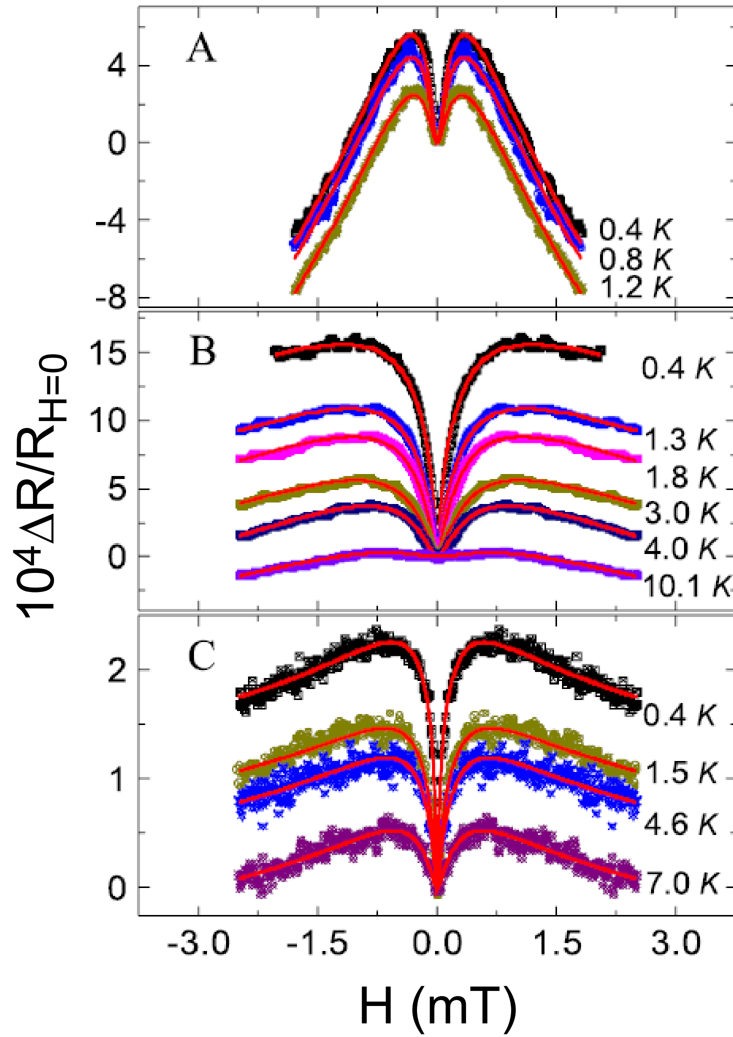

Figure 1.10: Antilocalization MR measurements in type A, B and C InSb films. Spin-orbit scattering time τ_{SO} and phase coherence time τ_{ϕ} are extracted from graph shape. (Ref. [23])

the diffusion constant D are computed by the 3-dimensional relation, $D = \frac{1}{3}v_F^2\tau_p$, where τ_p is the momentum scattering time. Kinematically, the films are regarded as 3-dimensional by the fact that the mobility, mean free path, and Fermi wavelength are shorter than the active layer thickness t. However, the relative values of phase coherence length L_ϕ ($L_\phi = \sqrt{D\tau_\phi}$) and t should also be considered because WL and AL are phase coherence phenomena. The obtained τ_ϕ values (Fig. 1.11 inset) from AL data indicate $L_\phi > t$ for all T at which AL is observed. Although films are kinematically 3-dimensional, the phase coherence is considered as a 2-dimensional phenomena under the condition of $L_\phi > t$ [22, 26, 27]. Therefore, the measured magnetoresistance data is fitted by the two-dimensional theory of Hikami, Larkin and Nagaoka (HLN) [28]. The correction of resistivity for isotropic spin-orbit scattering in perpendicular magnetic field H is given by,

$$\Delta\rho/[\rho^2(H=0)] \approx -\Delta\sigma = \frac{e^2}{2\pi^2\hbar}\left[\Psi\left(\frac{1}{2}+\frac{H_{tr}}{H}\right) + \frac{1}{2}\Psi\left(\frac{1}{2}+\frac{H_\phi}{H}\right) - \frac{3}{2}\Psi\left(\frac{1}{2}+\frac{H_\phi}{H}+\frac{4}{3}\frac{H_{SO}}{H}\right)\right] \tag{1.24}$$

where Ψ is the digamma function and $H_{tr} = \hbar/(4eD\tau_p)$, $H_{SO} = \hbar/(4eD\tau_{SO})$ and $H_\phi = \hbar/(4eD\tau_\phi)$. The Hall measurement and the resistivity at H=0 determines τ_p and D independently (τ_p is the momentum scattering time).

Fig. 1.11 shows the extracted values of τ_{SO} versus T and τ_ϕ versus T (inset). For the measurement temperature range of $0.4 < T < 10$ K, τ_{SO} is not dependent on T and τ_ϕ is dependent on $1/T$. The restricted temperature range for observing AL signal in film A can be explained by the large τ_{SO}, which lowers the ratio τ_ϕ/τ_{SO}. The value τ_{SO} depends strongly on n, where τ_{SO} varies from ~6.5 *ps* in film C with the highest n to ~73 *ps* in film A with the lowest n. In all three InSb films, even in film C with the highest n, $L >1$ μm, and this length scale is easily achievable with current fabrication techniques.

This dissertation explores the results from five types of experiments. InSb device structures, fabrication techniques, and measurement techniques are discussed in Chap. 2. The first experiment is a Hall measurement of InSb with two CoFe bars. Also discussed are the magnetic properties of the CoFe, presented in Chap. 3. The second experiment is an interface MR measurement in InSb with a single CoFe electrode, and where the electromagnetic properties of the InSb/CoFe interface are presented, Chap. 4. The third experiment is the electrical detection of spin injection

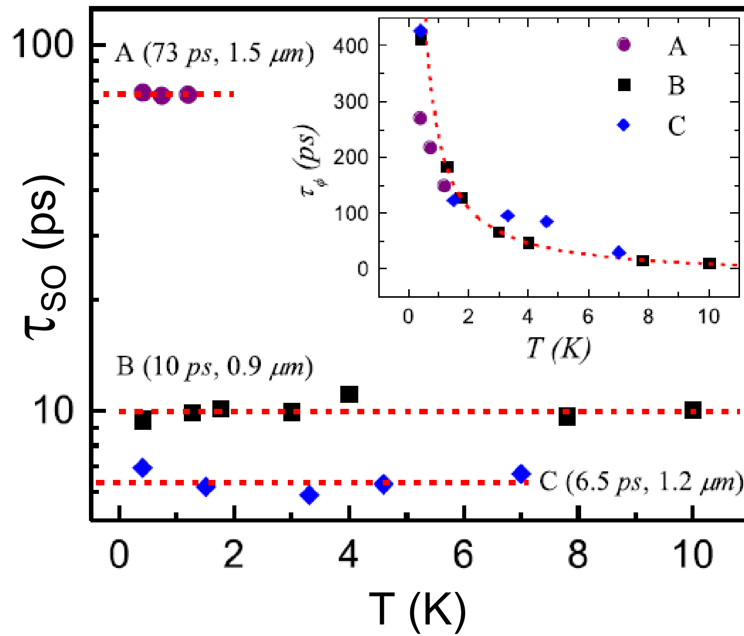

Figure 1.11: Main panel: the spin coherence times τ_{SO} vs T, extracted from data of Fig. 1.10. Data fit to HLN theory, Eq. 1.24. The dashed lines indicate average τ_{SO} values with phase coherence time τ_ϕ and the spin coherence length in the parentheses. Inset: the phase coherence times τ_ϕ vs T. The dashed line is the $1/T$ fit. (Ref. [23])

in an InSb/CoFe lateral spin valve geometry. The results from the non-local measurements of lateral spin valves made from type C and type A InSb are presented in Chap. 5. The fourth experiment is a spin transport measurement, where Hall and MR measurements in patterned InSb with a CoFe electrode are performed and discussed in Chap. 6. The last experiment addresses measurement of the inverse spin Hall effect. The results in an InSb/CoFe spin Hall device are presented in Chap. 7.

Chapter 2

Experimental Details

In the following sections, device fabrication techniques and experimental details are described. Further, the experimental setup for low temperature magnetotransport measurements are also described.

2.1 Sample Fabrication Techniques

Our previous work on AL in InSb thin films, which showed spin and phase coherence, is critical for the design of spin transport experiments in lateral InSb/CoFe spin devices. The device structure, especially the spacing of two ferromagnetic electrodes, is designed based on the spin coherence length obtained from AL of InSb thin films. In this section, the fabrication processes for InSb devices will be described including nanoscale fabrication techniques which were developed over the past several years in the Heremans group.

Depending on the objectives of experiments different types of devices were fabricated. In their respective chapters, we will discuss the details of each device design. Here we will introduce only the typical fabrication techniques widely used for making metal or semiconductor devices and describe the fabrication procedure for an InSb/CoFe lateral spin valve as an example.

The first step for device fabrication is the preparation of the clean InSb $\sim$2 mm$\times$4 mm chip, obtained by cleaving an InSb wafer. The dimensions of the InSb chip can be modified, depending on the total size of the pattern, but are limited to 19 mm by

7 mm, which is the size of the 14-pin DIP header. The sample is cleaved by scoring the GaAs ⟨100⟩ surface (the back side) of the wafer with a carbide tip. Then the chip is cleaned by soaking it in TCE (trichloroethylene), ACE (acetone) and IPA (isopropyl alcohol) in consecutive order for 3 minutes each to remove organic, ionic, and metallic impurities. Then IPA is sprayed on the chip and room temperature, and nitrogen gas is blown over to dry and remove any large dust particle.

Photolithography is the most common method to transfer patterns onto samples, and we also employ this technique with a Karl Suss MJB 3 instrument. A film of photosenitive material (photoresist) is deposited, and exposed under a shadow mask. After removing the exposed photoresist, the mask pattern remains. Users are easily able to maneuver the alignment between the pattern mask and the sample by looking at the sample under the microscope. On the other hand, a drawback of this method is the relatively large size limit (∼1 μm) of the pattern, due to the UV light interference and diffraction.

Photoresist thin film is formed by spin coating AZ5206E photoresist. Before spinning the sample is glued to the corner of the thin glass slide (18 mm square, 0.18 mm thickness) using AZ5206E photoresist glue because the sample size is too small to mount on the spinner. This also make it convenient to handle the sample without damaging it. Then the glue is dried at room temperature for 5-10 minutes and baked in a 95 °C oven for 15-30 minutes. Next, the surface is fully covered with few drops of AZ5206E photoresist, and then the sample is spun at 4000 rpm (revolution per minute) for 40 seconds. The photoresist film is baked for 30 minutes in 95 °C oven to cure the resist to the optimal sensitivity and consistency. The thickness of AZ5206E film is 0.6 μm with the above spinning parameters. The photoresist thickness is an important factor when deciding the thickness of various deposited films. The deposited films should be thinner than the photoresist otherwise there could be a problem when attempting to remove the photoresist. The UV exposure time is about 15 seconds. Before exposure, the alignment between the mask and the sample is critical, especially in case of transferring multiple patterns. The mask (or photomask) is a glass plate with a patterned iron oxide film on one side so that the UV light only can reach the photoresist through window in the iron oxide. The patterned side of the mask should physically contact the surface of the photoresist. The exposed part of the photoresist changes in chemical structure, so that it becomes more soluble in a developer. The developer for the AZ5206E is AZ351 developer diluted 5 times with water. The sample is soaked in this particular developer for about 15 seconds to develop AZ5206E and submerged in de-ionized water at least 1 minute to wash off the developer. Then the sample is dried by blowing nitrogen gas.

Another widely used pattern transferring method is electron beam lithography (EBL). The pattern writing mechanism of EBL is similar to photolithography. The electron beam breaks the polymer chain of an electron resist, such as PMMA (polymethyl methacrylate), so that a developer can wash out the exposed part. The advantage of this technique is the nanometer scale writing capability (∼30 nm) gained by the small wavelength of the electron beam. Also, there is no need of a pattern mask, as the beam can be controlled by software which allows users freedom for pattern design. The major disadvantage for EBL is the longer exposure time needed. The electron beam writing time is given by the formula below,

$$d \cdot A = t \cdot I \tag{2.1}$$

where t is the exposure time for covering area A with electron dose d and beam current I. A typical value for d is around 200 μC/cm^2 to sufficiently expose PMMA. To deposit a PMMA film, first the sample is glued on a thin glass slide. For EBL the thin glass slide is coated with conducting metal such as gold to drain electrons to ground. The glue for attaching the sample to the glass slide is also conducting, and we use colloidal graphite in isopropanol base.

The sample is dried at room temperature for 5-10 minutes, then baked for 30-40 minutes in a 170 °C oven. 6% PMMA in chlorobenzene solution is spin coated at 7800 rpm for 40 seconds, resulting in a film thickness 0.3 μm and then baked for 6 hours in a 170 °C oven. Before the sample is loaded into the SEM (scanning electron microscope), it is scratched in order to properly locate and orient the pattern under high magnification. The scratch is also convenient for focusing the electron beam precisely. The sample is pumped down below $5{\times}10^{-5}$ Torr in the SEM chamber. The electron beam writing is controlled by NPGS (nanometer pattern generation system) software into which the magnification, beam current, center to center value, line spacing, dose and pattern are entered. The particular pattern for lithography is designed in design CAD (computer-aided design) program, which is linked to NPGS. Once the PMMA has been exposed as desired, the exposed portions of PMMA by developing in MIBK (methyl iso butyl ketone) diluted 3 times with IPA. The established developing time for 6% PMMA is 70 seconds, with subsequent rinsing in IPA for at least 1 minute. The sample is blown dry with nitrogen. The patterned PMMA has an undercut profile because the electron beam is scattered diffusively from the InSb surface.

A pattern can be transferred to an InSb sample after lithography by etching away the exposed InSb. To etch InSb, a solution of 4 parts lactic acid to 1 part nitric acid

is used. The time to etch an InSb film 1.55 μm thick down to the GaAs substrate is between 70 and 100 seconds. The exact etching time is dependent on several factors, such as the size of the pattern, the shape of the pattern, the temperature and the volume of the etchant. Thus, the etching is done in steps so that the progress can be monitored under a microscope to avoid over etching. Due to the anisotropic lattice structure of InSb, the etching profile also depends on the orientation of the pattern with respect to the crystalline axis.

To add layers of other materials on top of the InSb, thin films are deposited by thermal evaporation in ultra high vacuum. All deposited materials used in this dissertation, CoFe, SiO, Cr, and Au, were deposited in an Edwards 306A thermal evaporator. The source material is evaporated in ultra high vacuum by heating up a tungsten boat with a large current. The current value determines the temperature of the source material. The vaporized source particles are condensed on the surface of the sample. The thickness of the evaporated film is monitored by a quartz balance, which measures the shift in resonance frequency of a quartz crystal as the material is deposited. The evaporation process is performed under vacuum of less than 10^{-6} Torr. To evaporate CoFe, an aluminum oxide (Al_2O_3) coated molybdenum (Mo) boat holds a piece of $Co_{60}Fe_{40}$, about 5 mm diameter. The evaporation rate is regulated to about 2 Å/s. The process of SiO and Au deposition is similar to CoFe, except that a tungsten (W) boat is used for these two materials.

To create a pattern of CoFe or any other material on InSb, a lithography step is combined with a film evaporation and lift off step. The material deposited on top of the developed resist is removed by removing the resist, leaving a negative of the pattern on the material. The solvent used to remove PMMA and AZ5206E is acetone. The acetone lift off process consists of three steps: soaking the sample in at room temperature, heating it to 75 °C in acetone, and then placing it again in acetone at room temperature. Each bath lasts for ∼1 hour.

After fabrication, a device must be soldered to a mounting package (DIP header) so that it can be mounted into the measurement apparatus. The sample is connected to a 14-pin DIP header by Au wires soldered with indium. Indium is chosen because it is very stable and conductive at low temperature (0.4 K). It also has a low melting point (156.6 °C) while contacting, which ensure no unwanted thermal annealing of the sample occurs. The soldering temperature is 220-240 °C. The contacted sample is attached to the DIP header using Apiezon N grease, which is also stable at low T.

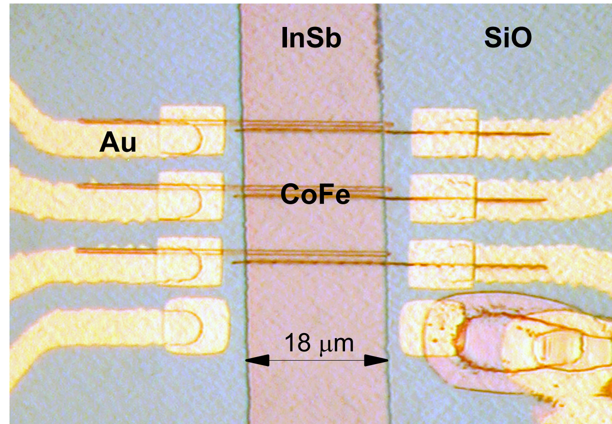

Figure 2.1: Micrograph of InSb/CoFe lateral spin valve. The width of InSb is 18 μm. The width of CoFe bars: the wide is 1000 nm and the narrow is 200 nm. The thickness of CoFe bar is 55 nm and the thickness of SiO is 1.2 μm

2.2 Device Fabrication-Lateral Spin Valve

A LSV device micrograph is shown in Fig. 2.1. Three pairs of CoFe electrodes are deposited on top of InSb which has an insulating SiO window already on it. Au layers for electrical contacts with CoFe come in from the sides. The LSV fabrication process is depicted in Fig 2.2. First, a SiO window is deposited on top of InSb. SiO is a good insulating material at low temperatures and is easy to evaporate. On top of the SiO, an Au contacting pattern with 8 arms is deposited. Six contacts are connected to 3 pairs of CoFe bars and the remaining two contacts are for the alignment process necessary for the EBL. The thickness of the Au is about 55 nm. Before the deposition of the Au, 5 nm of Cr is evaporated on the InSb surface, which aids the ability for Au to stick to the InSb. Next, the CoFe electrodes are deposited on the InSb with connections to the Au contacting arms as shown in Fig. 2.2. The CoFe pattern is defined by EBL to create nanometer size CoFe bars. The electron beam dose used is 235 μC/cm^2 with a current 12 pA. Lastly, 55 nm thick CoFe electrodes are deposited.

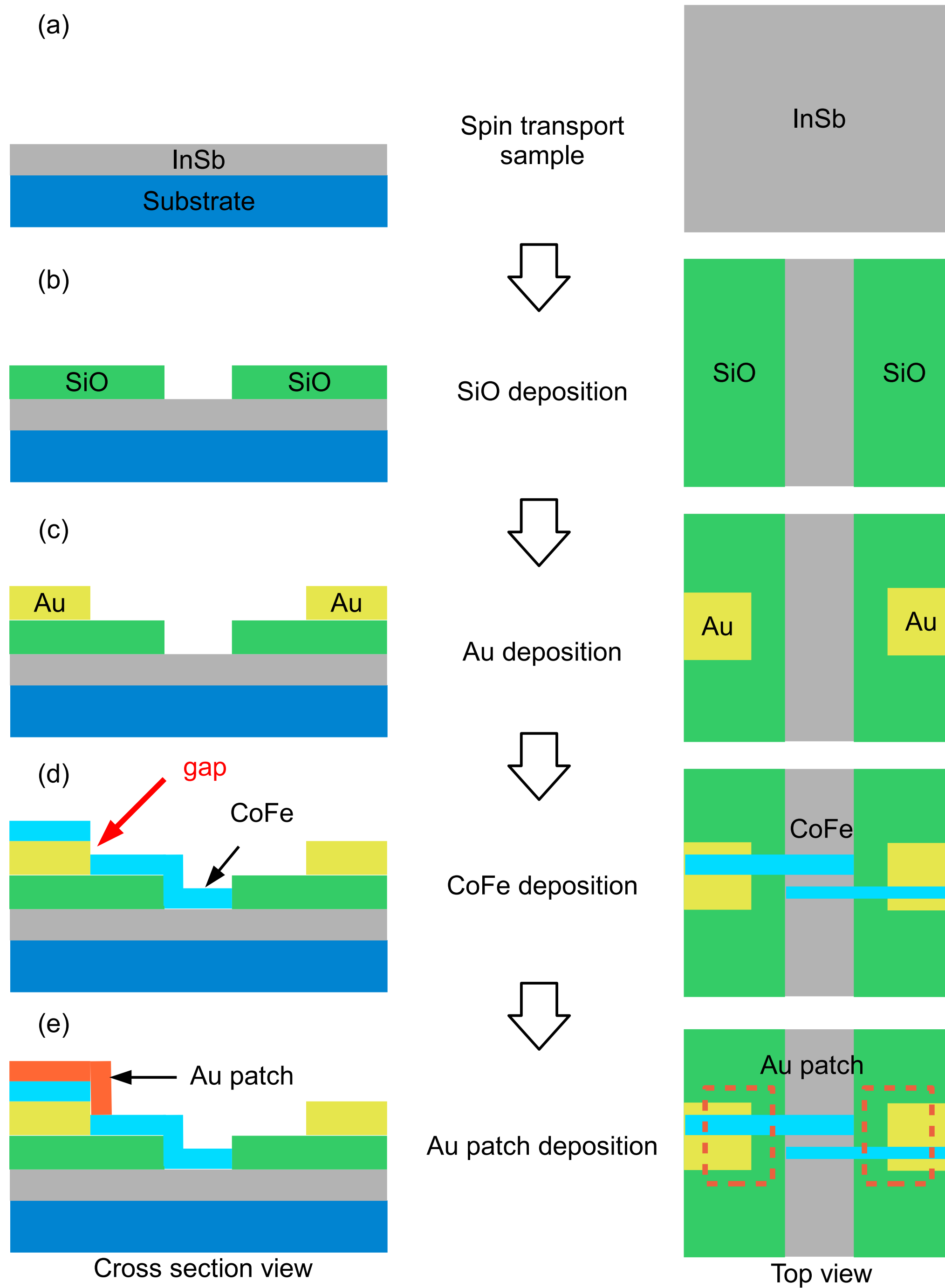

Figure 2.2: Schematic fabrication procedure of the InSb/CoFe lateral spin valve. The details of photolithography, electron beam lithography and thermal evaporation steps are described in the text.

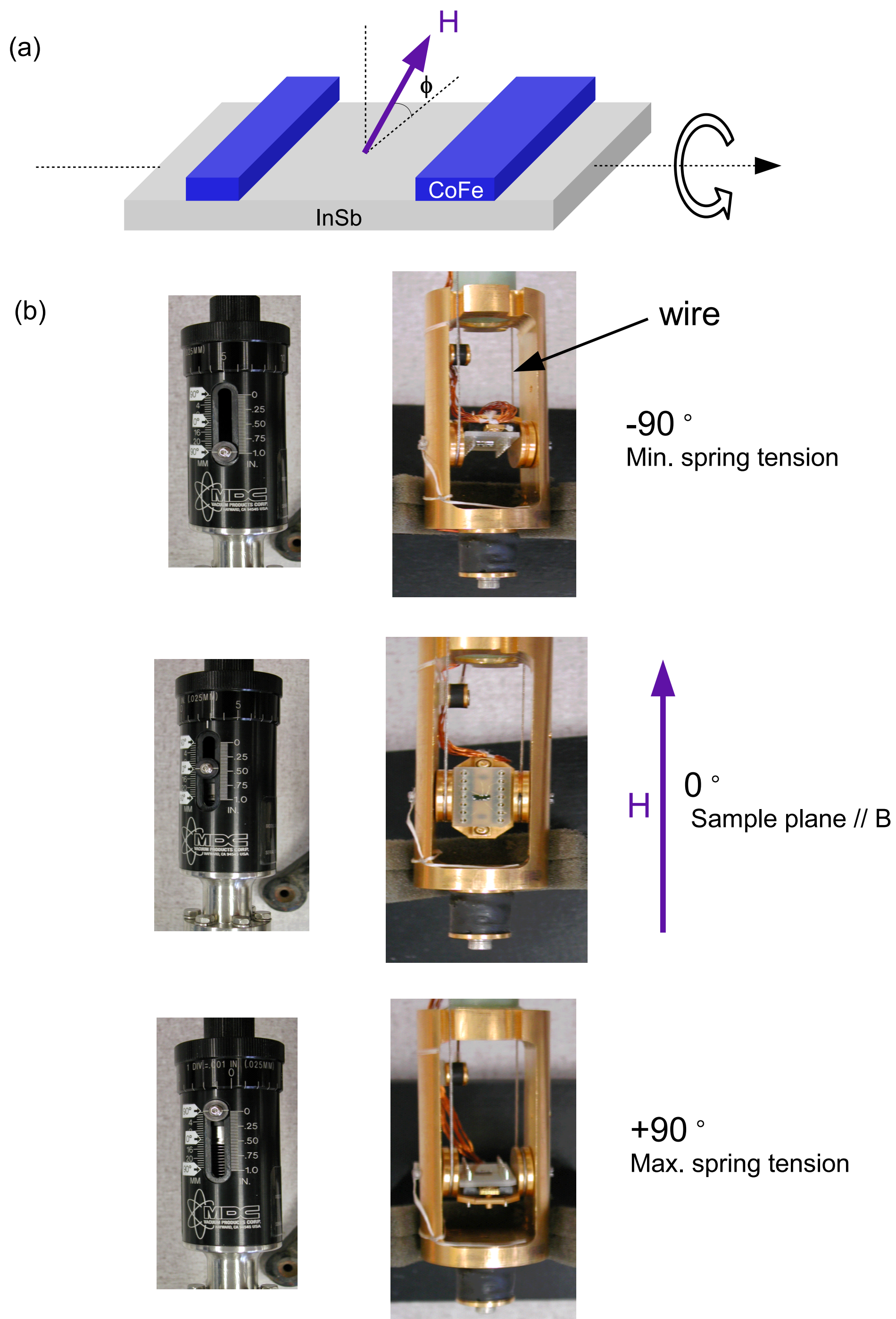

Figure 2.3: (a) Schematic illustration of tilting of sample. (b) Operation of the tilting probe controlled mechanically by tension of a wire (indicated).

2.3 Experimental Setup

The fabricated device is loaded into a tilting probe which can rotate the device around a 180° range, as shown in Fig. 2.3. The sample holder is mechanically rotated so that the external magnetic field direction is tilted with angle ϕ as illustrated in Fig. 2.3 (a). Figure 2.4 describes the experimental setup in block diagram format. ^{4}He cryostat is used to perform low temperature MR characterization. A sample is loaded into the tilting probe. The MR measurement is performed with lockins. AC current is applied from lockin to the sample via a contact box. The superconducting magnet generates a perpendicular magnetic field with respect to the sample, and is controlled by a source meter (Keithley2400). Temperature and DC bias are controlled by a resistance bridge thermometer and a voltage source (Keithley6487), respectively. Voltage signal detected by a lockin is collected in a computer via a multimeter (Keithley2000), as indicated in Fig. 2.4, solid lines. Experimental setup is controlled through a LabView (National Instruments) control software via GPIB (general purpose interface bus) lines.

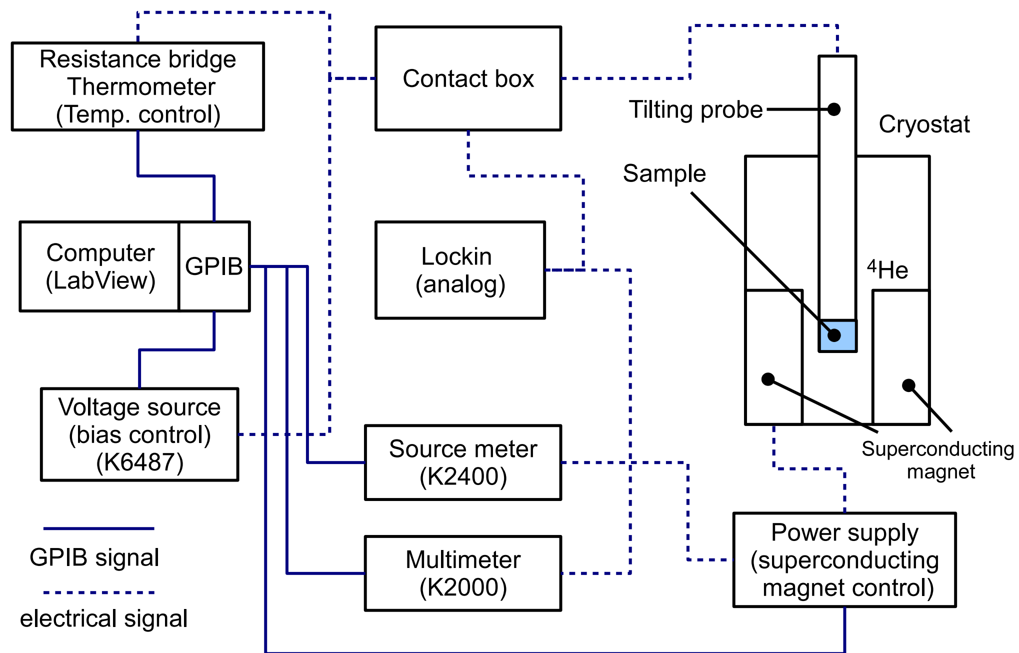

Figure 2.4: Block diagram of experimental setup. Solid (Dashed) lines indicate GPIB (electric) signals.

Chapter 3

Magnetic Characteristics of $Co_{60}Fe_{40}$

To investigate spin phenomena in InSb, the characteristics of spin-polarized current injection must be well understood. We study the magnetic properties of the ferromagnetic material CoFe, so as to better determine its role for spin injection. In addition, the anisotropic properties of the magnetization of the CoFe are important because the direction of spin polarization is determined by the magnetization of CoFe. In this chapter, the saturation magnetizations of various CoFe electrodes with different widths will be calculated from Hall measurements in which the fringing fields of the CoFe electrodes are detected.

3.1 Device Design and Fabrication

The type C InSb film is fabricated into a Hall device, by photolithography and wet etching. Then, two small Hall cross patterns are added by electron beam lithography and etching. The lithographic width of the Hall crosses is 8 μm and the separation of two Hall crosses is 40 μm. Next, two CoFe bars with different widths are deposited on one Hall cross. As depicted in Fig. 3.1(a), the edges of CoFe bars are centered in the Hall cross. The narrow CoFe bar has a width of 200 nm and the wider one has a width of 500 nm. The separation between the two bars is 800 nm and their thickness is 55 nm. These lithographic dimensions are also indicated in Fig. 3.2 (b).

The Hall cross without the CoFe bar is used as a control and senses the Hall signal.

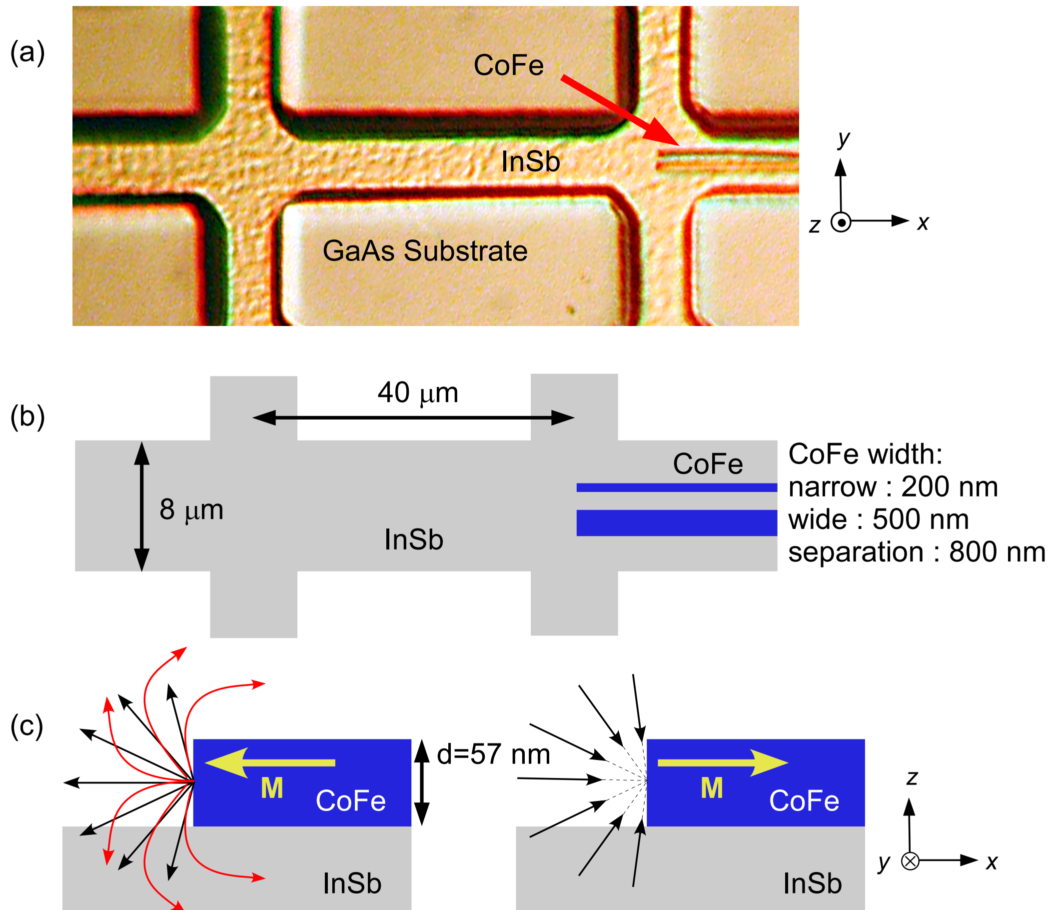

Figure 3.1: (a) Micrograph of InSb Hall device with two CoFe bars. (b) Schematic Hall device and lithographic dimensions. (c) Sideview of device indicating fringing field profile from the edge of the CoFe bar.

For the Hall cross with the CoFe bars, the current passing through the CoFe bars is negligible, as will be shown later, and all the current is assumed to stay in the InSb layer. An in-plane magnetic field is applied along the longitudinal direction of the CoFe bars so that their magnetization state can be manipulated.

3.2 Sensing Fringing Field

The Hall measurement is a well-known tool to measure materials properties, such as carrier densities of electrons or holes. Also, as a magnetometer, Hall devices sense magnetic fields and/or currents. In this section, the Hall effect in InSb is used to sense the fringing fields of the CoFe bars. The measurement senses the $\hat{z}$-component of the fringing field B_z, as depicted in Fig. 3.1 (c). Fig. 3.2 (a), and (b) present the signals for the Hall cross with and without the CoFe bars, in response to the application of an in-plane external magnetic field. The residual Hall slopes are subtracted for clarity. The control Hall cross does not show any switching. In the presence of CoFe bars, a 3-state Hall signal is observed due to the perpendicular fringing fields induced by the magnetized bars, indicating a 3-state magnetization ($\rightrightarrows$, $\leftrightarrows$, and $\leftleftarrows$). The size difference of the CoFe bars allows access to the antiparallel state as the narrow bar has a larger coercive field due to shape anisotropy [29, 30]. Indeed in-plane coercive fields are 900 Oe and 630 Oe for narrow and wide CoFe bars, respectively. The fringing fields are 3 Oe and 8 Oe for narrow and wide, respectively, which are calculated by the following Hall relations.

$$\frac{V_H}{I} = \frac{B}{net} \tag{3.1}$$

$$\langle B_z \rangle \approx \triangle R_{xy}(net) \tag{3.2}$$

In type C InSb film, the carrier density $n = 8.9 \times 10^{22}\ m^{-3}$ and the thickness of InSb active layer is t=1.3 μm.

3.3 Saturation Magnetization

The saturation magnetization of the CoFe bar is calculated based on the assumption that the CoFe is a single domain at its endpoint when the magnetization is saturated,

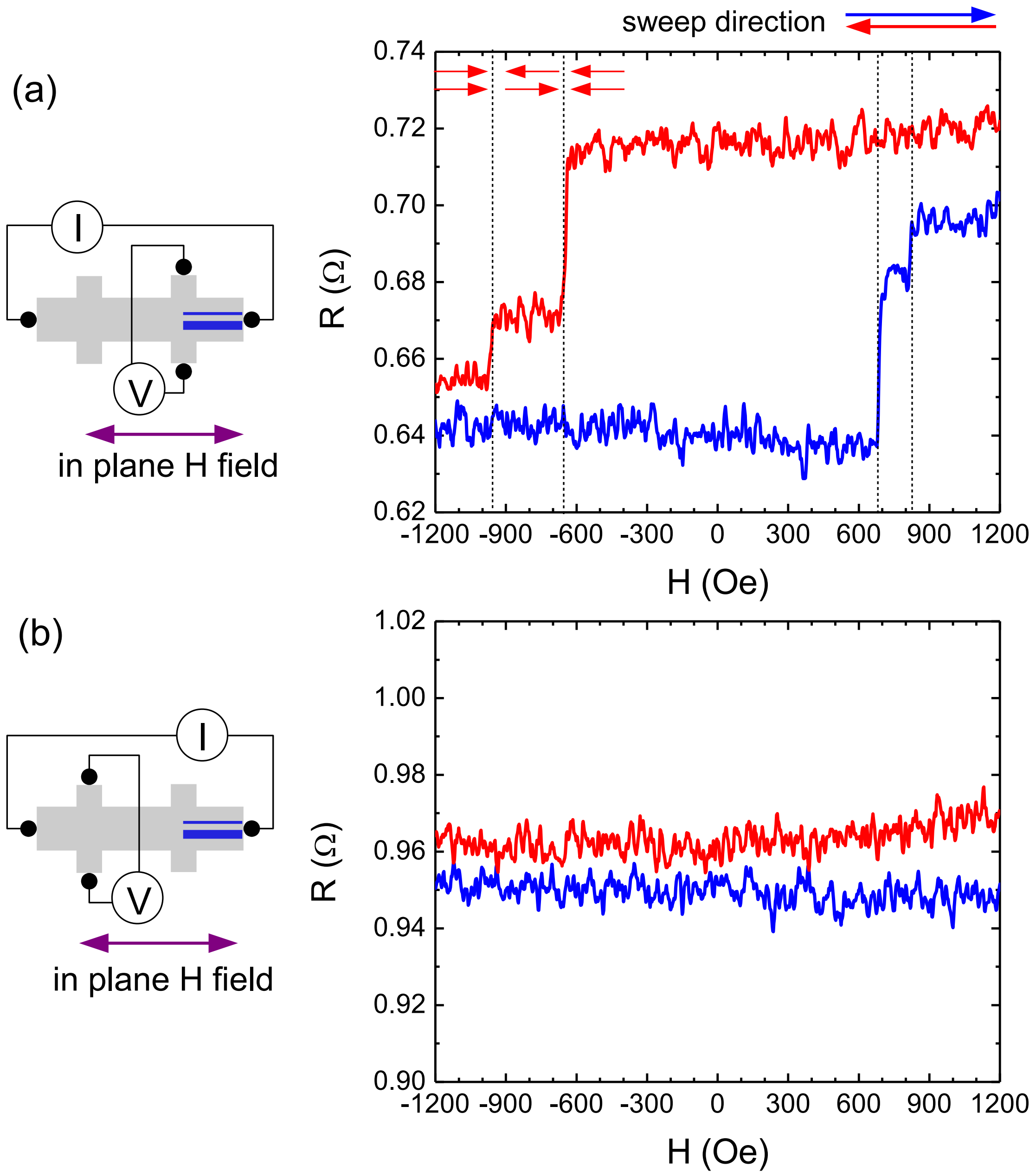

Figure 3.2: (a) Hall measurement performed in the Hall cross with the two CoFe bars. Applied current is 1 μA and the temperature is 1.3 K. (b) Hall measurement in Hall cross without the CoFe bars.

$\vec{M} = \pm M_s \hat{x}$. At the edge of the CoFe bar magnetic field lines may be visualized, as depicted in Fig. 3.1(b). The black lines indicated the idealized field line distribution while the red lines represent the experimentally realized field lines. In this model, the effect of the fringing fields generated from the other edge of the CoFe bar is neglected, as it is at far distance from the Hall cross. For simplification, it is assumed that magnetic poles are concentrated in a line, $d/2$ (d: CoFe thickness) away from the InSb surface, along the edge of CoFe bar. Accordingly, the fringing field can be written as,

$$B_z(x) = \frac{\mu_0}{4\pi} \frac{2\lambda_m w z}{x^2 + z^2} \tag{3.3}$$

where $\lambda_m = M_s d$ is the line magnetic charge density, and w is width of the CoFe bar. The average magnetic field in the Hall cross determines ΔR_{xy}. The averaged B_z along the vertical line of the InSb active layer (1.3 μm) is considered as the total fringing field affecting the Hall cross. The average $\bar{B}_z$ at the line of point x in the InSb film is given by

$$\bar{B}_z(x) = \frac{\displaystyle\int \frac{\mu_0}{4\pi} \frac{2\lambda_m w z}{x^2 + z^2} dz}{\displaystyle\int dz} \tag{3.4}$$

The measured Hall resistance change is equivalent to the effect of the averaged $\bar{B}_z$ in Hall cross area,

$$\Delta R_{xy} = \frac{\Delta \bar{B}_z}{net} = \frac{2\Phi_m}{net \displaystyle\int da} \tag{3.5}$$

where $\Phi_m = \int \bar{B}_z da'$ is the magnetic flux in the Hall cross area. The factor 2 is because $\bar{B}_z$ flips such that $\Delta \bar{B}_z = \bar{B}_z - (-\bar{B}_z) = 2\bar{B}_z$. The area da' where Φ_m contributes is defined as (width of CoFe $\times$ Hall cross width/2), because CoFe bar edge is located in the center of the Hall cross. The area da is the total Hall cross dimension, 5$\times$5 μm^2. Thus, Eq. 3.5 is written as,

$$\Delta R_{xy} = \frac{\Delta \bar{B}_z}{net} = \frac{2\int\int da' dz \frac{\mu_0}{4\pi}\frac{2\lambda_m wz}{x^2+z^2}}{net\int da} \tag{3.6}$$

The measured ΔR_{xy} for the wide and the narrow CoFe bars are 0.044 Ω and 0.016 Ω, respectively. The obtained saturation magnetization of the narrow and the wide CoFe bars are $M_{\mathrm{s,wide}} = 1.4\times10^6$ A/m (1400 emu/cm^3) and $M_{\mathrm{s,narrow}} = 1.3\times10^6$ A/m (1300 emu/cm^3), respectively. The magnetic moment of $Co_{60}Fe_{40}$ alloy is given by $\mu = 2.25\mu_B$ from superconductor-insulator-ferromagnet spin polarization measurements [31], where μ_B is the Bohr magneton. As a bcc structure with $a = 2.82$ Å, CoFe has 2 atoms per cell, thereby the magnetic moment density is $n = 8.5\times10^{28}$ m^3. Using the relation $M_s = n\mu$, the saturation magnetization of $Co_{60}Fe_{40}$ is 1.77×10^6 A/m (1770 emu/cm^3). In addition, the calculated saturation magnetization of $Co_{50}Fe_{50}$ is 1800 emu/cm^3 [32]. The saturation magnetization of the CoFe bars presents a ∼25% smaller value than the magnetization saturation obtained from the magnetic moment of CoFe. The discrepancies are due to the fact that we approximated the fringing field using an infinitely wide magnetic bar. In Sec. 6.1.2, the same measurement is performed with an 8 μm wide CoFe bar. The calculated saturation magnetization is then 1.7×10^6 A/m (1700 emu/cm^3). However, in Sec. 6.2.2, the obtained saturation magnetization from the same InSb structure with the same width CoFe electrode is 0.7×10^6 A/m (700 emu/cm^3) due to experimental non-idealities. The Hall measurement of the fringing field of the CoFe bars, in conjuction with an approximate magnetic model described above, provide insight into the magnetic properties of the CoFe bar such as the fringing field, the magnetization switching field, and the saturation magnetization.

Chapter 4

Interface Magnetoresistance in InSb/CoFe

Before we can make spin devices from InSb/CoFe layered structures, the properties of the InSb/CoFe interface must first be understood [33, 34]. Spin injection through the InSb/CoFe interface can be affected by the anisotropic properties of the InSb and the properties of the CoFe magnetization [35, 36]. In Chap. 3, we studied the properties of CoFe. In this Chapter, we investigate the electromagnetic response of the InSb/CoFe interface. Variable temperature and angle dependence of the MR of the interface is presented.

4.1 Interface Magnetoresistance with In-Plane Rotation

4.1.1 Device Structure

In tunneling anisotropic magnetoresistance (TAMR) the magnetization (M) direction with respect to the crystallographic axis of InSb [110] determines the tunneling resistance. The tunneling resistance is high when the magnetization of the CoFe is along the [110] direction because the majority spin is then perpendicular to the direction of the strong SOI which is parallel to [-110] (weak SOI $\parallel$ [110]). If the magnetization is parallel to [-110], which is in the direction of strong SOI, then the

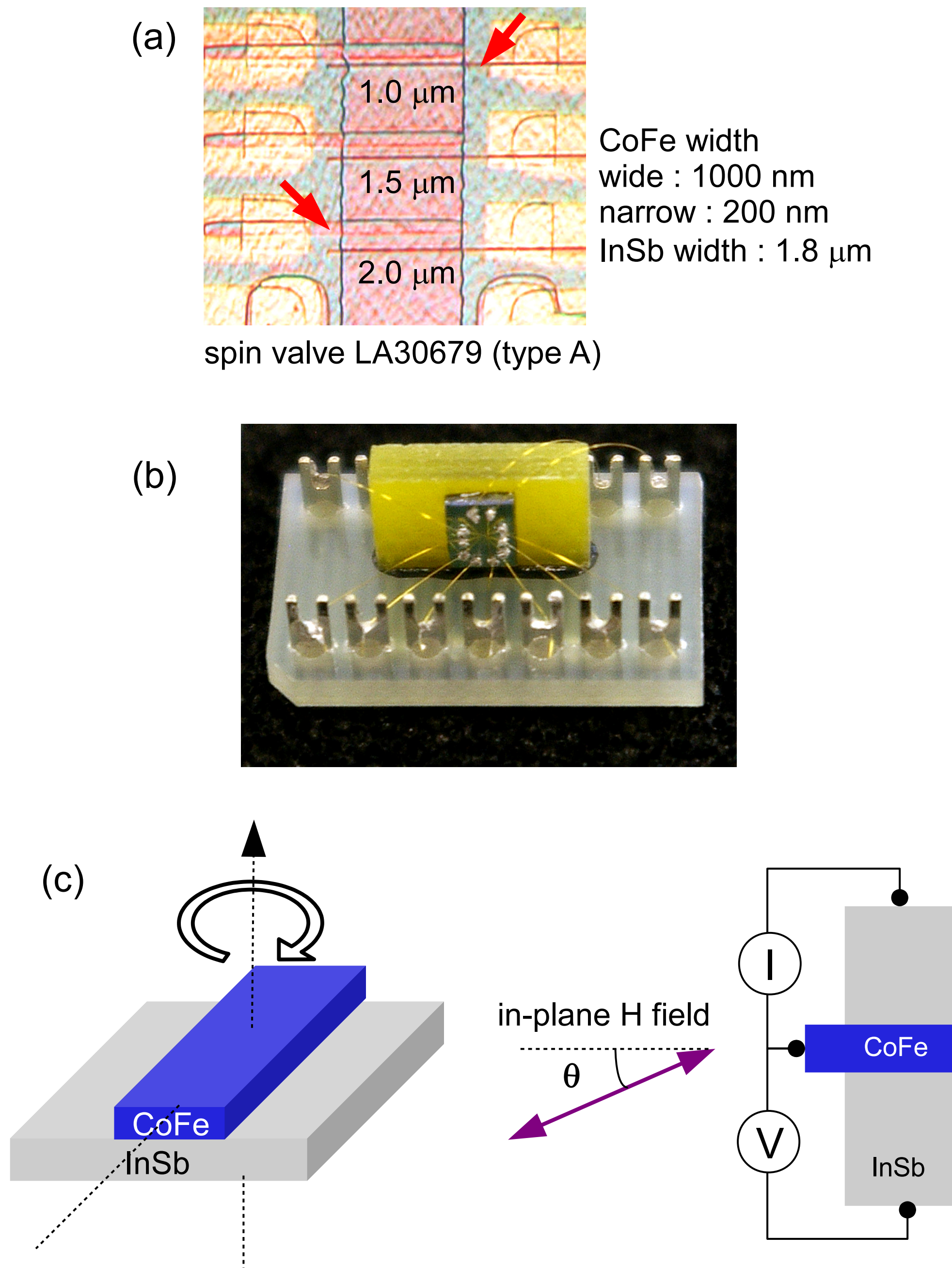

Figure 4.1: (a) Micrograph of type A InSb/CoFe spin valve geometry. (b) Modified DIP header allowing in plane rotation of the external magnetic field. (c) Schematic of the interface MR measurement configuration.

interface has a low tunneling resistance. Our MR measurement of the InSb/CoFe interface is performed in an InSb/CoFe lateral spin valve geometry (type A InSb film). Among the 3 pairs of spin valves shown in Fig. 4.1 (a), one wide electrode (1000 nm) and one narrow (200 nm) CoFe electrode are used for the MR measurement, as depicted with two red arrows in Fig. 4.1 (a). The spin valve sample is mounted in a modified 14-DIP header, which orients the sample such that the external magnetic field can be applied in the plane of the InSb. The modification is achieved by attaching a fiber glass segment vertically and then mounting the sample to it, Fig 4.1 (b). For the MR measurements of the single CoFe electrode on InSb, a 3-contact configuration is utilized, as shown in Fig 4.1 (c). A 1 μA current is applied between the CoFe electrode and the InSb, and a voltmeter is connected between the CoFe and the other side of InSb channel. In such a 3-contact configuration, the interfacial MR is measured, as well as the resistance of the CoFe electrode and lead wire. Assuming most of the current injected is at the first contact point between InSb and CoFe near the SiO edge, the estimated resistances of the CoFe (3 $\Omega/_\Box$) are $\sim$75 Ω and $\sim$15 Ω for the narrow and the wide CoFe electrodes, respectively.

4.1.2 Interface Magnetoresistance

The I-V characteristics of the wide and narrow electrodes measured at 1.3 K show a linear behavior over most of the range in V (Fig. 4.2). However, for both I-V traces, in the 1st quadrant ($I > 0$, $V > 0$) slight curvatures are noticed, which indicates that a Schottky type potential barrier is present at the interface. The I-V curves for both electrodes obtained at several temperatures (1.3-3.9 K) show no dominant temperature dependence as shown in Fig. 4.3.

Fig. 4.4 (a) and (b) show the MR signals of the narrow and wide CoFe electrodes. The temperature of the measurement is 1.27 K for narrow bar and 1.34 K for wide one. The in-plane external field H is parallel to the CoFe electrode (θ=0°) and the sweep range is from -5000 Oe to 5000 Oe. The blue (red) solid lines indicate a forward (backward) sweep of the magnetic field. A Hall slope has been subtracted for clarity. The MR signals for both electrodes show a peak at low field, which is mostly symmetric in H. The relative MR values are about 17% ($\Delta R/R_0$) and 6% for the narrow and wide electrodes, respectively, which is very high compared to previous reports of tunneling anisotropic MR (TAMR) [37–40]. The difference of the background resistances ($R_{0,wide} - R_{0,narrow}$) of both traces is $\sim$55 Ω which is comparable to the difference $\sim$60 Ω of the estimated resistances of both the CoFe electrodes. Because R_0 is not dependent on H, the CoFe resistance does not contribute to the

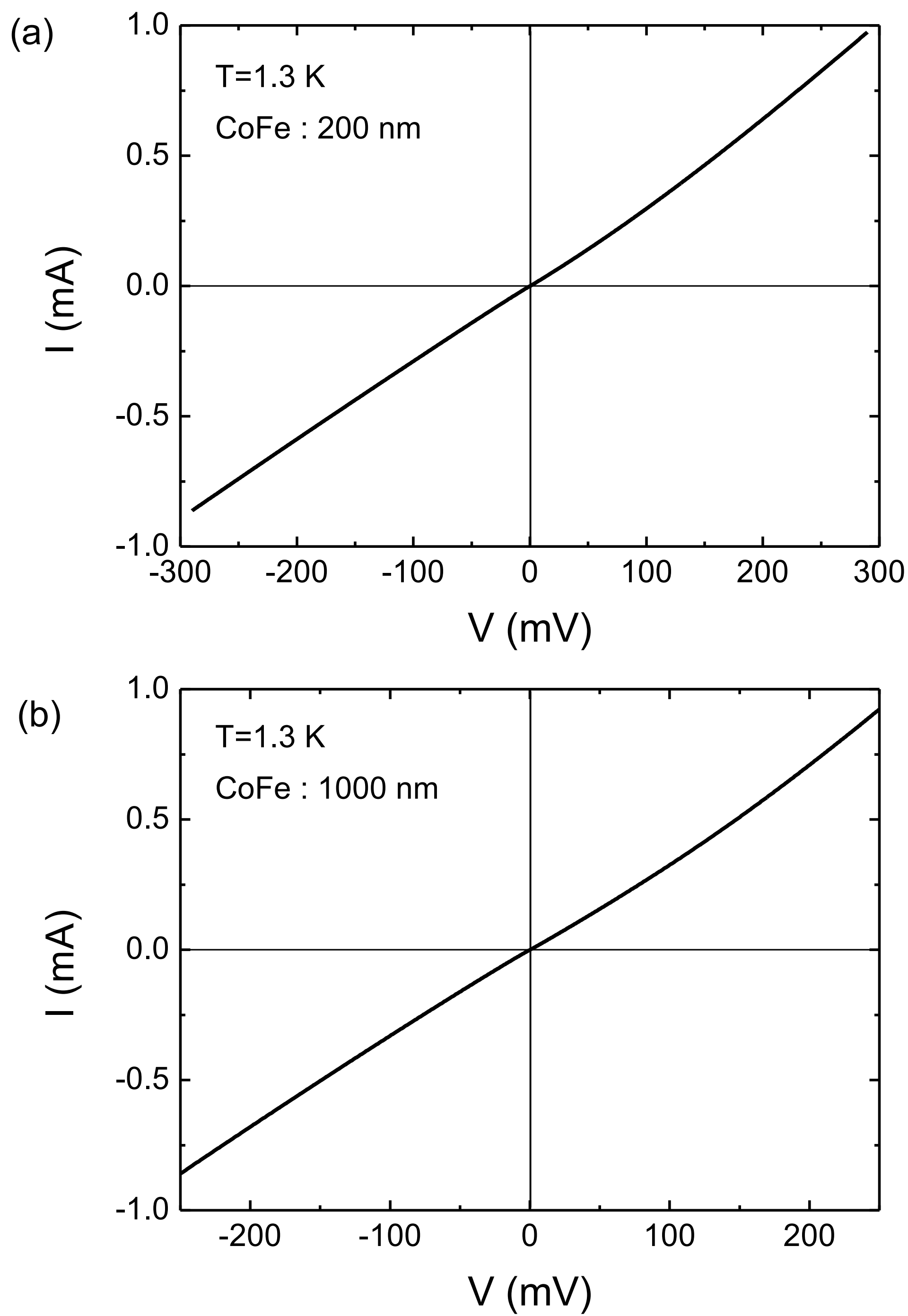

Figure 4.2: (a) *I-V* traces at 1.3 K on narrow CoFe electrode and (b) wide CoFe electrode. Both (a) and (b) present ohmic behaviors with small curvature.

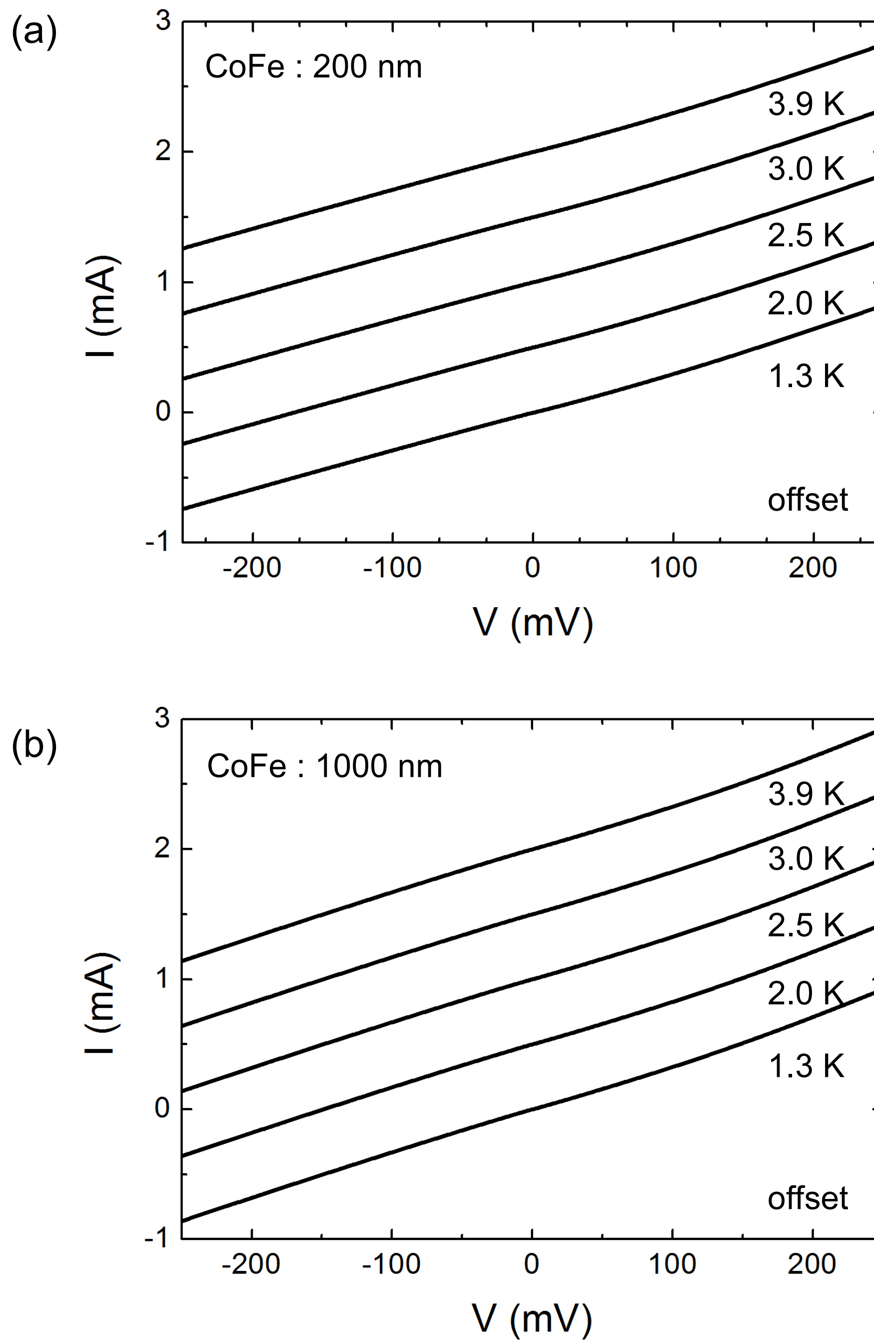

Figure 4.3: (a) I-V traces at 1.3-3.9 K on narrow CoFe bar and(b) wide CoFe bar. Both (a) and (b) present no temperature dependence. The data are offset for clarity.

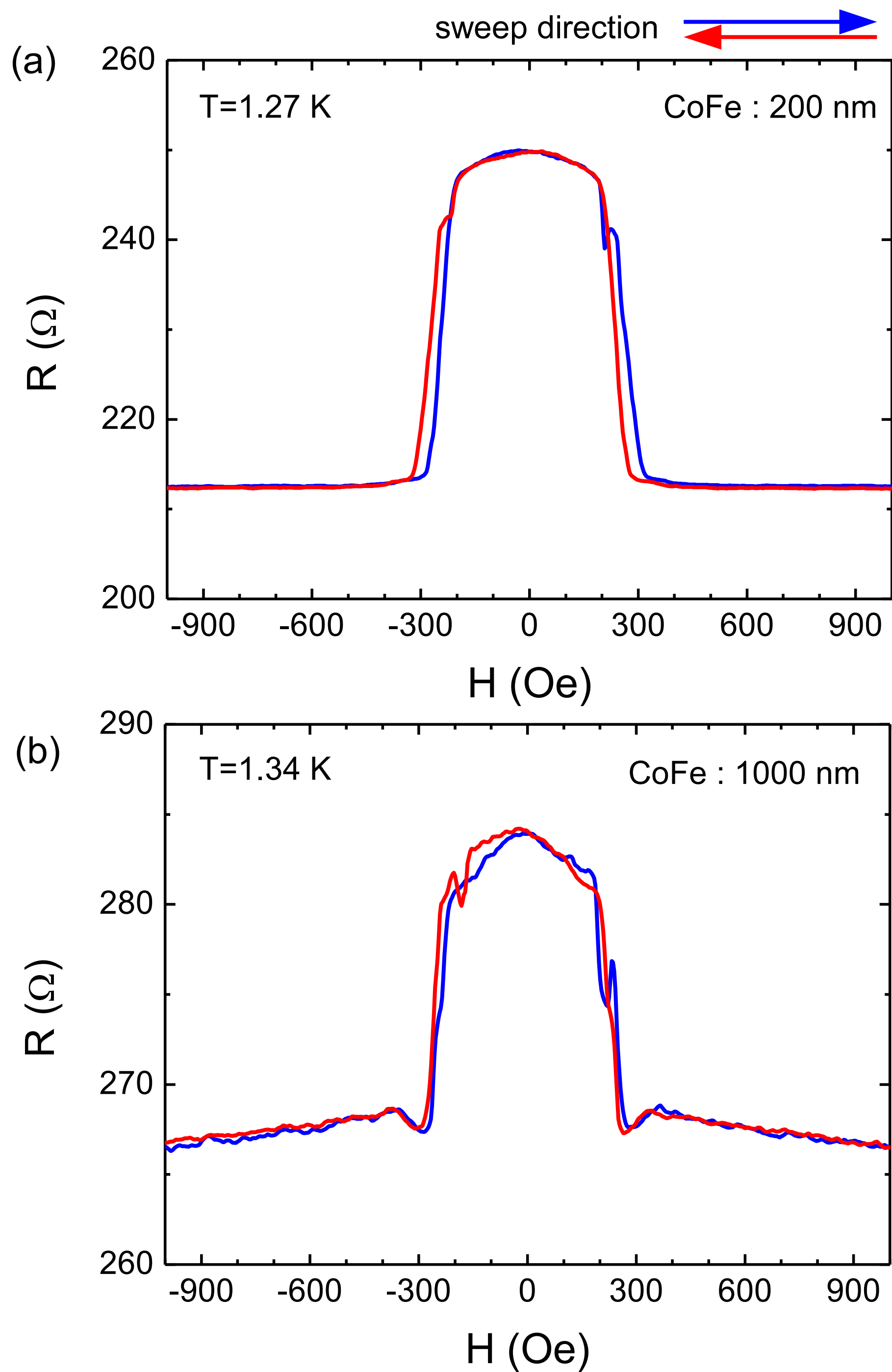

Figure 4.4: Interface MR measurement with blue and red indicating opposing magnetic sweep directions for (a) narrow and (b) wide CoFe bars.

signal, implying that the interface contribution is the dominant component of the signal. The critical magnetic field H_c, denoting the half-width of the peak, is $\sim$300 Oe for both electrodes. From the slight hysteresis on both graphs, the signal must depend on the magnetization. Based on the fact that the state of spins tunneling through the interface is dependent on the magnetization of the ferromagnet, we expect our MR signal to respond to the magnetization switching of the CoFe electrodes around its coercive field ($\sim$630-900 Oe), which is observed in Chap. 3. However, the MR measurements here do not present such a response. The MR traces indicate switching at a much lower field ($H \approx$300 Oe), suggesting the CoFe switching does not directly affect the interface MR.

4.1.3 In-Plane Angle Rotation

The angle dependence of the MR signal for the narrow bar is presented in Fig. 4.5 (a). The measurement is at 2.0 K. Fig. 4.5 (b) shows $\Delta R/R_0$ versus θ, in which $\Delta R/R_0$ increases relatively fast for $\theta < 30°$, and saturates for $\theta > 60°$. The same data is plotted in polar form in Fig 4.6, where we assume and extrapolate that the signal should be periodic in π. Fig 4.6 indicates an uniaxial anisotropic property of the CoFe electrode. Interestingly, the signal increases as the magnetic field rotates into the hard axis of the CoFe bar (see the 90° trace in Fig. 4.5 (a)).

The angle dependence of the MR for the 200 nm wide bar is also measured at 2.5 K and 3.0 K, with 0° and 90° traces shown in Fig. 4.7. Similar to the results at 2.0 K, $\Delta R/R_0$ is larger at 90° than at 0° for these temperatures as well.

On the other hand, in the interface MR measurement for the wide CoFe electrode an angle dependence is not observed in the temperature range 1.28-1.35 K and at 2.0 K, as shown in Fig. 4.8 (a) and (b). Further, no angle dependence is present at 2.5 K for 0° and 90° as indicated in Fig. 4.9 (a). At 3.0 K, a small difference in the signal is observed, Fig. 4.9 (b), but its origin may not be due to angle rotation. Here, the 0° signal is larger than that at 90°, which is not consistent with the results obtained from the narrow bar. And the signal difference between 0° and 90° for the narrow bar is temperature sensitive, being $\sim$1.2 Ω, $\sim$0.8 Ω, and $\sim$0.7 Ω for 2.0 K, 2.5 K, and 3.0 K, respectively. For the wide CoFe electrode, the signal difference observed at T=3.0 K should similarly appear at lower temperatures and temperature rather than θ could be responsible for the variation. Therefore, an angle dependence of the MR signal for the wide CoFe electrode is likely not present in the temperature range of 1.3-3.0 K.

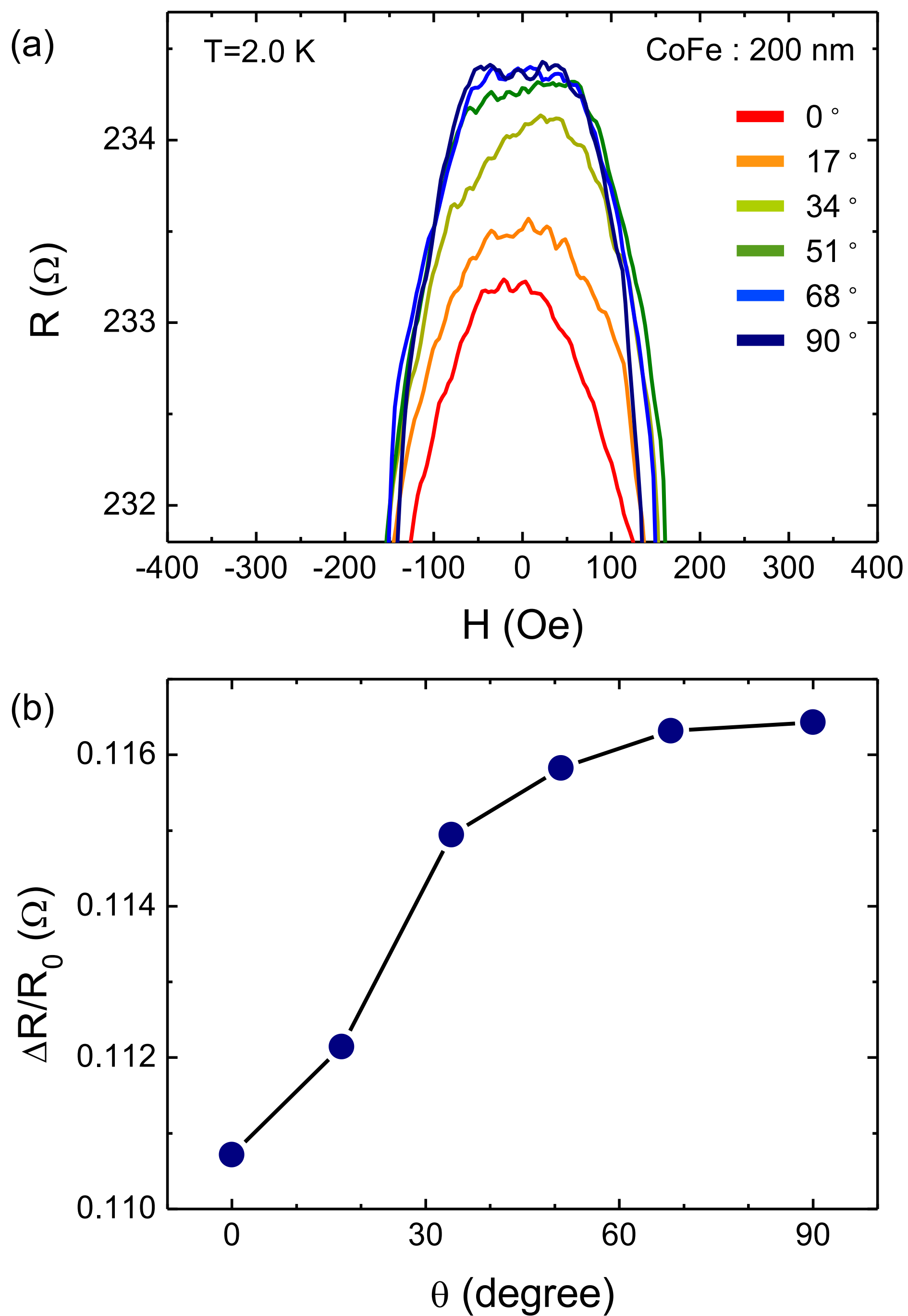

Figure 4.5: (a) Angle dependence measured at 2.0 K. (b) Signal amplitude ΔR vs θ of the traces in (a).

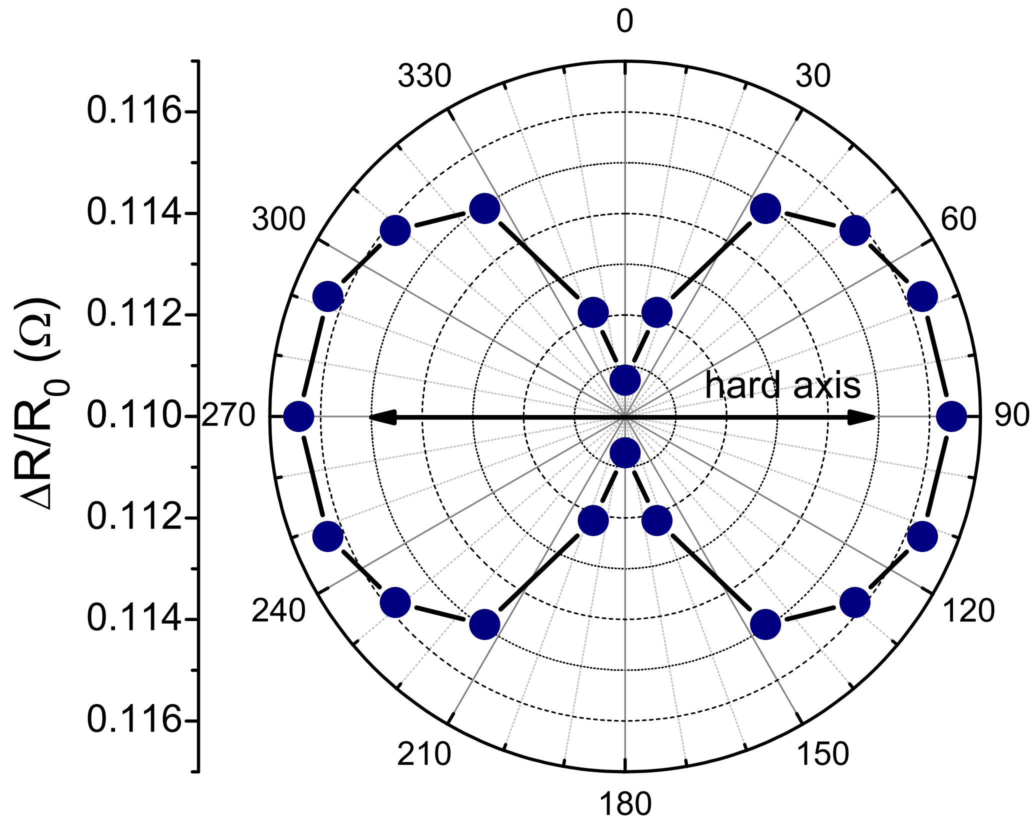

Figure 4.6: Polar plot of ΔR of the interface between the narrow CoFe electrode and the InSb layer, at 2.0 K. The hard axis lies along the 90° to 270° axis.

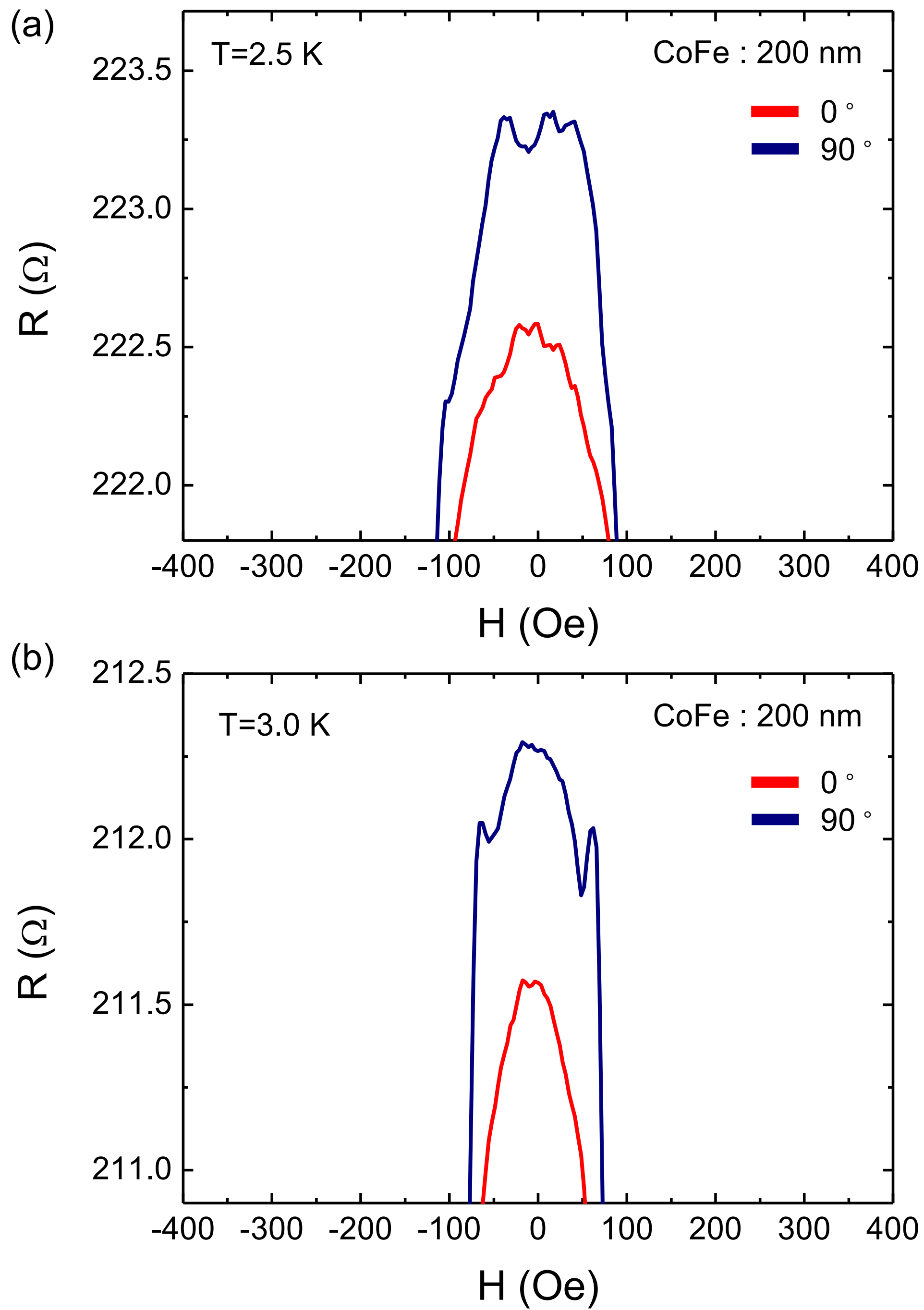

Figure 4.7: Interface MR of the 200 wide nm CoFe bar at 2.5 K (a), and at 3.0 K (b).

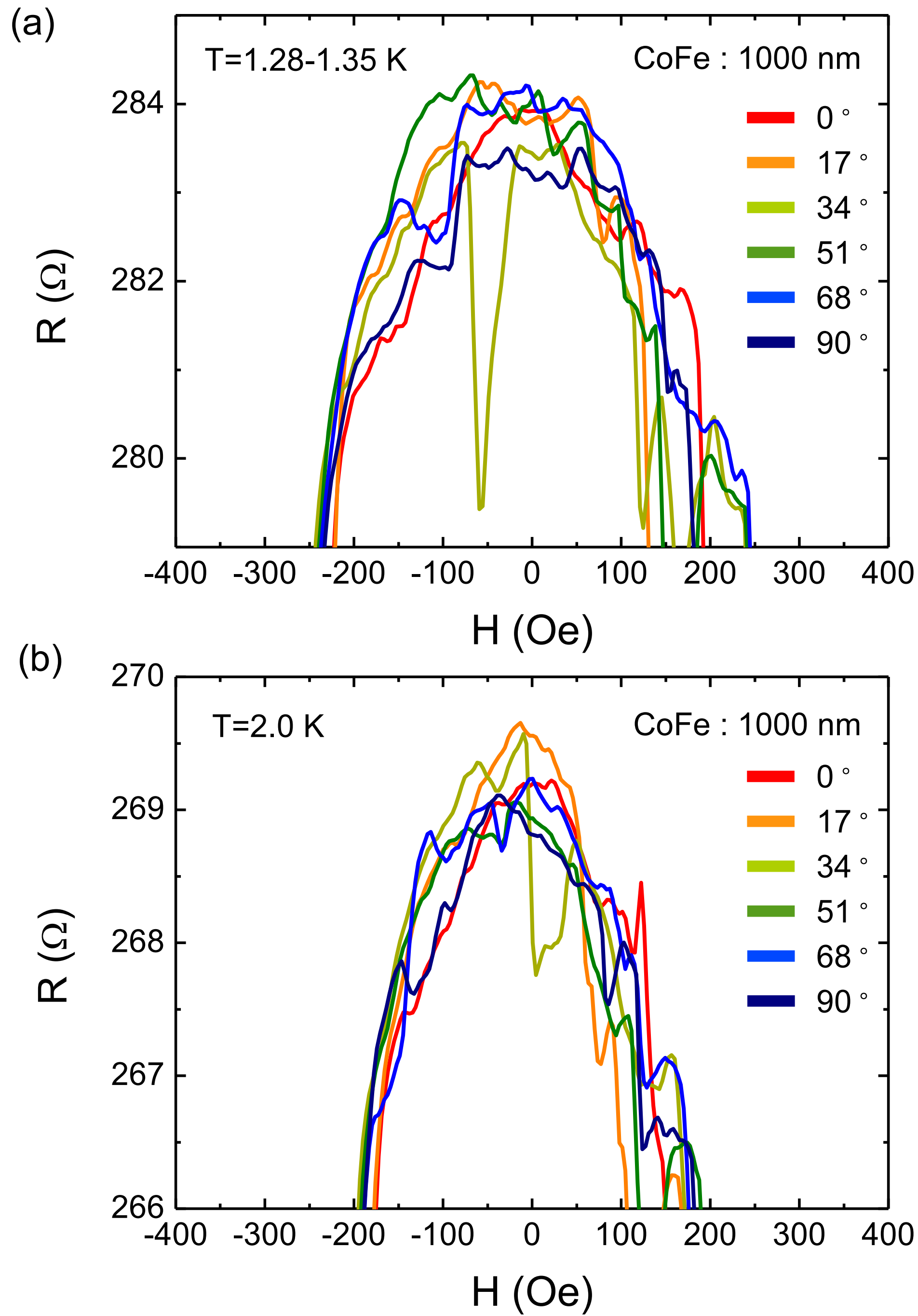

Figure 4.8: Interface MR of the 1000 nm wide CoFe bar in the temperature range 1.28-1.35 K (a), and at 2.0 K (b).

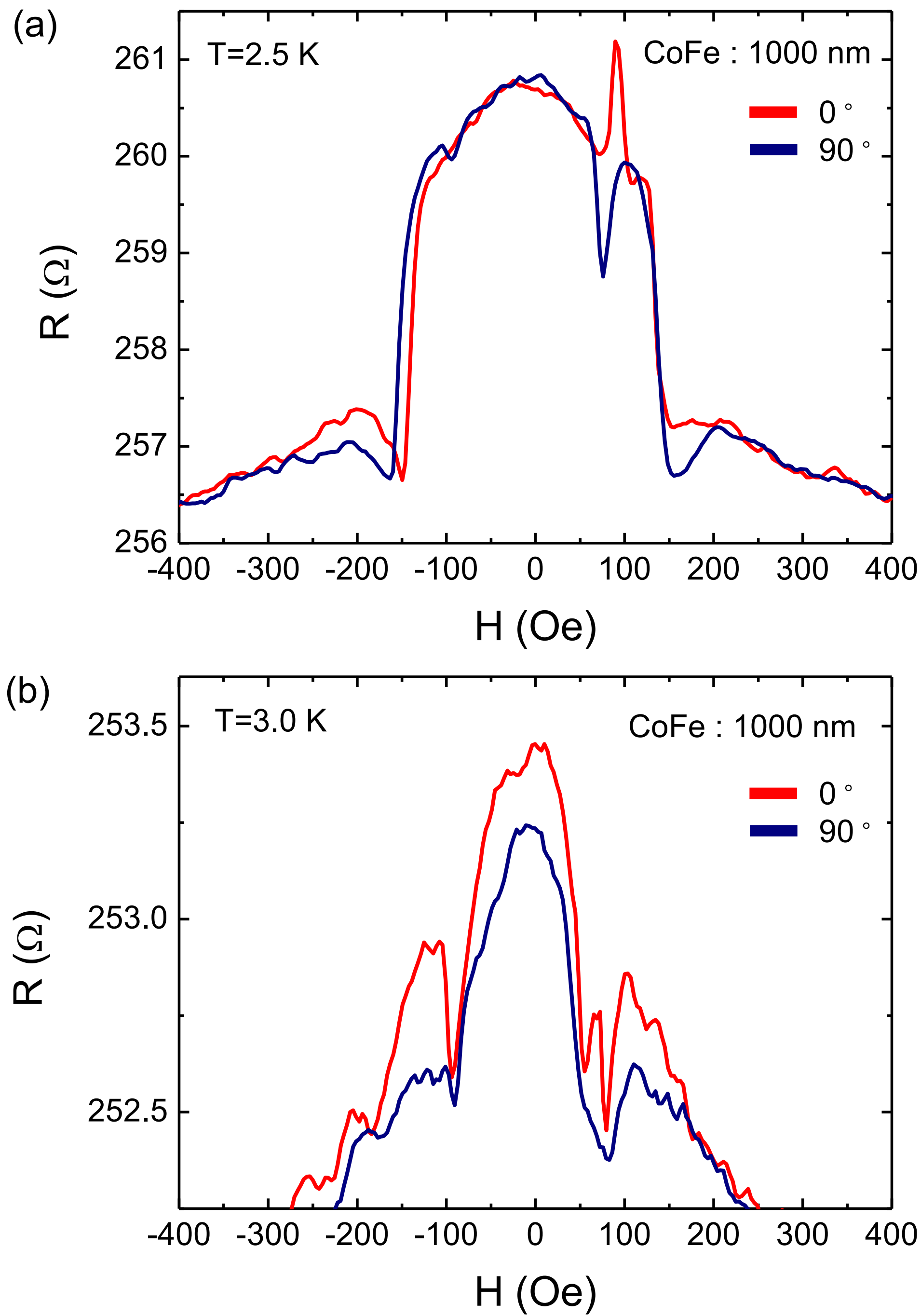

Figure 4.9: Interface MR of the 1000 nm wide CoFe bar at 2.5 K (a), and at 3.0 K (b).

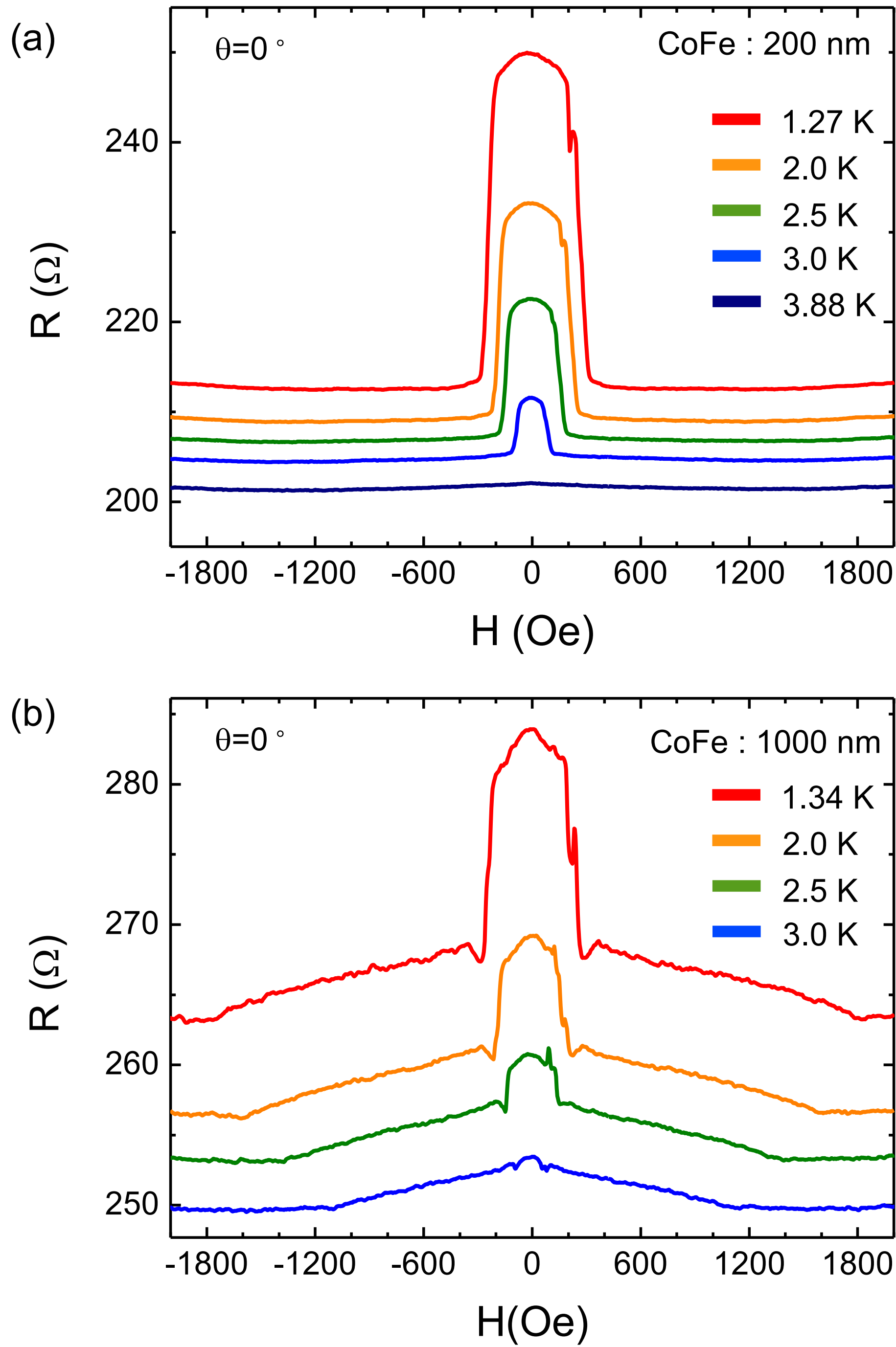

Figure 4.10: Temperature dependence of interface MR for narrow (a) and wide (b) CoFe bars with θ=0.

4.1.4 Temperature Dependence

The interface MR signal for both the narrow and the wide CoFe electrodes measured at 0° is sensitive to temperature in the range of 1.27-3.88 K, as presented in Fig. 4.10 (a) and (b). For the narrow and wide electrodes, as the temperature increases, both the amplitude and width of the signal peak decrease. In the case of the wide electrode, the traces show wider features $H \sim 1500$ Oe which decreases as temperature increases. The features here may be the result of a superposition of two signals with a similar temperature dependence.

In the Fig. 4.11 (a), the MR amplitudes of the narrow and the wide electrodes are extracted from the data of Fig. 4.10 (a) and (b), and are plotted versus temperature. Linear fits are indicated with red dashed lines in each plot. According to the linear fits, the extrapolated MR amplitudes of both electrodes disappear at 3.2-3.5 K, and the MR widths of both electrodes match over the entire T range. In Fig. 4.11 (b), the critical fields versus temperature are plotted, along with the linear fits.

4.2 Ferromagnetic Phase Model

The observed interface MR exhibits unique features which are the weak angle dependence with the largest MR along the CoFe hard axis, large MR peak at low field, and highly temperature dependent behaviors of the MR amplitude and width. To our knowledge, known phenomena in ferromagnets, semiconductors and any layered structures thereof are not consistent with our signal. Anisotropic magnetoresistance (AMR) is ruled out, due to the following reasons. Firstly, the order of magnitude of our signal does not match with any typical AMR signal [41]. Secondly, AMR is strongly dependent on the direction of the magnetization. However, the angle dependence of our signal is very weak. Lastly, the Curie temperature of CoFe is above that of room temperature, which means AMR could be temperature insensitive at our measurement temperatures. Taking into account the InSb layer in our samples, TAMR can be suggested. The TAMR signal is determined by the SOI and the magnetization of ferromagnets. In spite of the strong SOI of InSb and the Schottky type interface, our signal cannot be explained by TAMR due to the temperature sensitivity and the four issues listed above. The strong temperature dependence leads to our reasoning that an energy dependence or dephasing mechanism, such as localization and electron-electron interaction (EEI) [42], may be the cause. WAL has been observed in InSb but not WL. When a ferromagnet is adsorbed onto the sur-

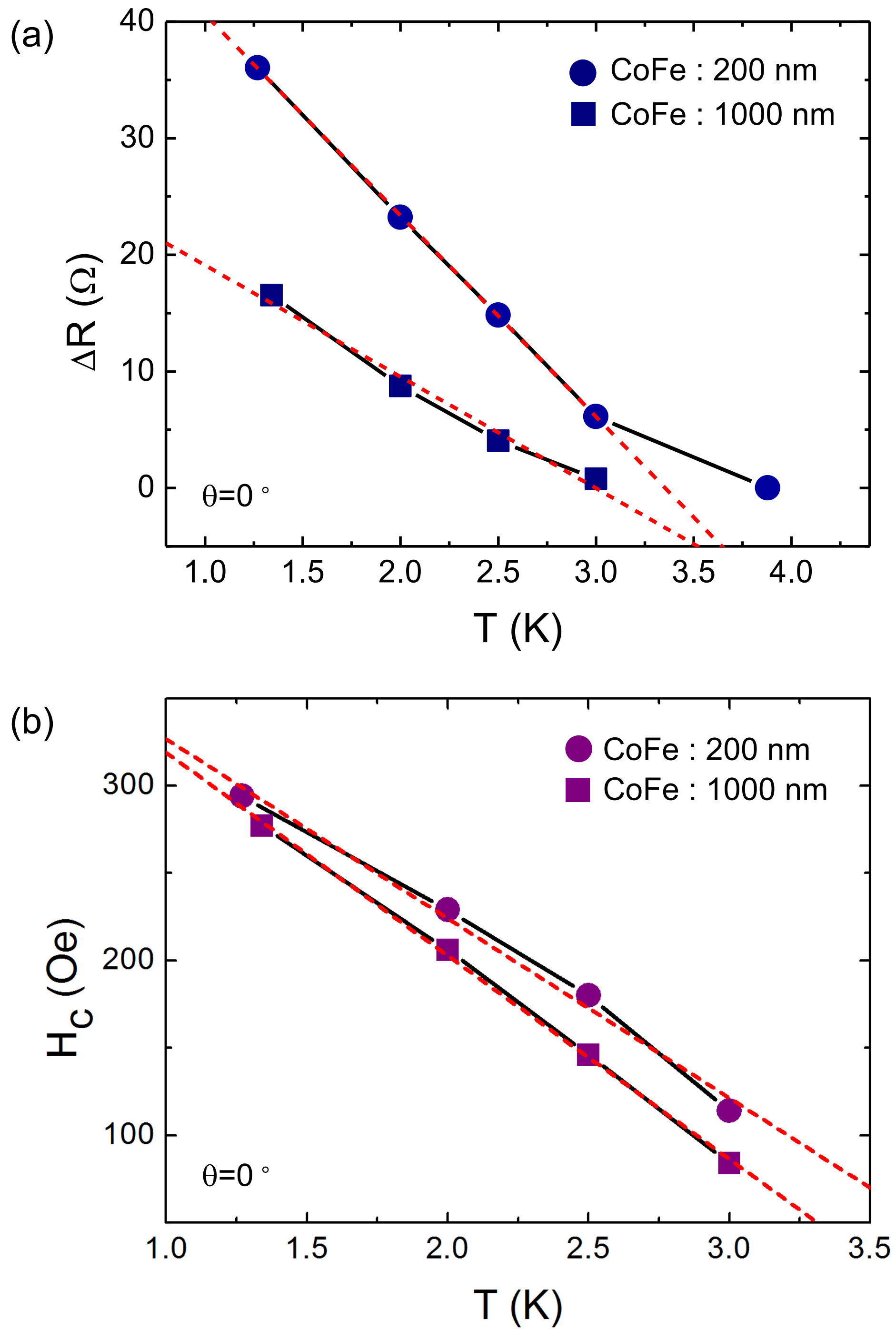

Figure 4.11: For the narrow and the wide CoFe electrodes, extracted signal amplitude (ΔR) and critical H field (H_c) values from Fig. 4.10 are plotted versus temperature. Linear fits are indicated with red dashed lines.

face of semiconductors, spin-flip scattering is induced, which flips the WAL to WL, consistent with our result. However, the order of magnitude of WL [43, 44] is much smaller than our signal. In addition, in our measurement the H field is in-plane, which diminishes the expected WL signal. The EEI contribution to the signal is almost identical to WL in temperature and magnetic field behavior. But, due to the low carrier density of InSb, EEI cannot be the reason for our observations.

The origin of our signal is not fully understood. The measurement results indicate that the signal is dependent on magnetic hysteresis in our signals. However, the hysteresis in the signal is temperature dependent, which is not present in CoFe only. In addition, H_c is smaller than the coercive field and is also temperature sensitive. Magnetization switching is not present in our signal. The weak angle dependence of our signal is also due to magnetization but is not typical. Based on the observations listed above, we deduce that only the magnitude of the magnetization is responsible for the MR signal. At 300 Oe ($\approx H_c$) the Zeeman splitting in the InSb is $g\mu_B B$=90 μeV and at T=1.3 K, $k_B T$=110 μeV. As the temperature and/or H increase, the signal may disappear due to energy level broadening. Based on the analysis of the temperature dependence and the magnetization, we tentatively attribute our signal to a ferromagnetic phase in the InSb which is induced by spin injection from the CoFe into InSb. During the spin injection, the interface between the InSb and CoFe forms a stable ferromagnetic phase, lying at an energy $\approx$100 μeV lower than the normal state. This phase is destroyed by an increase in temperature and magnetic field, which is consistent with our signal. Once the ferromagnetic phase is induced by the injection of spins, then it responds to a magnetic field. The contribution of the magnetization of CoFe is to polarize the electron spin; a polarized spin source. The critical field of the new ferromagnetic phase decreases as temperature increases, due to level broadening. At low magnetic fields, the induced ferromagnetic phase in InSb is preserved. In Fig. 4.12, the magnetizations of the CoFe electrode, the magnetization directions in the ferromagnetic phase and applied magnetic fields are illustrated.

A good example of a ferromagnetic phase existing in a semiconductor is the dilute magnetic semiconductor system, DMS. MR signals measured with an in-plane magnetic field performed in GaMnAs showed a similar behavior to our signal and with a temperature dependence of the same order of magnitude [45, 46].

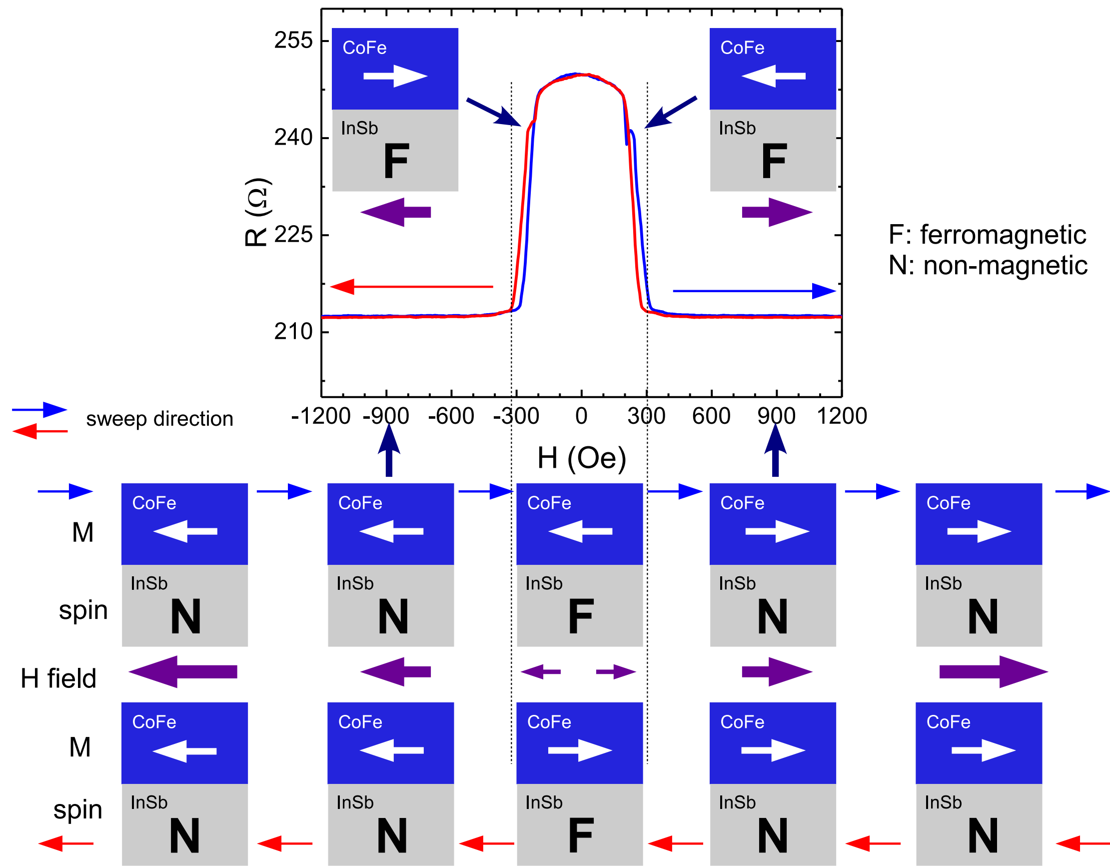

Figure 4.12: The ferromagnetic phase model. The MR result of the narrow CoFe bar with the CoFe magnetizations (M) (white arrows), the existence of ferromagnetic phase (black cross) and magnetic fields (purple arrows). At low fields ($H < 300$ Oe), a ferromagnetic phase is induced in the InSb. Insets: The configurations when the hysteresis the MR signal appears.

Chapter 5

Non-Local Detection of Spin Transport in InSb/CoFe Lateral Spin Valves

In the previous chapter, we studied the magnetoelectric properties of the interface between InSb and CoFe. A temperature sensitive behavior, a dependence on the CoFe magnetization, and a weak dependence on the in-plane rotation of the MR signal suggested the existence of a ferromagnetic phase induced by spin injection at the interface between InSb and CoFe. In this chapter, we will probe the spin current using InSb/CoFe LSV device geometries with a non-local measurement technique. An all electrical detection of spin currents is required to utilize spin for future spin devices. Several successful detections of spin current in semiconductors have been reported [47–53], but few are for semiconductors that exhibit strong SOI, such as InSb.

5.1 Device Fabrication

The details of the fabrication procedure of InSb/CoFe LSV is described in Sec. 2.2. Three LSVs are fabricated with type A and C InSb films (see Table 1.1). Both films have the same active layer thickness, but different carrier densities (n_A=0.65×10^{22} m^{-3}, n_C=8.9×10^{22} m^{-3}). A 18 μm width InSb channel is fabricated for all three LSVs. Two LSVs are fabricated with type C InSb. Of these two, one is comprised of

three CoFe electrodes, as depicted in Fig. 5.1 (a), (b), and (c), and the other consists of three pairs of CoFe electrodes, as shown in Fig. 5.2 (a). The CoFe electrodes are designed with different widths to induce shape anisotropy. For type C LSVs, the widths of the narrow and the wide CoFe electrodes are 200 nm and 500 nm, respectively. According to the LSV principle discussed in Sec. 1.2, the spin detection signal depends on the separation of the ferromagnetic electrodes; when that separation is longer than the spin coherence length no signal is observed. The AL results of both films (Fig. 1.11) show that the spin coherence lengths (L_{SO}) of type A and type C CoFe films are 1.5 μm and 1.2 μm, respectively. For the first type C LSV (Fig. 5.1 (a) and (b)), the separations of the three bars are 0.8 μm and 1.8 μm. For the second one, the separations of each pair are 0.8 μm, 1.0 μm and 1.2 μm, respectively (Fig. 5.2). A LSV geometry fabricated on type A InSb has three pairs of the CoFe electrodes as shown in Fig. 5.3 (a). The widths of the CoFe electrodes are 200 nm and 1000 nm for the narrow and wide electrodes, respectively, and the separations are 1.0 μm, 1.5 μm and 2.0 μm. The thickness of the CoFe electrodes is 55 nm for all the three LSVs discussed in this chapter.

5.2 Non-Local Lateral Spin Valve Measurements

For the first type C LSV (Fig. 5.1), a 10 μA current is applied between the wide CoFe electrode and the InSb. The narrow CoFe electrode, as a detector, measures the potential developed between the InSb/CoFe junction due to the accumulation of spin as shown in Fig. 5.1 (d) and (e). An in-plane external magnetic field is applied along the longitudinal direction of the CoFe electrodes. The total magnetic field sweep is from -20000 Oe to 20000 Oe. The R_s, depicted as (V/I), versus H in the two detectors with different separations from the injector are shown in Fig. 5.4. The near detector is 0.8 μm away from the injector, the far detector, 1.8 μm. In plots (Fig. 5.4 (a) and (b)), the Hall slopes are subtracted for clarity. At high field, the R_s is constant. When H reaches $\sim$300 Oe, R_s starts to decreases. The overall feature of the signal is that it is symmetric in H, showing a two state behavior. On the other hand, hysteretic features along with narrow peaks at 200 Oe are observed. While these peaks may be caused by the CoFe electrodes, the magnetic field value where the peaks appear (critical magnetic field H_c) are different then the coercive field of the CoFe electrodes. The non-local signal measured at the far detector having a 1.8 μm separation with the injector shows a weak signal, where R_s drops starting at $H_c \approx -300$ Oe. Thus we observe the same magnitude of the H_c value indicating that this signal is of the same origin as that measured at the near detector. The ΔR_s

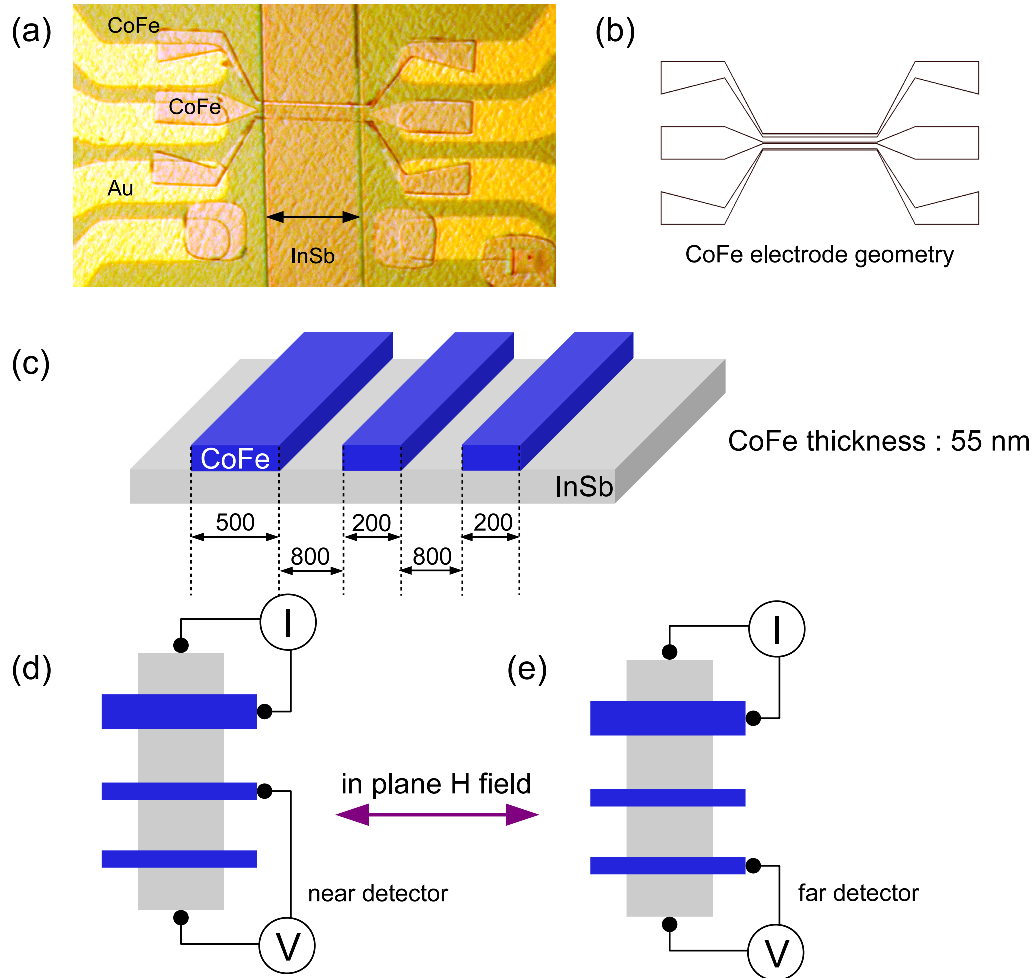

Figure 5.1: (a) Micrograph of type C InSb/CoFe LSV. The width of InSb is 18 μm. (b) CoFe ferromagnet electrode geometry. (c) Dimensions of the CoFe electrode and seperation distance, all in nm. Non-local measurement configuration, showing the near (d) and far (e) detector locations. The wide CoFe electrode is 1000 nm in width, and the narrow one, 200 nm. The thickness of the CoFe electrode is 55 nm, while the thickness of the SiO layer is 1.2 μm.

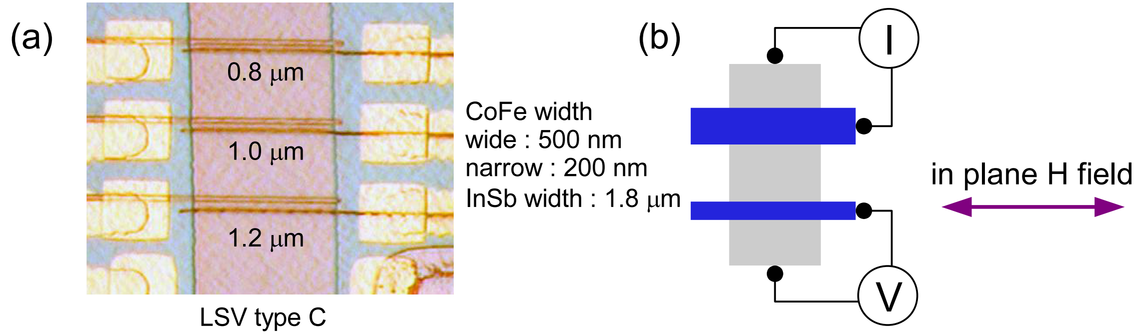

Figure 5.2: (a) Micrograph of type C InSb/CoFe later spin valve. The width of the InSb is 18 μm. (b) The non-local measurement is performed at 1.3 K and the applied current is 10 μA.

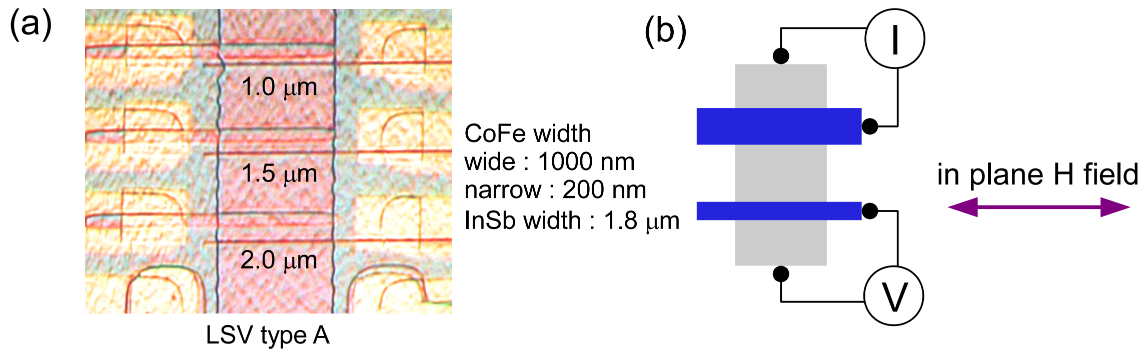

Figure 5.3: Micrograph of type A InSb/CoFe later spin valve. The width of the InSb is 18 μm. The measurement is performed at 1.3 K and the applied current is 10 μm.

diminishes in the far detector as expected. The $\Delta R_s/R_{s,0}$ is 10% and 1.3% for 0.8 μm and 1.8 μm separations, respectively. This is expected as the spin coherence length is 1.2 μm in type C InSb. The spin effect, such as R_s, in non-local system decreases exponentially (e^{-L/δ_s}) beyond the spin coherence length as discussed in Chap. 5. Theoretically, the far detector measures 22% of total injected spins because most of spins are randomized after traversing that distance from injector. The calculated ratio of ΔR_s for the near and far detector is 6% which is smaller than expected. The additional spin depletion of InSb could be caused by absorption of the spin current of the CoFe electrode (near detector) located in the path of the spin current. [19, 54]

The second type C LSV geometry consists of three pairs of spin valves, Fig. 5.2 (a). Here, the wide CoFe electrodes are 500 nm in width, the narrow are 200 nm. The measurement is performed at 1.3 K with a non-local configuration, Fig. 5.2 (b). As depicted in Fig. 5.2 (a) and (b), the three LSVs have 0.8, 1.0, and 1.2 μm separations, to further study the separation dependence of the non-local LSV signal. The in-plane magnetic field sweeps from -7500 Oe to 7500 Oe. A 10 μA current is applied to the injector CoFe electrode. The R_s values of the detector CoFe electrode are presented in Fig. 5.5 (a), and (b). For the plots in Fig. 5.5 (a), the wide CoFe electrodes are used as the injectors for each LSV, while in Fig. 5.5 (b) the narrow CoFe electrode is used as the injector. The overall features of the R_s here are similar to the result of the first LSV device on type C InSb with three CoFe electrodes, except for the hysteretic peaks observed in Fig. 5.5. To further investigate our observations, we fabricated the same geometry but with different physical dimensions of the CoFe to minimize the effect of the magnetization induced switching. We observed no clear magnetization switching at the coercive field. Yet, we suspect that the magnetization of CoFe electrode plays a role, as we observe hysteresis. Overall, the signals (R_s) appear symmetric in H with $H_c \approx 300$ Oe. The separation dependence of the signal amplitude is not observed. For the wide CoFe injector LSV, the $\Delta R_s/R_{s,0}$ are 2.6%, 1%, and 1% for 0.8 μm, 1.0 μm, and 1.2 μm, respectively. For the narrow injector LSV,the $\Delta R_s/R_{s,0}$ are 1.2%, 1%, and 3% for 0.8 μm, 1.0 μm, and 1.2 μm, respectively. The R_s values changes when the injector and the detector are exchanged. According to this observation the dependence lies more on the exact CoFe/InSb interface than on the distance between the injector and detector, typical for spin injection phenomena. A noticeable fact of the non-local LSV result is that the $R_{s,0}$ and ΔR_s are all negative. If the injection and detection are carried out in an ideal InSb/CoFe interface, the distribution of spins in the InSb channel will be uniform. However, the injection and detection are likely to be localized along the interface [55]. In our LSV structure, the CoFe bars are only contacted on one side. If the injection and detection do not occur in the center of the InSb channel, the signal baseline may be shifted negative or positive.

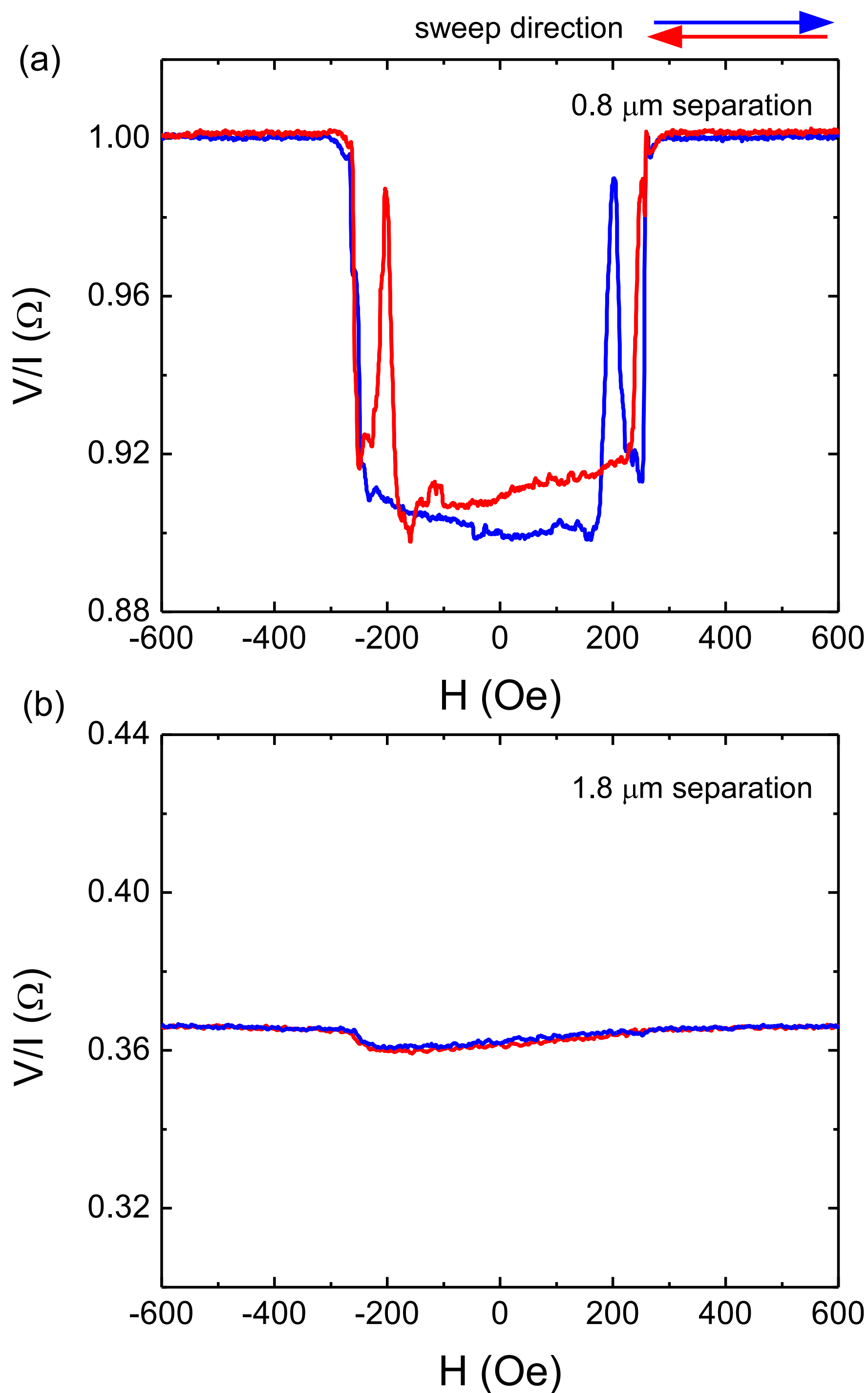

Figure 5.4: (a) Non-local measurement result of InSb/CoFe LSV with 0.8 μm separation shows two state signal and hysteretic peaks. (b) The signal disappears in 1.8 μm separation spin valve.

It is probable that the injection and detection points would shift to the side where the electric contacts are. The supportive evidence is described in Chap. 7. In Fig. 5.2 (a), the wide electrodes are contacted on the left side of InSb channel, and the narrow electrodes ones, on the right side of channel. This asymmetry of the LSV geometry is likely to induce a negative baseline in the detection. Comparison of the results with type C LSV geometries support this reasoning.

Other non-local measurements are perform in a LSV of type A InSb, which has a lower carrier density and longer spin coherence length than type C InSb. Due to spin coherence length of 1.5 μm in type A InSb, the separations between the wide and narrow electrodes are fabricated to be 1.0 μm, 1.5 μm, and 2.0 μm. For this LSV geometry (Fig. 5.3), the width of the wide CoFe electrodes are increased by factor 2 to 1000 nm to observe the effect of the magnetization versus H_c. The non-local measurements are performed at 1.3 K with an in-plane magnetic field which sweeps from -7500 Oe to 7500 Oe. The overall shapes of the non-local signals of the type A LSVs are similar to the results observed in the type C LSVs. The H_c ($\approx$300 Oe) is observed for all signals. An interesting observation in the type A LSVs is the high resistive interfaces for the two CoFe electrodes. We apply a current of 10 μA, but this value is effectively 6.06 μA at the wide electrode in the LSV with 1.0 μm separation, and 4.85 μA at the narrow electrode in the LSV with 2.0 μm separation. When these two CoFe electrodes are used as the injectors, the detected R_s signals are flipped, as a comparison between Fig 5.6 (a) and (b) indicates. On the other hand, if the CoFe electrodes are used as the detector (instead of injectors) the signal does not flip. In the LSV with wide injectors, the $\Delta R_s/R_{s,0}$ are 0.29%, 1.1%, and 2.7% for the 1.0 μm, 1.5 μm, and 2.0 μm separations, respectively. For the narrow injector LSV, the $\Delta R_s/R_{s,0}$ are 2.3%, 1.3%, and 1% for 1.0 μm, 1.5 μm, and 2.0 μm, respectively. Inspecting the signal amplitude for both wide and narrow LSVs, Fig. 5.6 (a) and (b) respectively, we deduce that the non-local LSV signal in InSb/CoFe is very sensitive to the injector interface.

5.2.1 Current Dependence

The H_c and ΔR_s do not appear to change with applied current magnitude, as observed when the wide CoFe electrode is used as an injector for type C LSV. As the magnitude of the current decreases, from 50 μA to 10 μA to 2 μA, the noise level of our measurement increases, as depicted in Fig. 5.7. As in previous measurements, we observe the feature at around $\pm$300 Oe for all the traces.

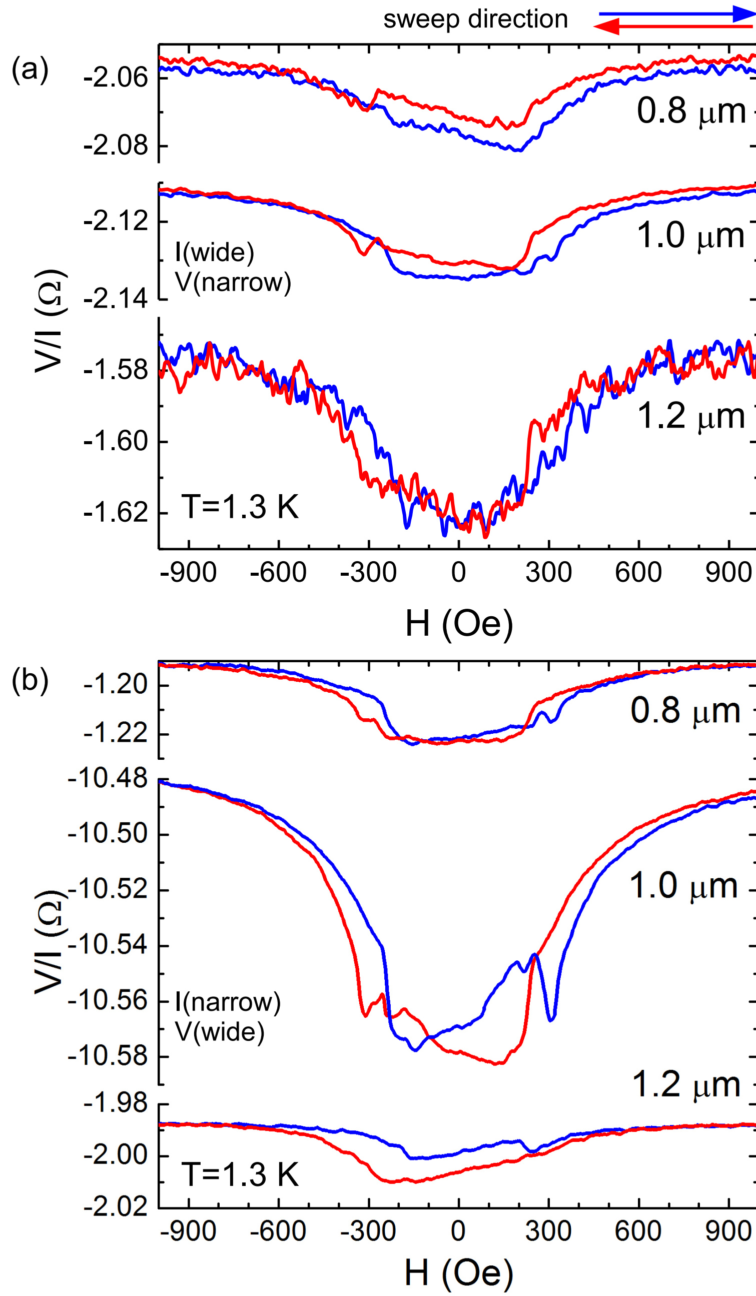

Figure 5.5: Non-local spin valve signal with type C InSb film with varying CoFe electrode separations. Geometry of this device is depicted in Fig. 5.2 (a). The signal amplitudes do not appear to depend on the separations. Upper graph, the wide CoFe electrodes are used as injectors, while the narrow electrodes inject. In the upper graph, the induced voltage is measured at the narrow electrode, in the lower graph at the wide electrode.

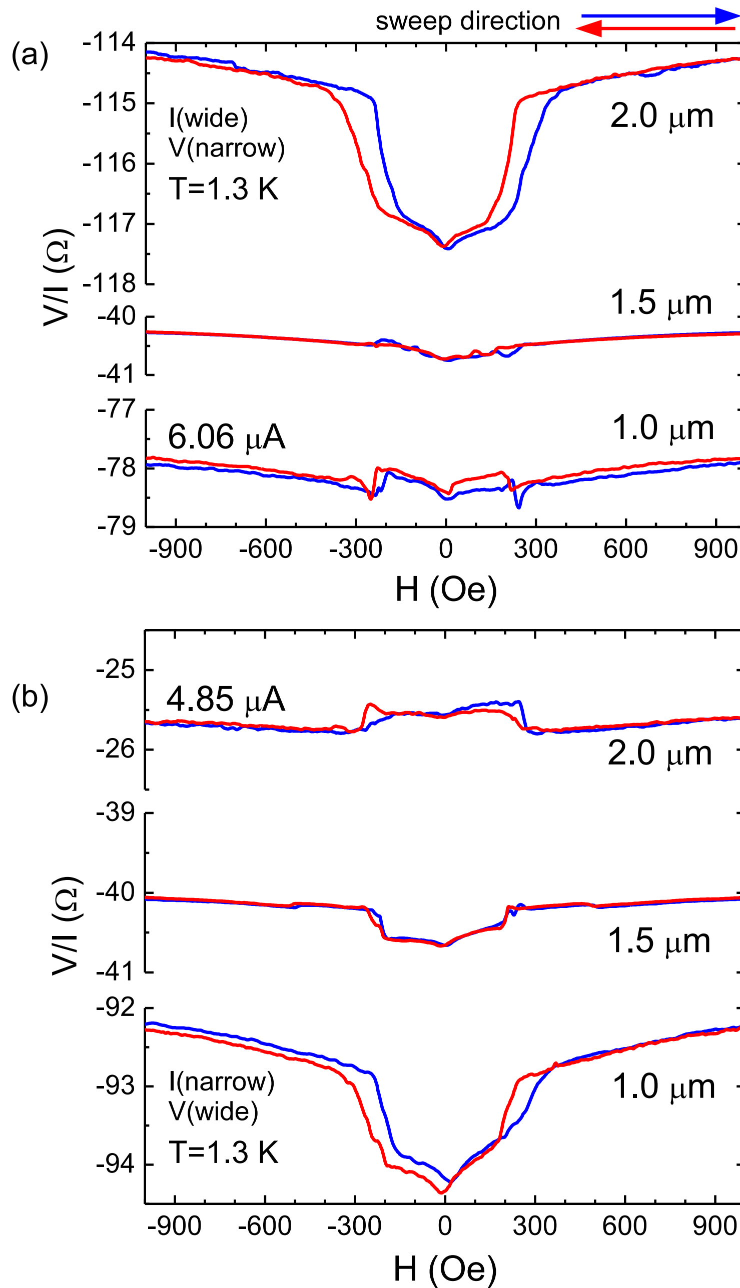

Figure 5.6: Non-local spin valve signal for type A InSb device with wide CoFe injector (a) and narrow CoFe injector (b). The signal amplitudes are not dependent on the separations. In the upper graph, the induced voltage is measured at the narrow electrode, in the lower, at the wide electrode. A current of 10 μA is applied, but due to the higher interface resistance (InSb/CoFe), the effective current values are 6.06 μA for the wide CoFe electrode and 4.85 μA for the narrow one.

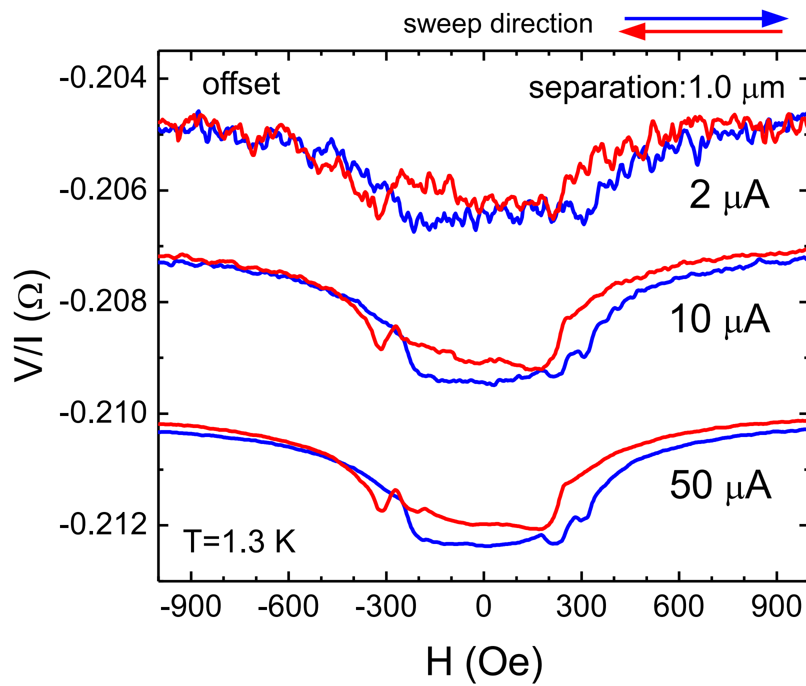

Figure 5.7: Non-Local spin valve signal with three different applied current on type C device. Data is offset for clarity.

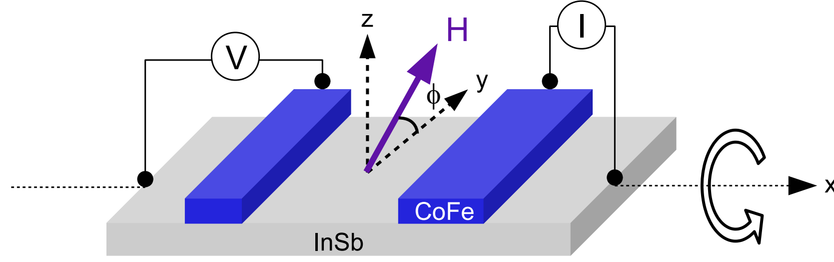

Figure 5.8: Schematic diagram showing the mechanism of tilting the sample to obtain varying out of plane magnetic fields, as well as measurement configuration.

5.2.2 Tilting Angle Dependence

Earlier, we saw that for the interface MR signals, the in-plane angle dependence is weak (Fig. 4.5 (a)). At a fixed temperature, the magnitude of the external magnetic field and the magnetization of the CoFe electrode are two important factors contributing to the observed signals. In this section, the dependence of the out of plane magnetic field is presented. The tilting of the direction of the applied magnetic field is accomplished by rotating samples along the $\hat{x}$-direction as described in Fig. 5.8. For the type A LSV, the magnetic field sweeps from -7500 Oe to 7500 Oe; 7500 Oe magnetizes the CoFe electrodes. Rotating the angle from 0° to 70°, the magnetization switching field -900 Oe for the 200 nm CoFe electrode- lies in the range of the field sweep as the effective in-plane magnetic field ($H_y = H\cos\phi$) is larger than the the coercive fields of the CoFe electrodes. The directions of the magnetization at low field ($< H_c$) are opposite for the forward and backward sweeps. We note that for the 90° traces, the CoFe electrodes are magnetized at -7500 Oe. For the type C LSV, the magnetic field sweeps from -500 Oe to 500 Oe, where the maximum field is smaller than the coercive field of the CoFe electrodes. The two CoFe electrodes are initially magnetized at 23000 Oe so that the magnetization of the CoFe electrodes is fixed when the magnetic field sweeps are applied. Fig. 5.9 (a), and (b) show the non-local signal for both type A (Fig. 5.9 (a)) and C (Fig. 5.9 (b)) LSVs geometries as a function of varying tilting angle, performed at 1.3 K. The applied current is 10 μA for both LSVs. In the type A LSV, the H_c and ΔR_s do not appear to depend on the tilt angle. In the type C LSV, H_c and ΔR_s also appear not to depend on tilt angle. However, we notice a difference in the hysteretic behavior of the traces in Fig. 5.9 (a) versus those in Fig. 5.9 (b). For the traces in Fig. 5.9 (b), the sample (LSV type C InSb) is exposed to a small magnetic field sweep range, where the mag-

netization of the CoFe is not changed due to the external field. For the LSV traces in Fig. 5.9 (a) in type A InSb, the sample is exposed to a large magnetic field sweep range, influencing and changing the magnetization of the CoFe. Thus in Fig. 5.9 (a), we observe almost no hysteretic behavior and a rather symmetric signal, even when the tilt angle is varied. In Fig. 5.9 (b), we observe non-symmetric behavior and variation as a function of tilt angle. Our InSb spin system is polarized in the $\hat{y}$-direction because the spins are injected from the magnetized CoFe, which here is fixed for both sweeps. The spin polarization is affected by the application of a perpendicular magnetic field ($\hat{z}$-direction) due to the spin precession. The direction of the magnetic field determines the direction of the spin precession. In short, we are changing the spin precession axis while keeping the magnetization fixed in Fig. 5.9 (b), and the changes among the traces in Fig. 5.9 (b) are thus due to spin precession only.

5.2.3 Temperature Dependence

We discussed the temperature effect on the InSb/CoFe interface in Chap. 4, which strongly supports the ferromagnetic phase model presented. In Fig. 5.10 (a), the non-local type C LSV MR signal shows temperature dependence in the range of 1.2-4.4 K, where ΔR_s and H_c decrease linearly as temperature increases. In Fig. 5.10 (b) and (c) we plot ΔR_s versus T and H_c versus T, respectively, to highlight the decrease of both ΔR_s, and H_c as a function of T. The trends in Fig. 5.10 (b) and (c) mirror those depicted in Fig. 4.11, indicating again interface MR phenomena. Here, both H_c and ΔR_s disappear at $\sim$3.2-3.5 K, which is comparable to the interface MR result. The hysteresis presented in H_c also diminishes with increase temperature. This temperature dependence is a unique property of the InSb/CoFe interface studied by us. Our observations of the same property in non-local geometry supports the detection of spin currents.

5.2.4 Bias Dependence

A DC bias is applied at the injector interface of type C LSV, which changes the population of spins in the InSb channel. Detection of a bias dependent signal in the non-local geometry is evidence of spin transport [33, 56]. Such a bias tunability is a useful tool for spin manipulation. Fig. 5.11 (a) shows our bias measurement configuration, in which the narrow CoFe electrode from the 0.8 μm LSV is used

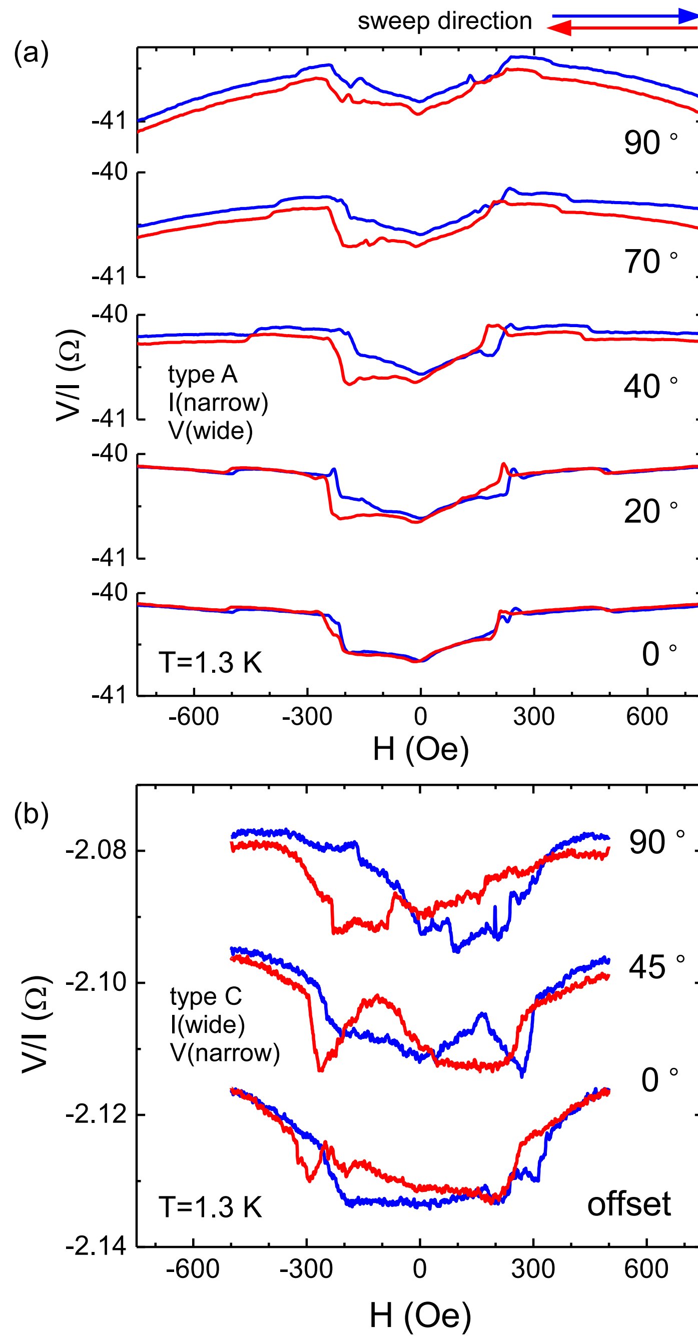

Figure 5.9: (a) Tilting angle dependence on LSV signal of type A device (1.5 μm separation) and (b) type C device (1.0 μm separation). In (a), the magnetization of the CoFe is allowed to vary, in addition to the tilt angle, resulting in almost symmetric behavior. In (b), the magnetization of CoFe is fixed, and we observe a non-symmetric behavior arising from varying the spin precession axis as a function of tile angle.

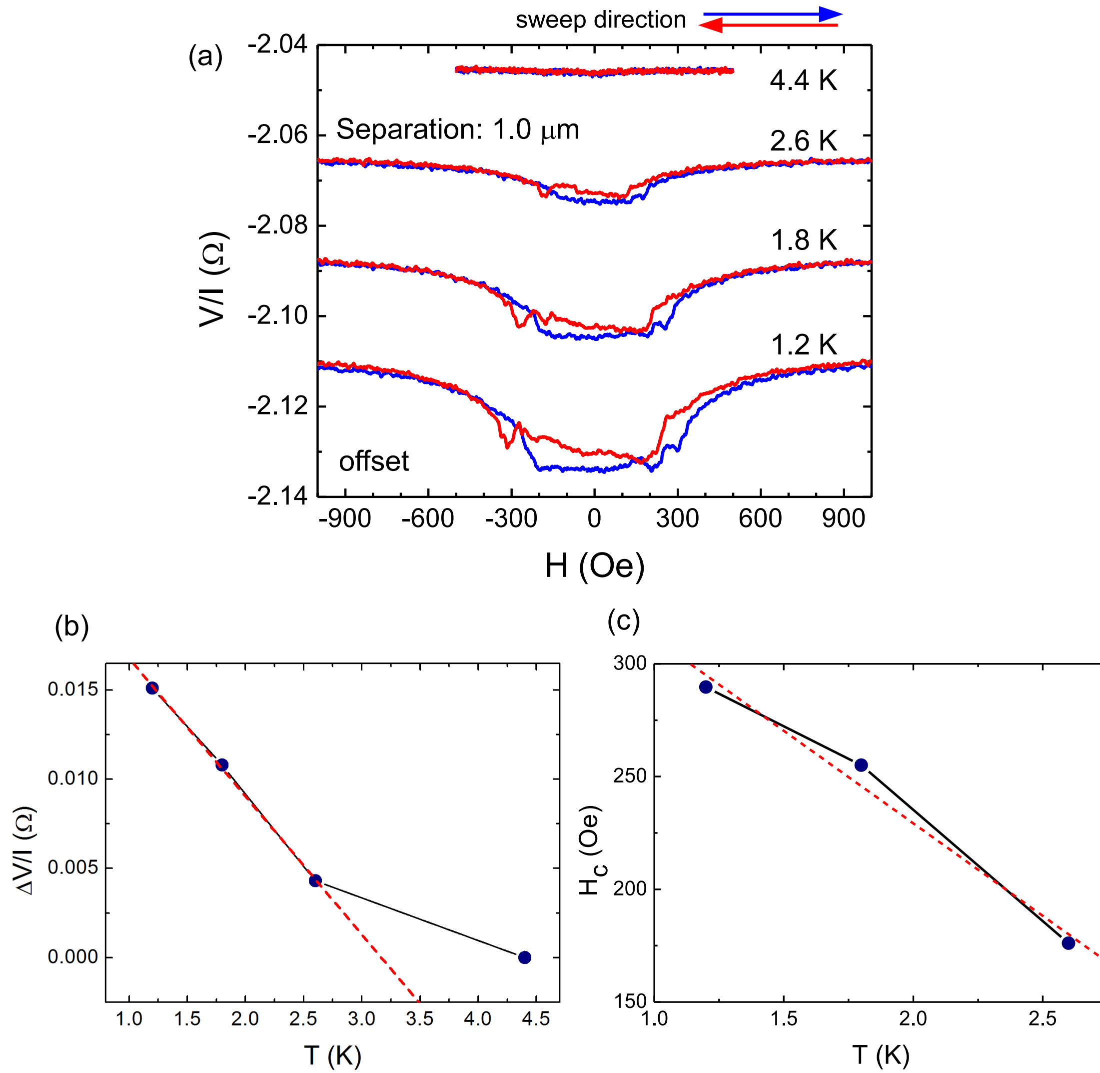

Figure 5.10: (a) Temperature dependence of the type C InSb/CoFe spin valve signal. Signal amplitude variation as a function of temperature, ΔR_s vs T (b) and H_c vs T (c). In both (b) and (c), the MR signal amplitude decrease as T increases, with an extrapolated T value of ~ 3.5 K.

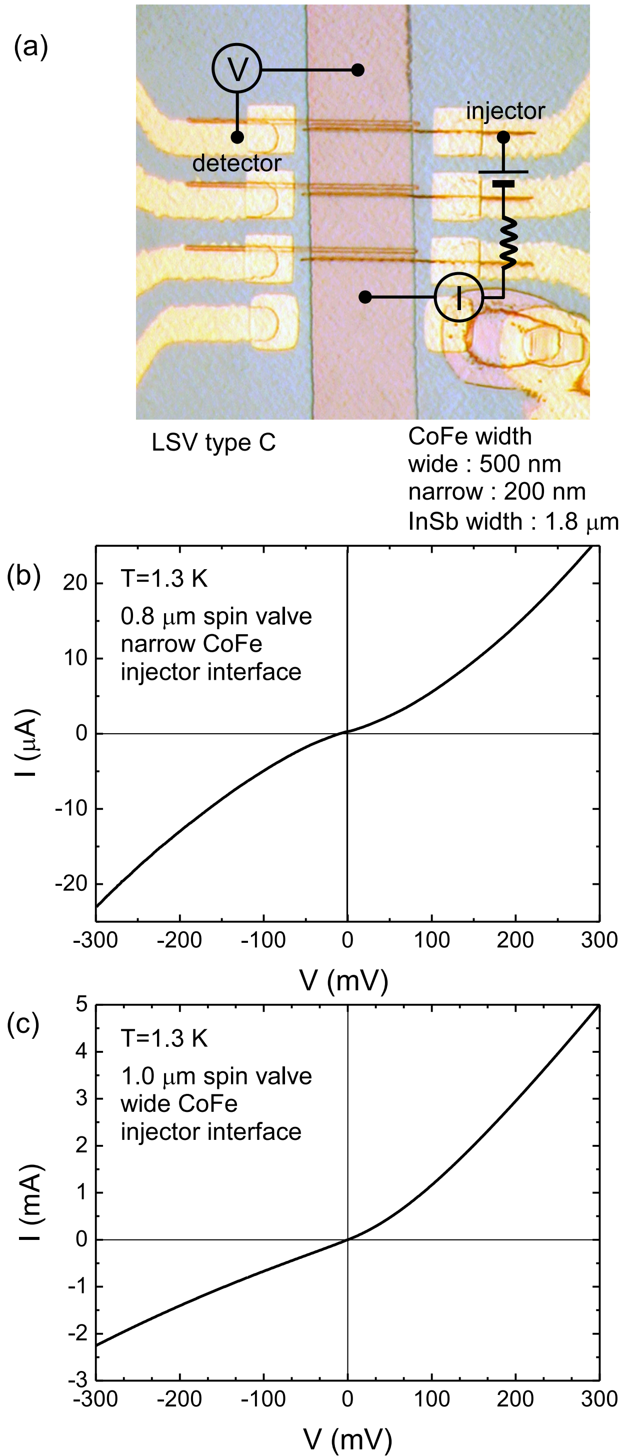

Figure 5.11: (a) Micrograph of type C LSV with bias configuration as described. I-V trace of the interface; (b) narrow CoFe bar of the 0.8 μm LSV, and (c) wide CoFe bar of the 1.0 μm LSV.

as the biased injector. The 1.0 μm LSV is also measured, with the wide CoFe as the biased injector. As the I-V measurements of Fig 5.11 (b) and (c) indicate, the InSb/CoFe interface of the 0.8 μm LSV injector develops a Schottky type barrier, recognized as a required condition for efficient spin injection [57, 58].

Fig. 5.12 (a) shows an example of the narrow CoFe injector spin valve signal with a 125 mV bias. The R_s shows the same shape as the unbiased signal, except here the signal amplitude changes. From the injector bias experiment, we observe that ΔR_s varies as a function of applied bias, as shown in Fig. 5.12 (b). For large DC bias ($V_{bias} < -20$ mV and > 40 mV), ΔR_s increases as $|V_{bias}|$ increases. Note that ΔR_s begins to level off as $|V_{bias}|$ becomes very large. In the range -20 mV $< V_{bias} < 40$ mV, ΔR_s increases as the $|V_{bias}|$ approaches to zero (inset Fig. 5.12(b)).

The non-local signal measured in the 1.0 μm LSV with the wide CoFe electrode as the injector also depends on the injector bias as shown in Fig. 5.13. Notice at zero bias, LSV signal shows an enhanced hysteresis and the signal level shifts for different sweep directions for $|H| < 300$ Oe. This is different from the same measurement presented in Fig. 5.5, which we attribute to a change in the interface characteristics due to repeated cool-down processes. The H_c remains at $\sim$300 Oe and does not depend on the bias. However, the signal with the bias shows a change in ΔR_s, as indicated in Fig.5.14 (a) and (b), where ΔR_s versus bias is shown for the forward sweep (blue) and the backward sweep (red), respectively. Two types of amplitudes are extracted. In Fig.5.14 (a), the circles represent the difference between the $R_{s,\mathrm{baseline}}$ and $R_{s,H=0}$. In Fig.5.14 (b), the squares represent the difference between the $R_{s,\mathrm{baseline}}$ and $R_{s,\mathrm{peak}}$. The $R_{s,\mathrm{peak}}$ is measured at 250 Oe and at -300 Oe for the forward and backward sweeps, respectively. Both traces show a maximum in ΔR_s at around zero bias. The traces of $R_{s,\mathrm{background}} - R_{s,H=0}$ are suppressed as $|V_{bias}|$ increases in the range of $|V| > 30$ mV, which is consistent with the narrow injector bias dependence experiment. For larger bias, the amplitude diminishes to zero. The overall features of the bias dependence for both sweep directions are similar, with only a 2-3 mΩ difference. Interestingly, the R_s measured at low field have a higher value than the background signal with -15 mV $< V_{bias} < 20$ mV bias, which suggests a contribution of the interfacial characteristic to the non-local spin valve signal.

5.3 Spin Current

We attribute the origin of the signals from the non-local measurement of the LSVs to the spin current due to following observations. Firstly, the signal features of the

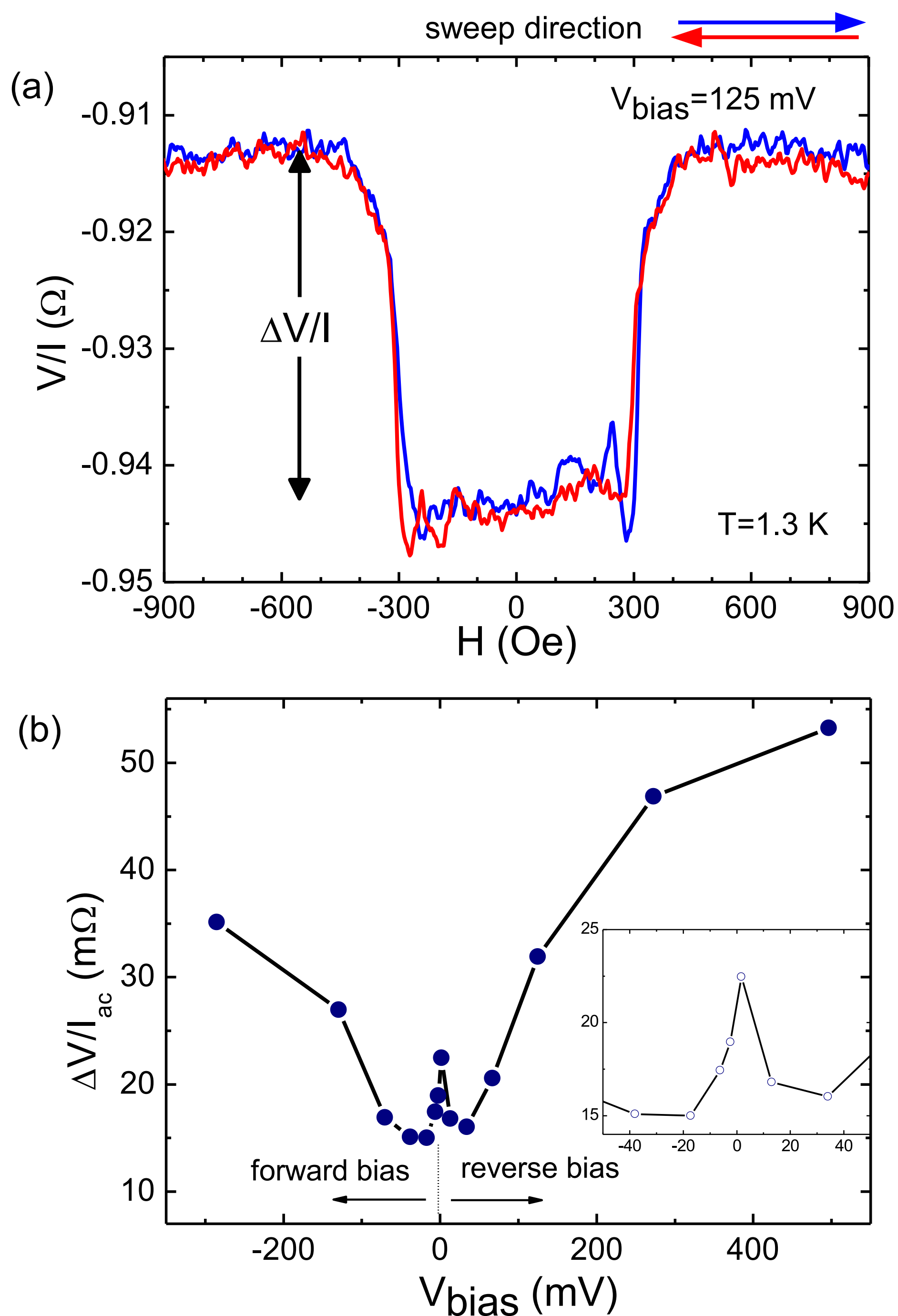

Figure 5.12: (a) Non-local signal of type C InSb LSV separated by 0.8 μm. Narrow CoFe bar (200 nm) injector is biased at 125 mV. (b) Signal amplitude versus applied DC bias voltage. Inset: magnification at low V_{bias}.

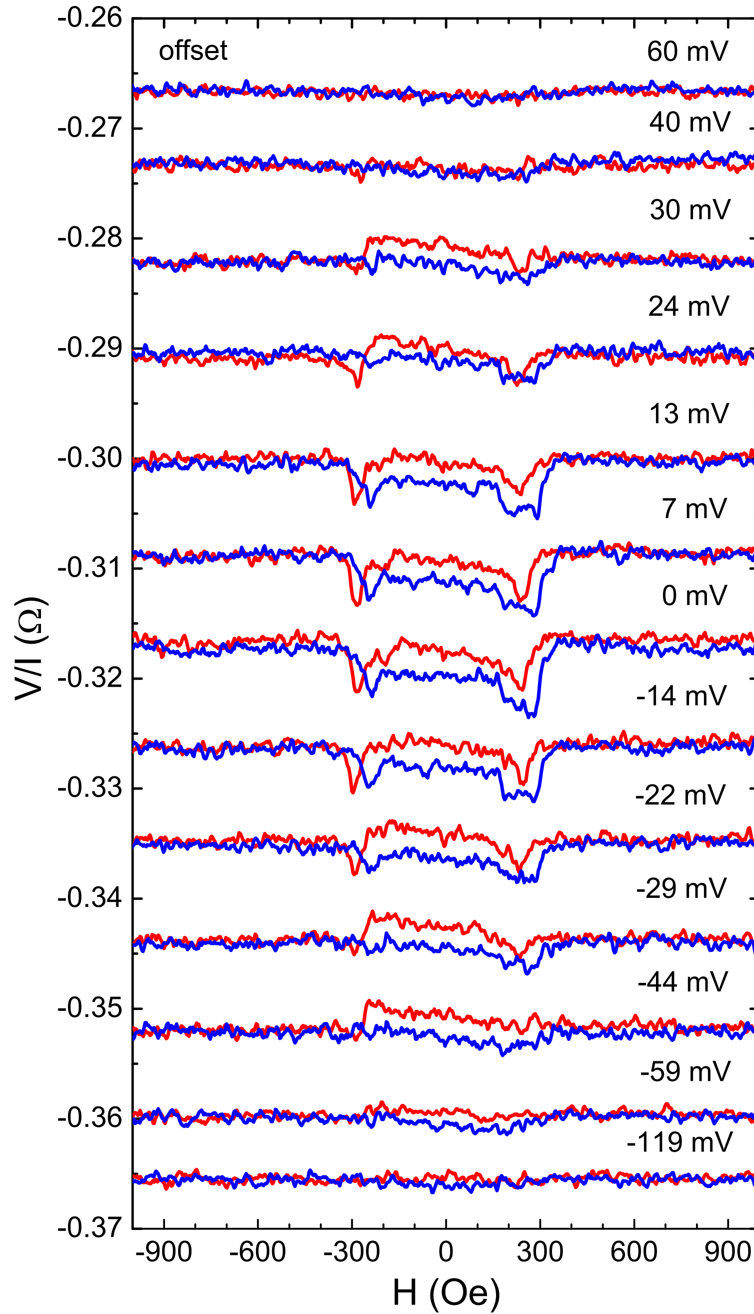

Figure 5.13: Non-local signal of type C InSb with 1.0 μm separation LSV. Using the wide CoFe electrode (500 nm) as injector, several DC bias voltages are applied to InSb/CoFe injector interface, and resulting MR signals plotted. Data is offset for clarity.

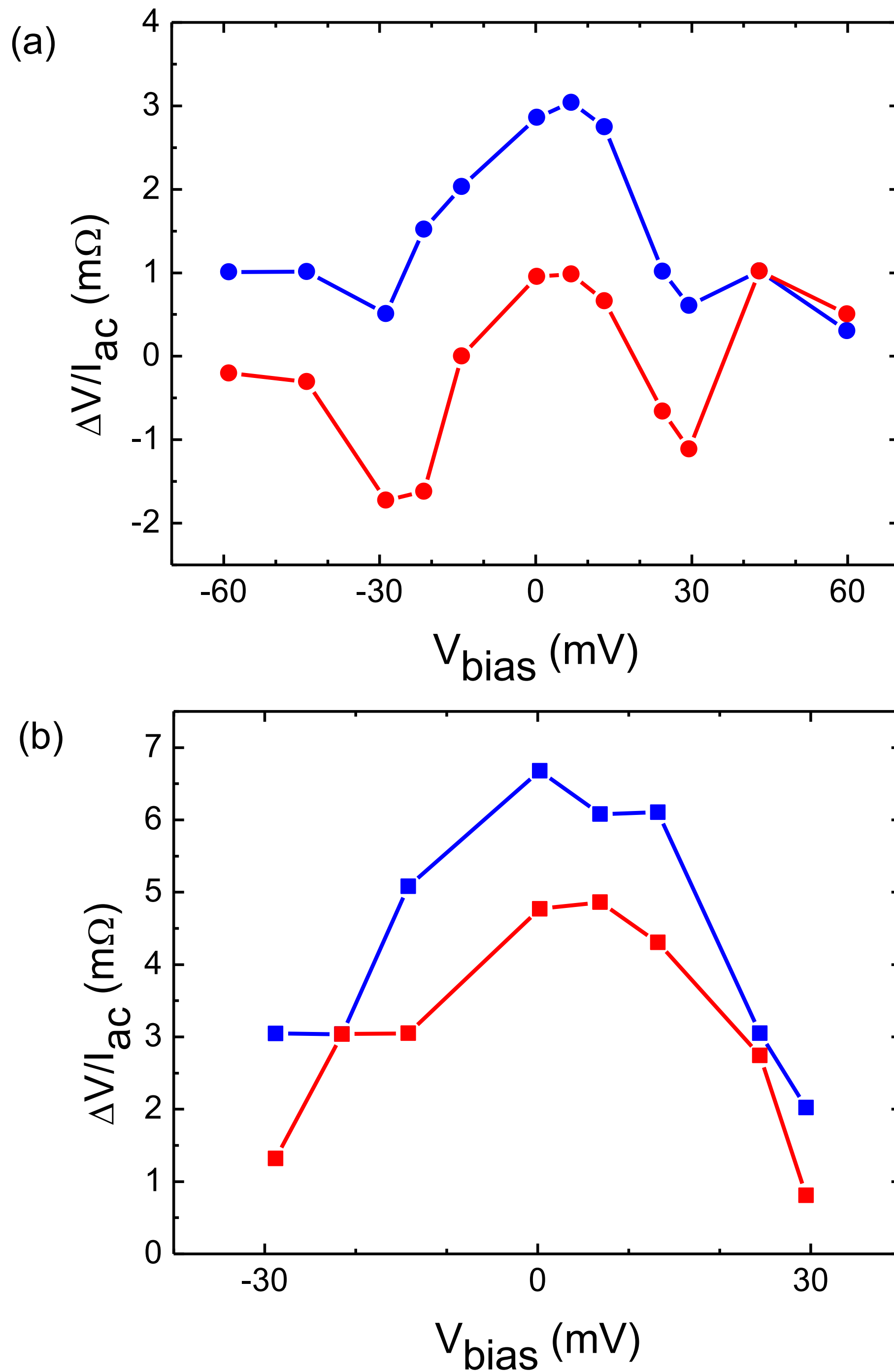

Figure 5.14: Variation of ΔR_s as a function of bias voltage. (a) $R_{\text{baseline}} - R_{H=0}$ versus V_{bias}. (b) $R_{\text{baseline}} - R_{\text{peak}}$ versus V_{bias}. The R_{peak} measured at ∼250 Oe and ~ -300 Oe for forward (blue) and backward (red) sweeps, respectively.

LSV are the same as the interface MR results presented in Chap. 4. The negative ΔR_s and baseline $R_{s,0}$ values are due to the direction of the current induced by the spin accumulation at the detector interface. This current flows from the InSb to the CoFe in the detector when the applied current is driven from the CoFe injector into the InSb. Therefore, both signal features are the same. Furthermore, the H_c in the LSV signals is the same as the H_c of the interface MR signals. As we discussed in Chap. 4, H_c is a property of the ferromagnetic phase that determines the magnitude of the response to the external magnetic field. Secondly, the non local LSV signals are dependent on temperature, which is consistent with the interface MR features. The temperature dependence in the range of 1.2-3.5 K is a unique characteristic of the interface MR reported here. Thirdly, the injector bias dependence in the non-local geometry is a signature of a pure spin current. Fourthly, the signals are dependent on the exact interfaces, exemplified when the injector and the detector are exchanged. Lastly, the non-local LSV signals with the magnetized CoFe are dependent on the direction of the perpendicular magnetic field, influencing the spin precession.

Chapter 6

Spin Transport in InSb Hall Devices with CoFe Electrodes

In this chapter, we will study the spin transport in InSb Hall devices with CoFe electrodes. The Hall and MR experiments in a simple Hall structure are a powerful tool to study the carrier transport properties. We introduce the ferromagnetic CoFe in a InSb Hall structure as a spin source to drive a spin current into the InSb. The Hall and MR measurements of the InSb/CoFe Hall structure will give insight on the spin transport mechanisms in strong SOI material InSb.

6.1 InSb/CoFe Spin Transport I

6.1.1 Device Design and Fabrication I

Two devices are fabricated from the InSb film type A and CoFe to investigate the spin transport. The devices consist of a patterned InSb film and a single CoFe electrode, which is deposited near a Hall cross. Two etching steps, following photolithography and EBL form Hall crosses as depicted in Fig. 6.1 (a). The CoFe electrode (thickness of 55 nm) is thermally evaporated on the top of the InSb pattern. A Au contacting layer (thickness 130 nm) is also deposited by thermal evaporation. The distance of the CoFe edge from the center of the near Hall cross is 1-2 μm. Fig. 6.1 (b) shows the lithographical dimensions of the device: the center to center distance between the two Hall crosses is $\sim$10 μm, the distance between the Hall cross near CoFe and the far

contacts is 120 μm, and width of the InSb transport channel is 8 μm. Although, the width of the CoFe electrode is 16 μm as depicted in Fig. 6.1 (a), we assume that only the CoFe deposited on the top of InSb (8 μm width) contributes to the measurement. The aspect ratio of the CoFe electrode is about 9. Due to the large resistance of the InSb/CoFe and/or CoFe/Au contacts, the actual current in the CoFe/InSb interface is 4-60% of the expected current. For example, the measured actual currents are 419 nA, 182 nA and 31 nA for the expected currents 10 μA, 1 μA, and 50 nA each. The multiple etching steps underneath the Au layer could cause a weak connection with the CoFe electrode. On the other hand, this could be a genuine property of the CoFe/InSb interface. The *I-V* behavior is non-ohmic. The external magnetic field is applied along the length direction of CoFe electrode.

6.1.2 Hall Measurement with In-Plane Field

A local Hall resistance is measured in the Hall cross with an in-plane magnetic field at low temperature (1.3 K). A in-plane magnetic field is aligned with the longitudinal direction of the CoFe electrode. The magnetic field sweeps from -10000 Oe to 10000 Oe. Fig. 6.2 (a) and (b) shows the Hall signal at the Hall cross near the CoFe electrode and at the Hall cross 10 μm away from the CoFe electrode. An 1 μA current is applied in the InSb transport channel, which flows under the CoFe electrode. Hysteresis is present in the Hall signal (R_{xy}) at the near cross, which is due to the fringing field from the edge of the CoFe electrode. No signal is present in the far Hall cross because the fringing field decays rapidly. On both graphs, the Hall slopes are subtracted for clarity. The observed switching field is 300-500 Oe and the difference of the Hall resistances (ΔR_{xy}), measured at high field where R_{xy} is linear, is 3.3 Ω. The calculated averaging fringing field in the Hall cross is 44 Oe. The saturation magnetization of the CoFe electrode is $M_s = 1.7 \times 10^6$ A/m (1700 emu/cm^3) calculated by the magnetic model as discussed in Sec. 3.2.

When an 1 μA current is applied between the CoFe and InSb as shown in the inset of Fig. 6.3 (a) and (b), the Hall measurement shows the magnetic field dependence in the near Hall cross and no dependence in the far Hall cross where neither the fringing field and the spin current are expected because of $\sim$10 μm distance. As shown in Fig. 6.3 (a) at the higher field ($|H| >$300 Oe), the R_{xy} stays constant after subtracting the Hall slope. ΔR_{xy}, the Hall resistance difference measured between high positive field and high negative field, is 3.1 Ω which is comparable to the Hall signal with current under CoFe. In addition, the difference of the Hall resistances at zero field for the forward sweep (blue) and backward sweep (red) is 2.6 Ω, which is

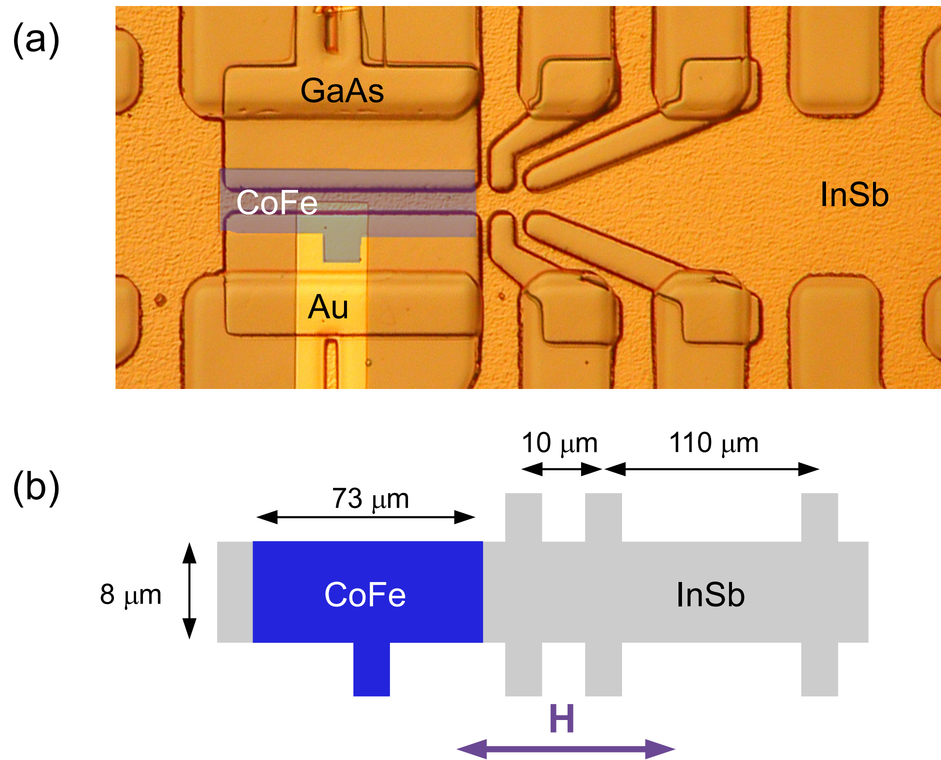

Figure 6.1: (a) Micrograph of the InSb/CoFe spin transport device. The CoFe layer is highlighted with blue color. (b) Lithographic dimensions of the device.

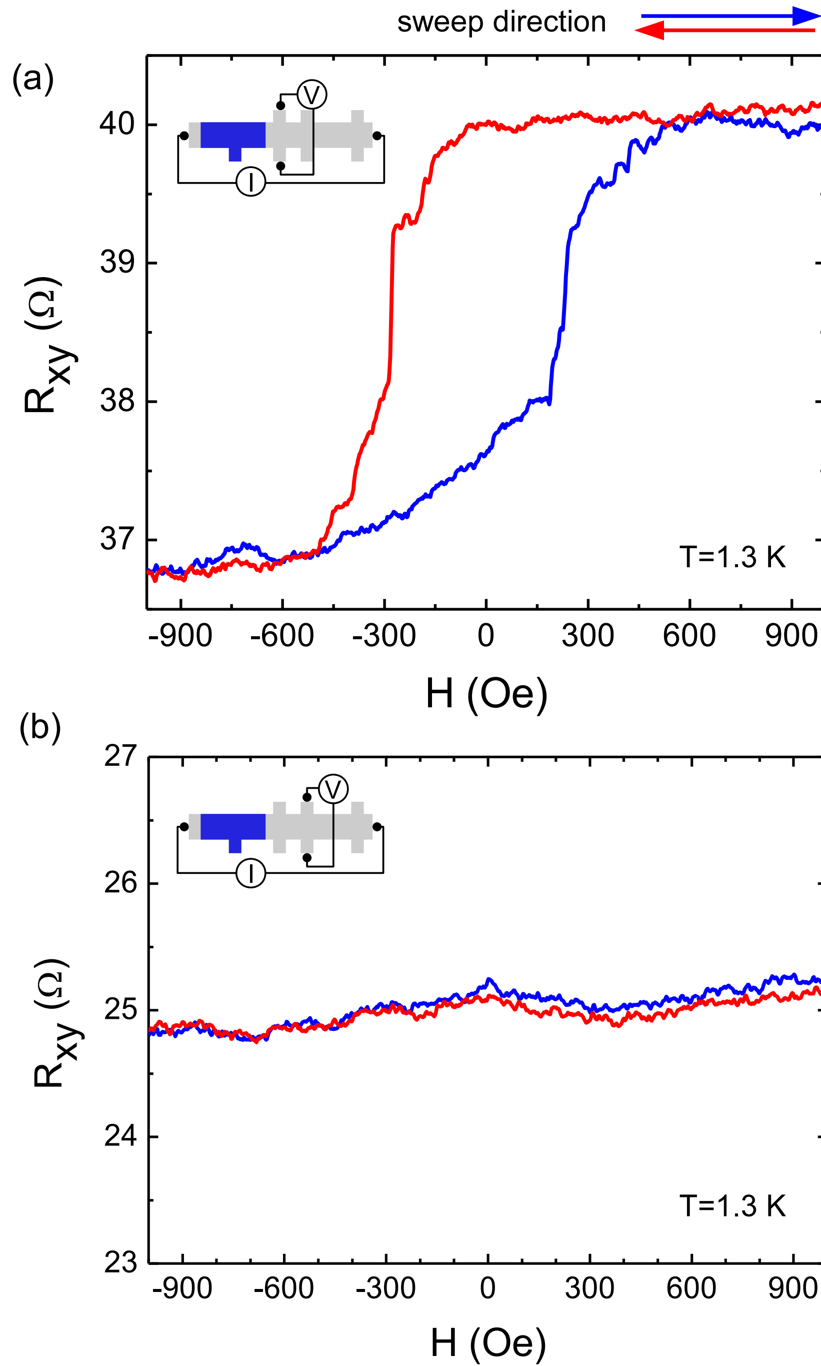

Figure 6.2: (a) Hall resistance measured in the Hall cross near the CoFe electrode with in-plane external magnetic field. Current I applied through InSb channel under the CoFe layer. (b) Hall measurement at the far Hall cross as a control, 10 μm away from near Hall cross, shows no noticeable signal. Hall slopes are subtracted for clarity.

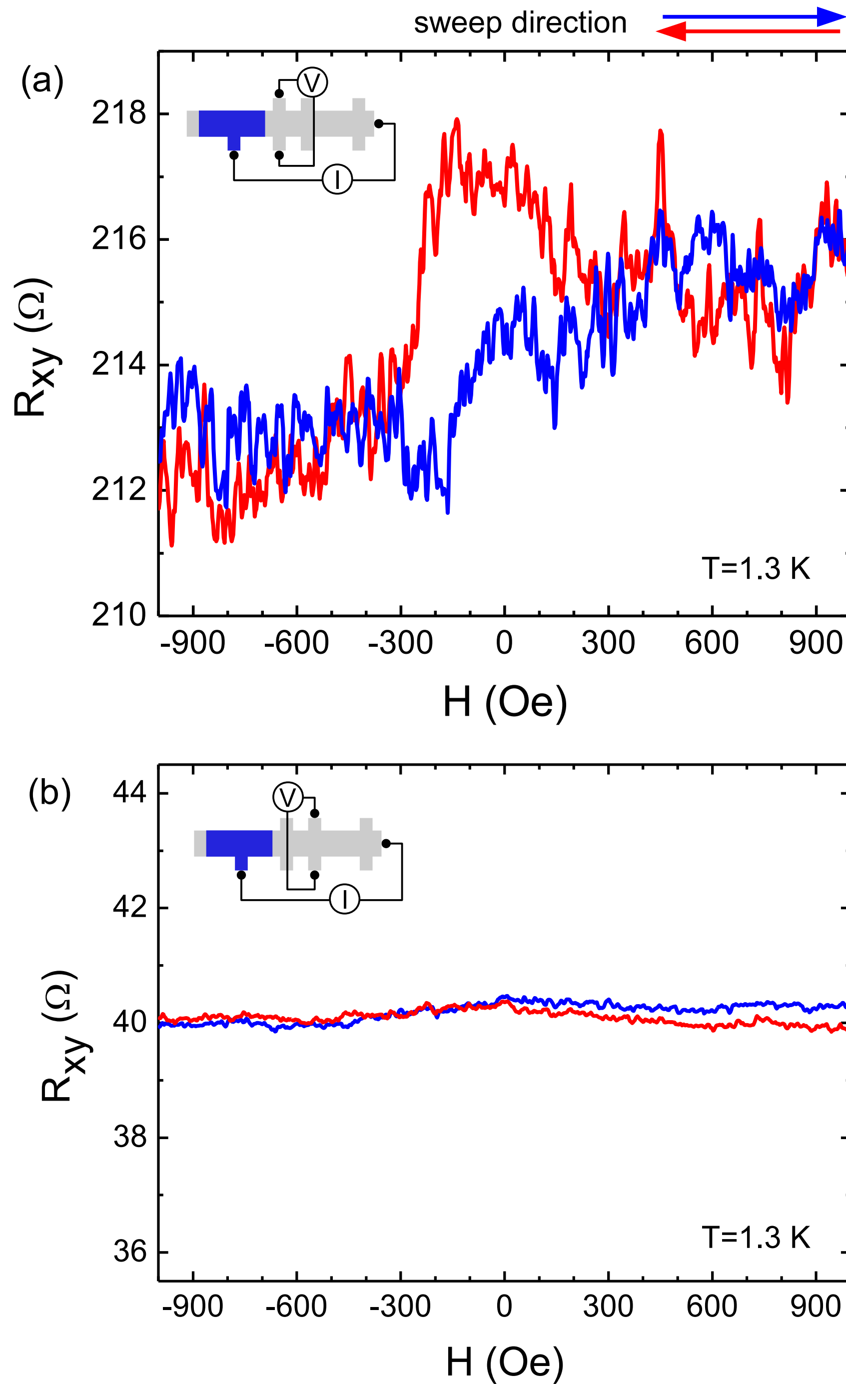

Figure 6.3: (a) Hall resistance measured in the Hall cross near the CoFe with in plane external magnetic field. Current I applied through the InSb/CoFe interface. (b) Hall measurement at the far Hall cross as a control, 10 μm away from the near Hall cross, shows no signal. Hall slops are subtracted for clarity.

also comparable to the 2.5 Ω from the Hall measurement with the current under the CoFe electrode. However, at low field ($|H| < 300$ Oe) where the hysteresis appears, the signal has a different signature. For both sweeps, the signals are shifted by about 1.6 Ω. Such a signal shift could be due to a contribution from the interface MR as we observed in Chap. 4 or simply by noise caused by the resistive contact.

6.1.3 Magnetoresistance Measurement with Perpendicular Field

Fig. 6.4 presents the MR results probed at the two top contacts (Fig. 6.4 insets) with 120 μm separation. A perpendicular magnetic field with a small sweep range (-50 Oe$< H <$ 50 Oe) is applied. Insets of Fig. 6.4 (a) and (b) show the different current configurations. A 50 nA current flows under the CoFe bar (a) and through the CoFe bar (b). On both graphs, WAL signals are present, which show a reduction of the distance of two peaks when the CoFe bar magnetized. For charge carriers with spin (s=1/2), the WL correction to the conductivity is given by Eq. 6.1,

$$\Delta\sigma = -\frac{1}{4}(-S_0 + \sum_{i=-1}^{1} T_{1,i} - \ldots) \tag{6.1}$$

Where S_0 is the singlet contribution and $T_{1,i}$ is triplet contribution to the conductivity. The ferromagnetic alignment or spin polarization reduces WAL because it suppresses the singlet component, $\frac{1}{\sqrt{2}}(\uparrow\downarrow - \downarrow\uparrow)$. The average ferromagnetic magnetization would also suppress antiparallel spin configurations, the singlet and one of the triplets [59], $\frac{1}{\sqrt{2}}(\uparrow\downarrow - \downarrow\uparrow)$, $\frac{1}{\sqrt{2}}(\uparrow\downarrow + \downarrow\uparrow)$, resulting WAL suppression. Therefore, the WAL suppression is due to the CoFe magnetization.

6.2 InSb/CoFe Spin Transport II

6.2.1 Device Design and Fabrication II

The resistive InSb/CoFe contact in the Hall device for Sec. 6.1 might have caused the low current and added noise to the signal. Due to the thickness of the InSb film, there must be at least a 1.55 μm gap between the InSb surface and the GaAs substrate

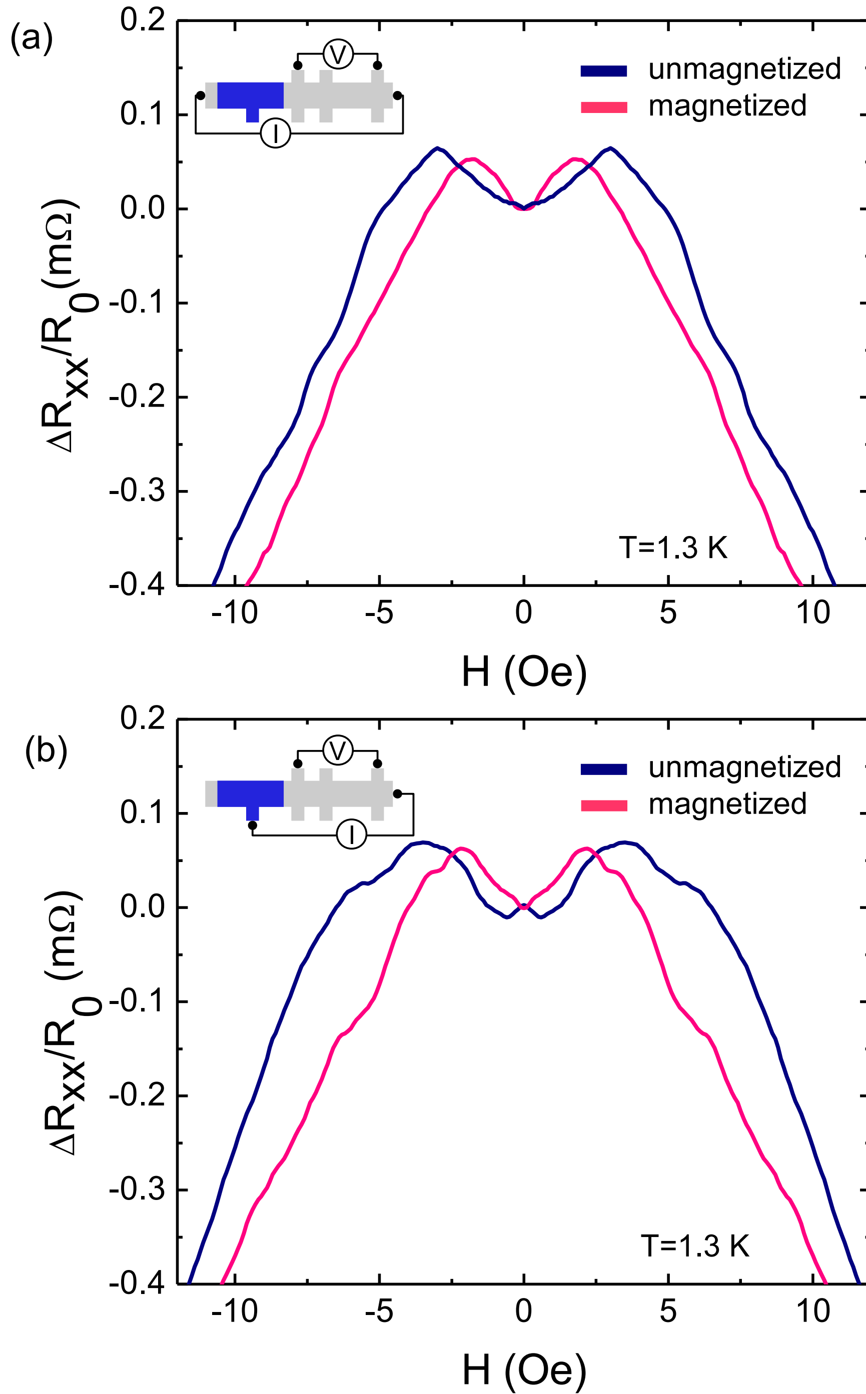

Figure 6.4: (a) MR in the InSb channel with a small perpendicular external magnetic field. Current flow under CoFe. WAL signal is suppressed when the CoFe is magnetized. (b) MR in the InSb channel with a small perpendicular external magnetic field. Current applied through the InSb/CoFe interface.

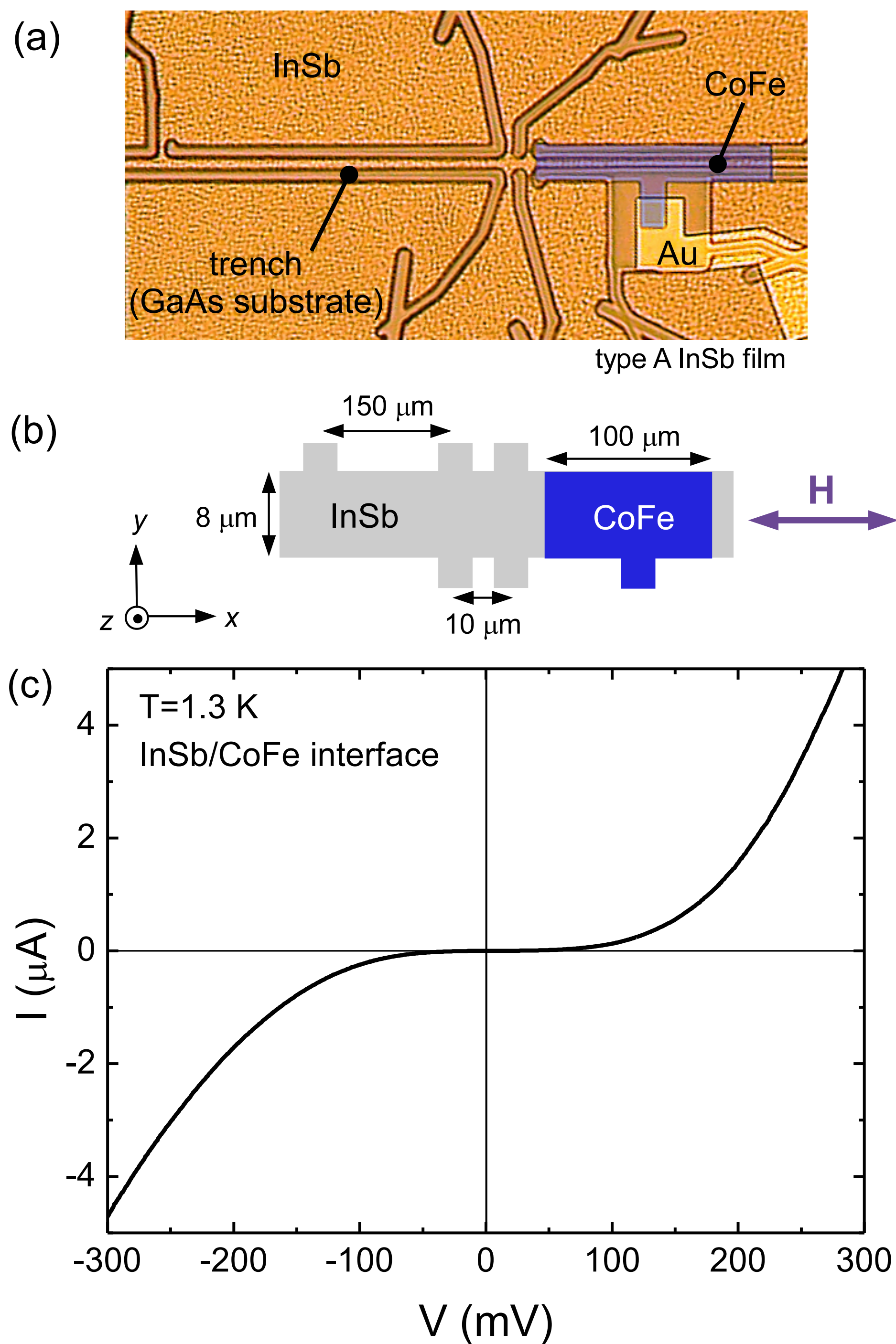

Figure 6.5: (a) Micrograph of the InSb/CoFe spin transport device patterned by EBL and wet etching. Then a CoFe electrode and Au contact layers are deposited. (b) Schematic of the device with lithographic dimensions. (c) I-V trace of the InSb/CoFe interface.

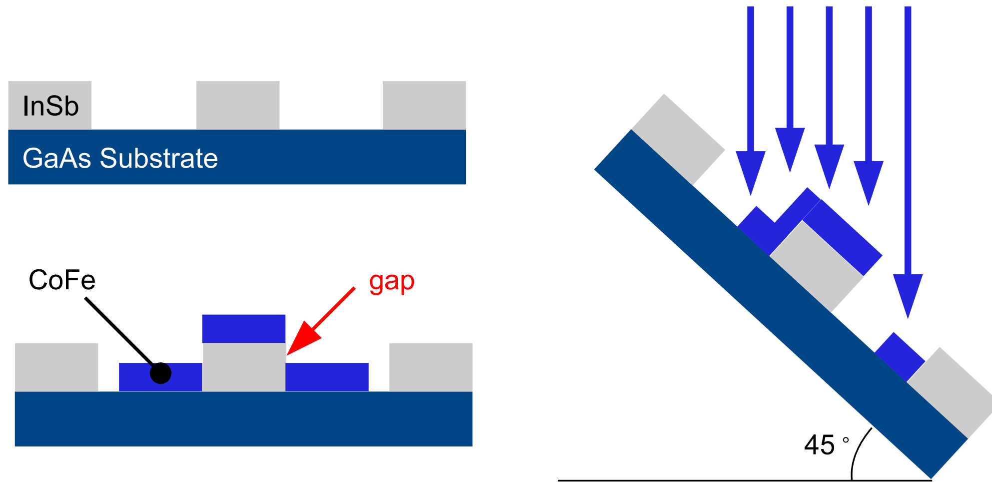

Figure 6.6: Schematic of the tilted evaporation.

surface. In the Hall device structure, the CoFe electrode is deposited on both the InSb and substrate surface. Therefore, there could be a region at which the CoFe cannot be reached due to the smaller thickness (55 nm) of the CoFe electrode than that of the InSb. In other word, the CoFe electrode could be disconnected on the side of mesa, which could cause a highly resistive signal. Several fabrication methods are tried to minimize this disconnection problem. The fabrication procedure of the first device (Sec. 6.1) includes two etching steps, which could cause a disconnection problem on the side of mesa. The fabrication of the second spin transport device introduces two methods to avoid the disconnection problem, which would improve the conductivity of the CoFe electrode if the conductivity problem is from a slight disconnect. On the other hand, if the CoFe bar still has a high resistance, the measurement results from the first device with current flowing through CoFe must be an interface property. The first method is to decrease the number of etching steps by employing a single EBL step for etching. As shown in Fig. 6.5 (a) the trenches formed by EBL and etching define the InSb mesa including the Hall crosses. The second method is a tilted evaporation of CoFe, as depicted in Fig. 6.6. Tilting the sample by 45° lets CoFe be deposited on the side of mesa. Au contact pads are deposited in the trench and contacted with the CoFe pattern. The lithographic dimensions of the device are depicted in Fig. 6.5 (b). The thickness of the CoFe electrode is again 55 nm.

6.2.2 Hall Measurement with In-Plane Field

The Hall resistance is measured at the Hall cross near the CoFe electrode and at the cross 10 μm away, at 1.3 K. A 1 μA current is applied in the InSb channel under the CoFe electrode. An in-plane magnetic field along the CoFe length sweeps from -10000 Oe to 10000 Oe . In the Hall cross near the CoFe, the magnetic field dependence is due to the fringing field from the CoFe edge, as shown in Fig. 6.7 (a). The observed switching field is 650-750 Oe and the calculated fringing field is $\sim$19 Oe from ΔR_{xy} =1.4 Ω, which is different from the result obtained in the first spin transport device (switching field: 300-500 Oe, fringing field: $\sim$44 Oe), although both devices have very similar structures (CoFe: 8$\times$73 μm for first device, 8$\times$100 μm for second device, InSb: 8 μm width for both devices). These differences could be due to misalignment between cross and CoFe electrode, or due to misalignment between the CoFe electrode and in-plane magnetic field. The fact that the calculated saturation magnetization of CoFe electrode for this device is 0.7$\times 10^6$ A/m (700 emu/cm^3) is supportive evidence. Fig. 6.7 (b) shows the Hall resistance at the other Hall cross. The data is antisymmetrized to remove the MR signal caused by the misalignment of the contacts. A spin signature and a fringing field effect are not present. The subtracted Hall slopes measured at both Hall crosses are comparable, as indicated in Fig. 6.7 (a) and (b).

Fig. 6.5 presents the *I-V* characteristic of the CoFe/InSb interface, where a Schottky tunnel barrier is clearly developed. Fig. 6.8 (a) shows the results of the Hall measurement with a 1 μA current applied through the CoFe/InSb interface. The hysteretic behavior of the signal due to the fringing field is observed. The switching field is $\sim$650 Oe and ΔR_{xy} is $\sim$1.4 Ω. The results of the non-local Hall measurement with a 10 μA current is presented in Fig. 6.8 (b). In this case only pure spin current can exist in the Hall cross, due to the non-local configuration. Therefore, the detected hysteretic signal must be related to a spin signal. The direct spin Hall effect (DSHE) [60–64] is a transport phenomenon in which a charge current induces a transverse spin current by SOI. The inverse spin Hall effect (ISHE) [65–68] which is reciprocal effect of DSHE is described as Eq. 6.2,

$$\vec{E}_{\mathrm{ISHE}} = \left(\frac{\sigma_{\mathrm{SHE}}}{\sigma_{\mathrm{N}}^2}\right)\vec{j}_{\mathrm{s}} \times \vec{\sigma} \tag{6.2}$$

where σ_{SHE} and σ_{N} are the spin Hall conductivity and electric conductivity, respectively, and $\vec{\sigma}$ is the spin polarization vector. Therefore, an injected spin current with a particular spin polarization induces the electric field in the material, which may be

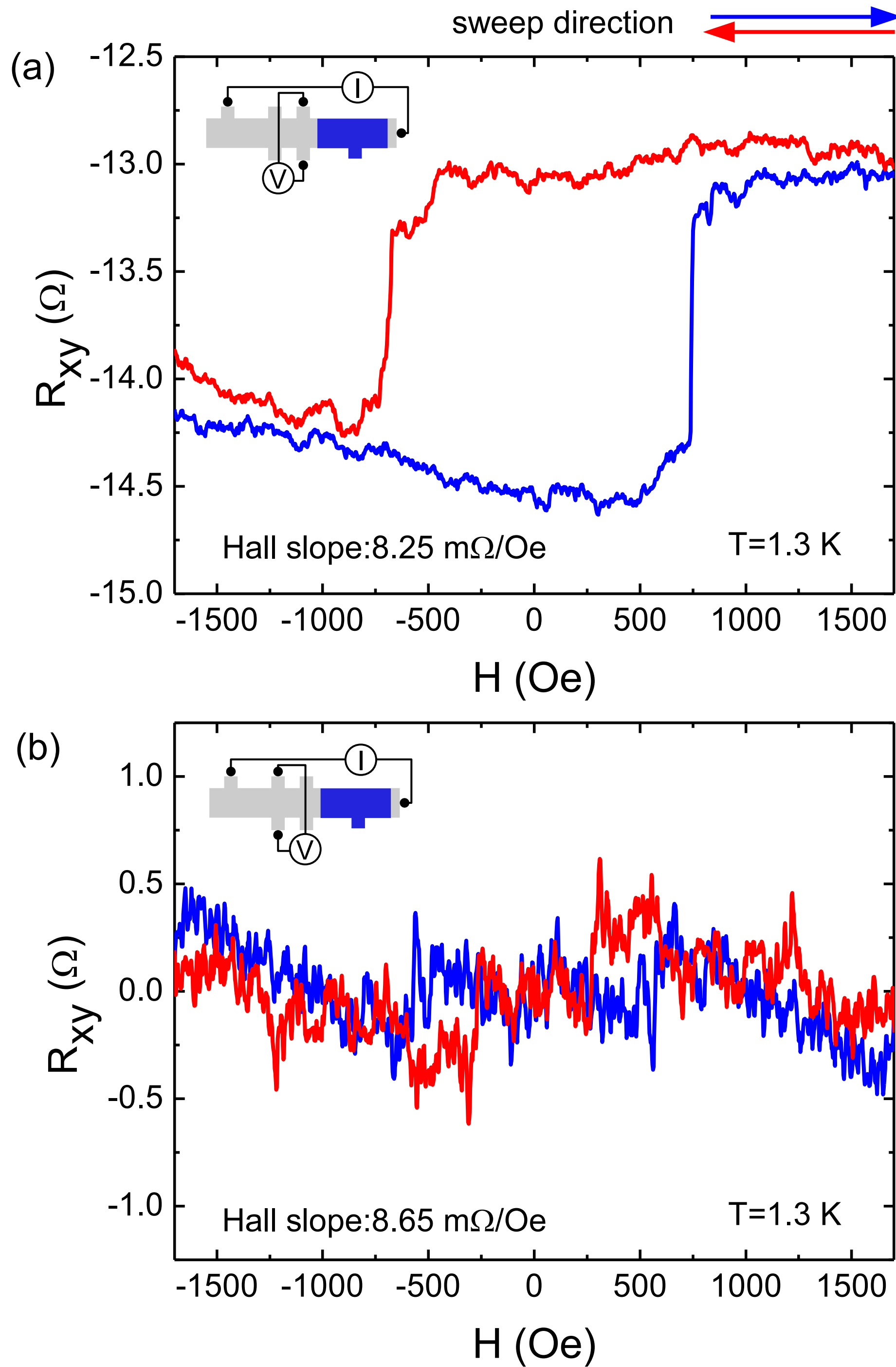

Figure 6.7: (a) Hall measurement result in the Hall cross near the CoFe bar with in-plane magnetic field along CoFe bar (Hall slope subtracted). (b) The far Hall cross data is antisymmetrized to remove MR signal.

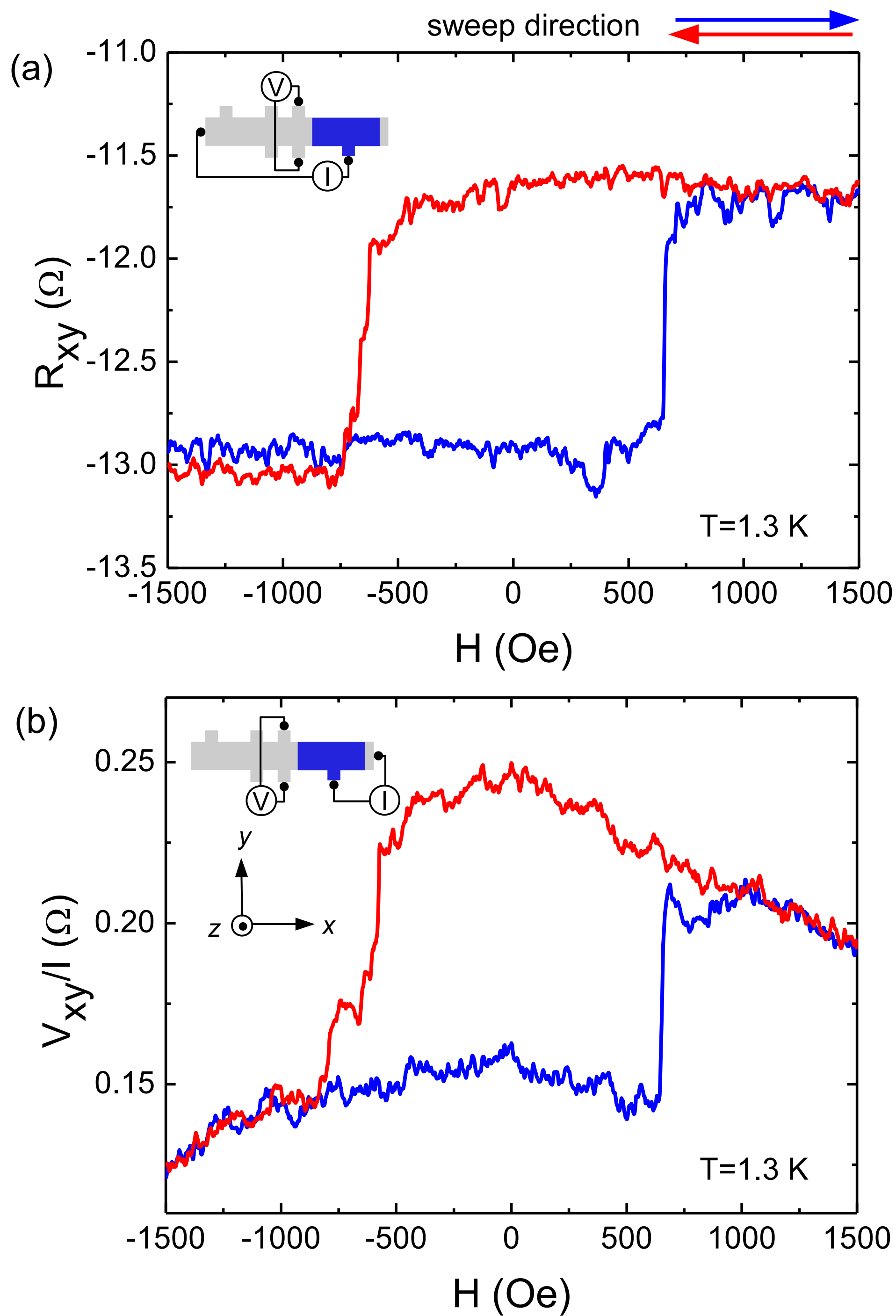

Figure 6.8: (a) Local Hall measurement in the Hall cross near CoFe. Current applied through the CoFe/InSb interface. (b) Non-local Hall measurement. Hall slopes are subtracted for clarity.

the origin of our signal. In the spin transport device geometry, the direction of induced charge current should be $\vec{j_{c,y}}$ to detect an induced electric field by ISHE in the Hall contacts. However, the directions of the spin current and the spin polarization, which is aligned to the direction of magnetization, are parallel, which would give zero charge current in Hall cross contacts, $\vec{j_{c,y}} \propto \vec{j_{s,x}} \times \vec{\sigma_x} = 0$. Here $\vec{j_c}$ is the charge current vector. However, the ISHE could play a role in the detected non-local Hall signal. First, the fringing field effects measured in the Hall cross near CoFe for two transport devices show different results, although both devices have the same structures (except the length of CoFe). Specifically, the second device shows an apparently smaller saturation magnetization value, which means mis-alignment of the magnetization with CoFe electrode could lead non-zero value of the $\hat{z}$-component of magnetization so that the direction of injected spin has same $\hat{z}$-component ($\vec{j_{c,y}} \propto \vec{j_{s,x}} \times \vec{\sigma_z} \neq 0$). Second, the effective magnetic field which is a sum of the fringing field and the external in-plane field, could shift of the direction of the spin toward the $\hat{z}$-direction by spin precession along the effective field. Thirdly, the SOI could also induce a change in the spin direction by spin precession.

In Fig. 6.9 (a), three types of Hall measurement results with different measurement configurations are plotted together. The non-local, current through CoFe, and current under CoFe traces are the configurations represented in inset of Fig. 6.8 (b), Fig. 6.8 (a), and Fig. 6.7 (a), respectively. The switching field is shifted depending on whether the current goes through the CoFe or under the CoFe, with a larger switching field when the current goes under the CoFe. The switching field of non-local trace is comparable to the switching field of current through CoFe trace. Therefore, the spin polarized current reduces the switching field. Fig. 6.9 (b) presents the difference between current through CoFe trace and the current under CoFe traces. The switching field shift due to the current flowing through the CoFe is $\sim$100 Oe.

6.2.3 Magnetoresistance Measurement with In-Plane Field

The non-local MR measured at the top contacts and bottom contacts are presented in Fig. 6.10 (a) and (b). The measurement configurations of the top contacts and bottom contacts are shown in the insets of Fig. 6.10 (a) and Fig. 6.10 (b), respectively, with a background subtracted. Interestingly, the detected signal on the top contacts mirrors the signal measured at the bottom contacts. The raw data plotted in Fig. 6.11 (a) shows the traces of this non-local MR result. This broken MR symmetry could be caused by broken time reversal symmetry (Onsager reciprocity relation), which means the detected signals are spin related. Moreover, the non-local MR is possibly

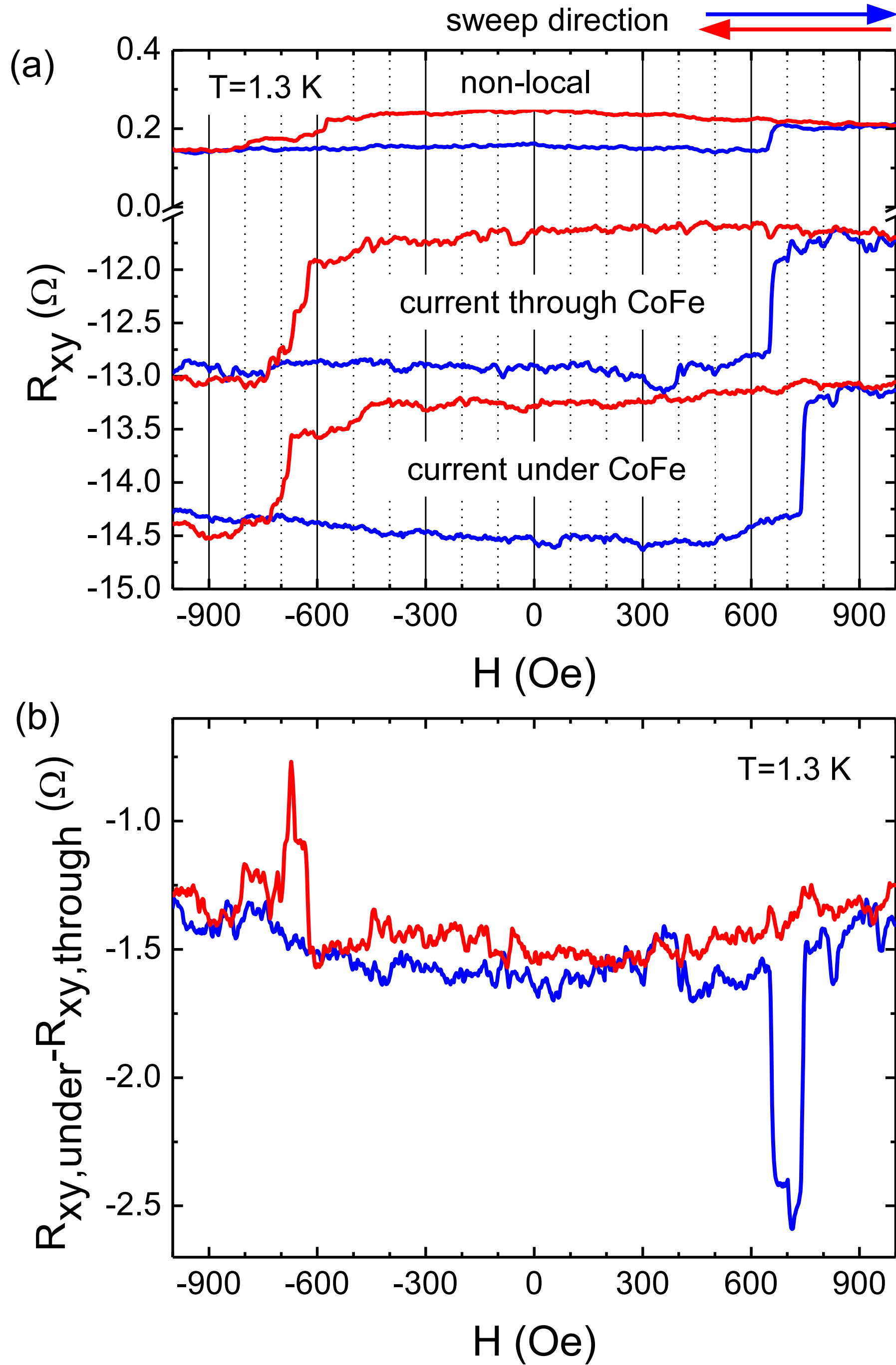

Figure 6.9: (a) Comparison of switching fields measured in near Hall cross with different measurement configuration. The switching field of non-local in which current flow through the CoFe is comparable to local Hall signal with current through the CoFe. (b) The subtraction of bottom two traces of (a) shows the difference of the switching fields of local Hall signals with different current applications.

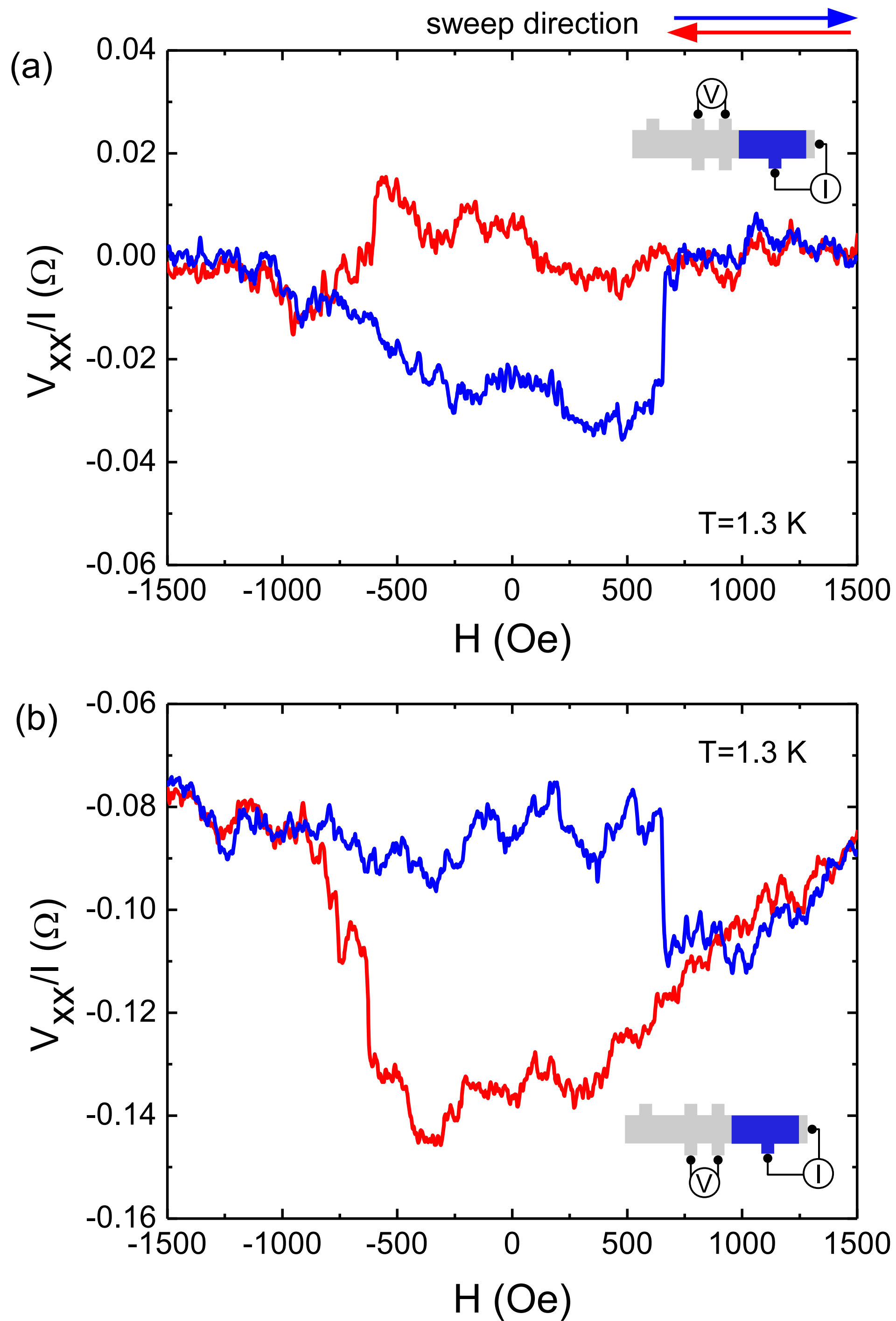

Figure 6.10: Non-local MR with in-plane H measured at the top contacts (a) and the bottom contacts (b).

detecting the ISHE. Because the spin can not reach the far contacts, which are separated by about 10 μm from the CoFe electrode, the far contacts are maintained at constant potential. Since the potential difference between the two far contacts is likely negligible, the non-local Hall measurement is the same as the difference of two non-local MR signals. Fig. 6.11 (b) presents the result of subtracting the non-local MR measured at the top contacts and bottom contacts. The traces of Fig. 6.11 (b) are comparable to the non-local Hall signal shown in Fig. 6.8, with a switching field of 650 Oe and $R_{xx,top} - R_{xx,bottom}$ of 0.09 Ω.

6.2.4 Hall Measurement with Perpendicular Field

Fig. 6.12 presents the non-local Hall measurement results with a perpendicular magnetic field swept from -1000 Oe to 1000 Oe. A current of 10 μA is applied through the CoFe/InSb interface. The CoFe electrode is first magnetized with in-plane magnetic field of ±10000 Oe, then the sample is tilted by 90° for the perpendicular field sweep. The arrows in the insets of Fig. 6.12 represent the directions of the CoFe magnetization. The top and the bottom insets represent the positive and negative directions of magnetization, respectively. The measured signals of both positive and negative magnetization of the CoFe have a sweep direction dependence. At zero field, the maximum amplitudes of 0.3 Ω are present for both top and bottom plots. As we discussed in Sec. 5.2.2, the spin precession here may also cause the signals. Due to a critical field of $H_c \approx 300$ Oe, we think the signals have the same origin as non-local LSV.

In conclusion, in this chapter, Hall and MR signals are measured locally and non-locally in InSb/CoFe Hall devices. The ferromagnetic CoFe contributes to the Hall signals by its fringing field and to the MR signal through a reduction in WAL. The non-local MR signals show asymmetric behavior, which is the evidence of spin phenomena The non-local Hall signals shows a switching behavior due to the CoFe magnetization switching at its coercive field. However, it is not sure whether the detected signal is the spin Hall effect or a fringing field effect. The non-local Hall signals in a perpendicular field show a critical field behavior similar to LSVs.

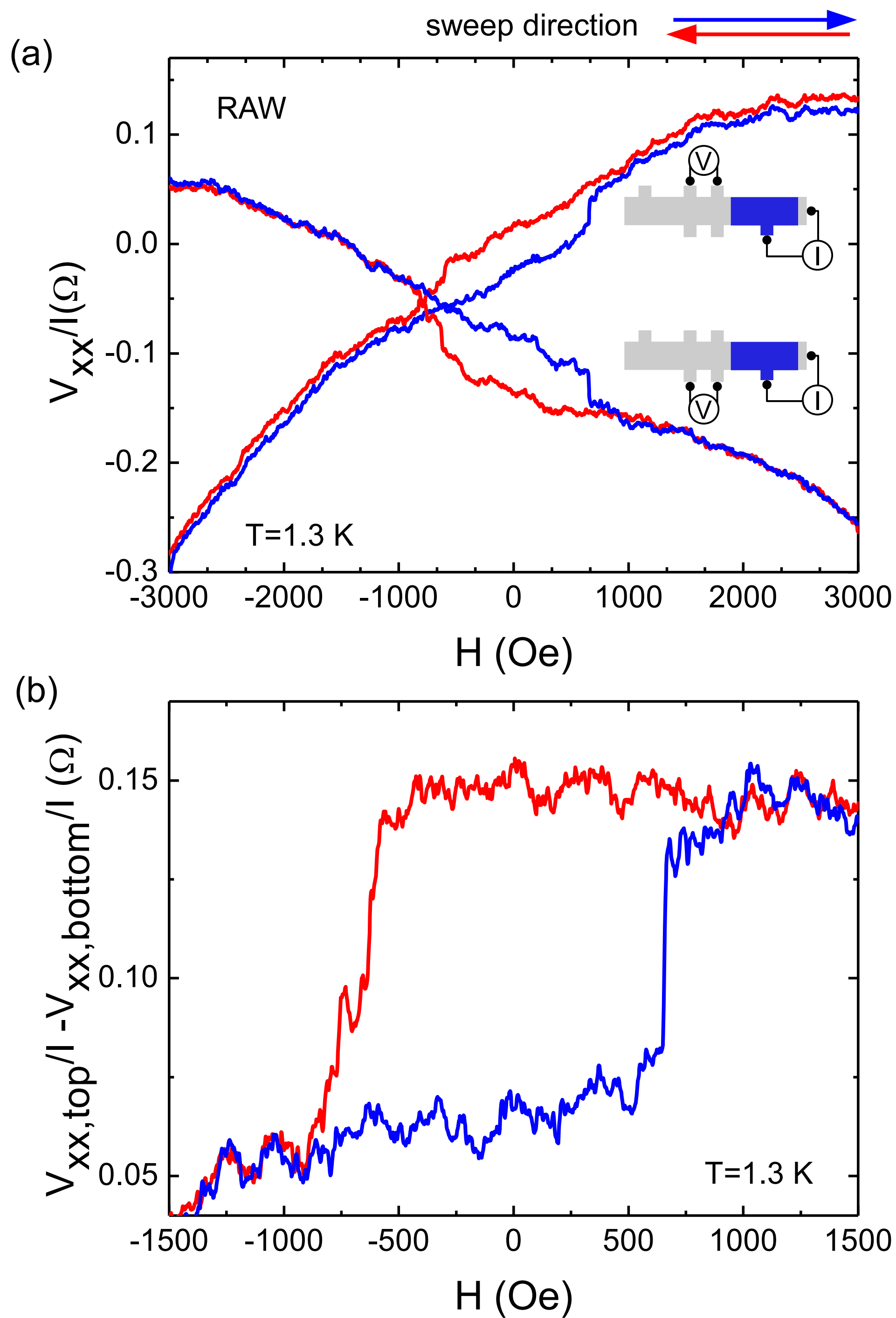

Figure 6.11: (a) Raw data of the non-local MR measured in top contacts and bottom contacts. (b) Signal difference of top contacts and bottom contacts.

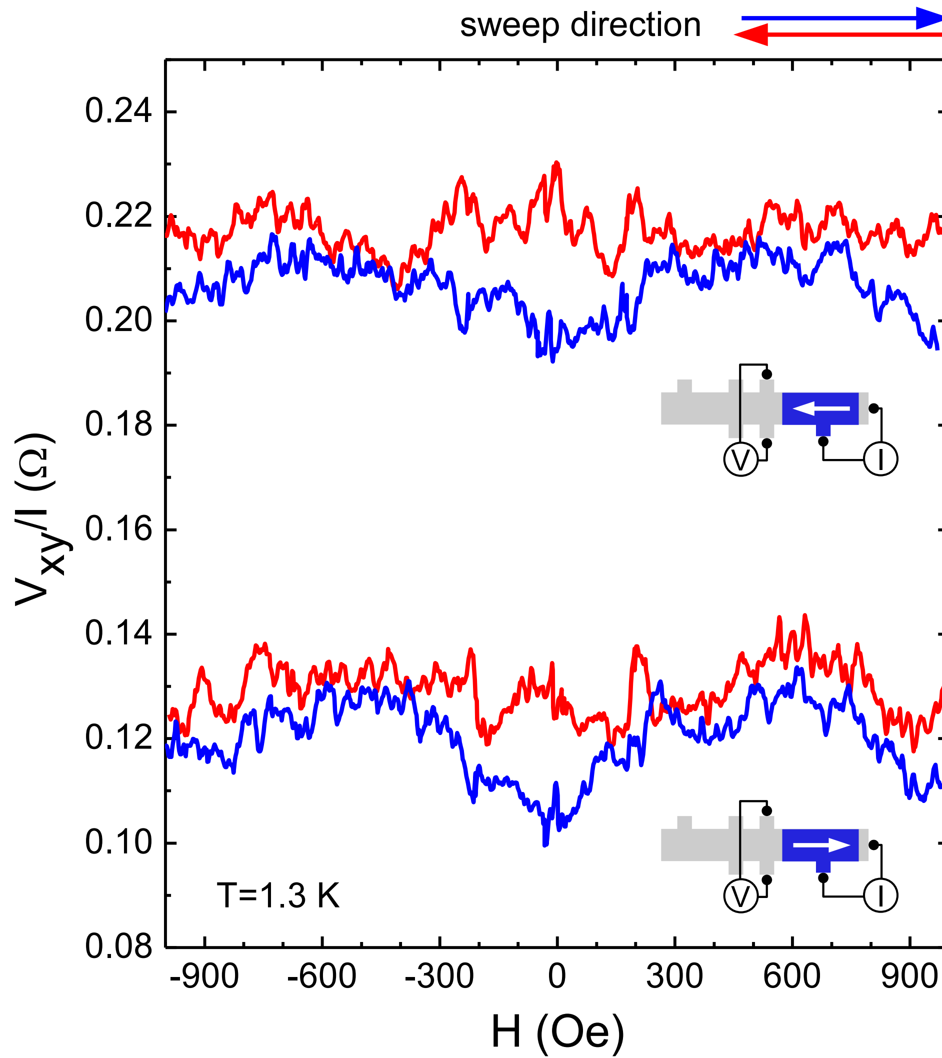

Figure 6.12: Hall resistance under perpendicular magnetic field with magnetized CoFe. CoFe magnetized at in-plane high field which is indicated with white arrows in measurement schematic.

Chapter 7

Inverse Spin Hall Effect in InSb with CoFe Electrodes

7.1 Device Design and Fabrication

In Sec. 6.2.2 and Sec. 6.2.3, the contribution of the inverse spin Hall effect to the non-local Hall and non-local MR signals is uncertain due to the presence of fringing fields. Thus, a simpler device is fabricated, which aims to remove the fringing field, and is expected to better isolate the inverse spin Hall effect. Type A InSb is patterned by EBL and etching. And then, 120 nm of SiO layer is patterned by photolithography, while 55 nm of CoFe and 80 nm of Au are patterned by EBL. The micrograph of ISHE device and lithographical dimensions are shown in Fig. 7.1 (a) and (b), respectively. Fig. 7.1(b) indicates the device contact number, the device geometry with a cartesian coordinate and (c) shows a schematic of the magnetic field tilted to angle ϕ. The I-V trace (Fig. 7.1 (d)) indicates the Ohmic characteristic of CoFe/InSb interface in the device.

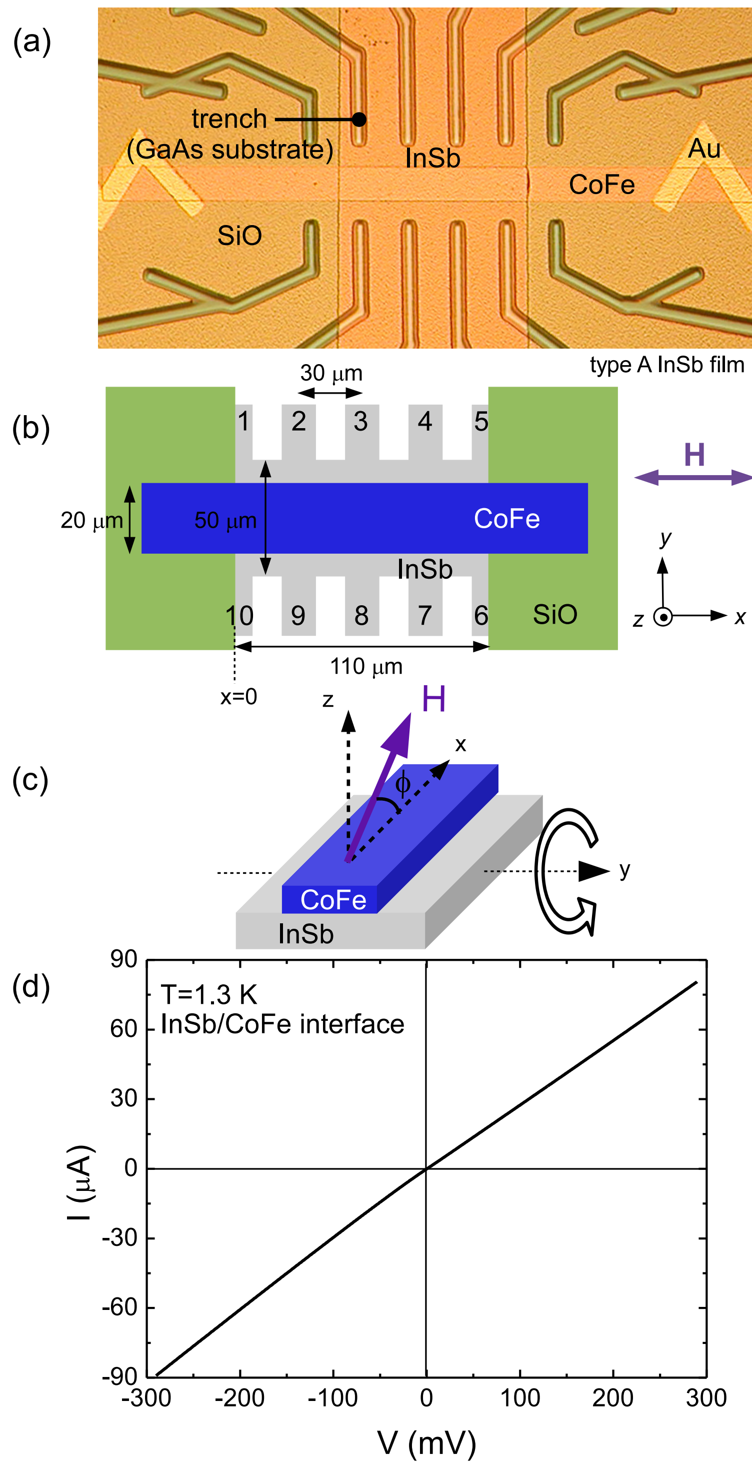

Figure 7.1: (a) Micrograph of spin Hall device. (b) Lithographic dimensions. (c) Schematic diagram of tilted external magnetic field. (d) I-V data of CoFe/InSb interface.

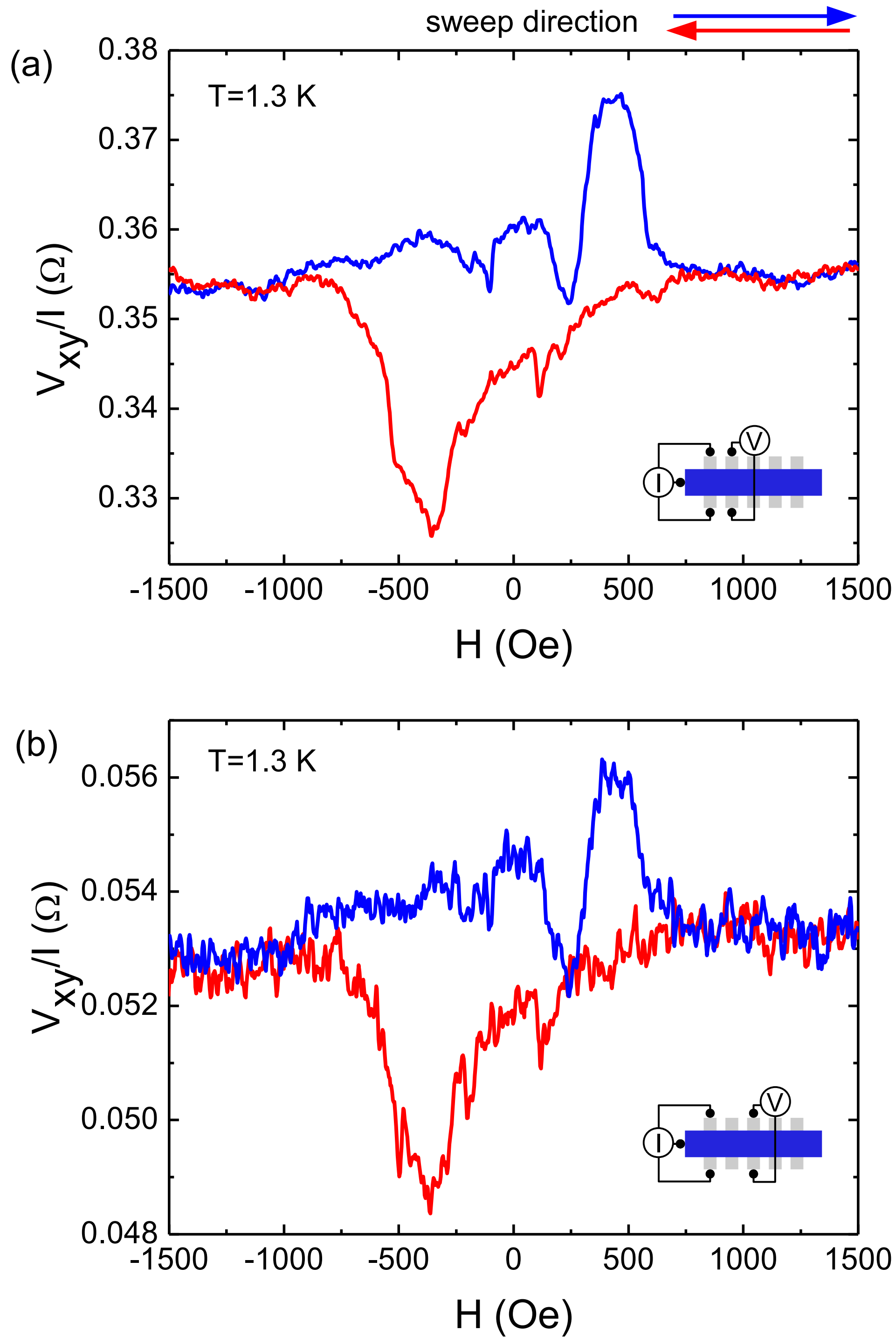

Figure 7.2: Spin Hall geometry data with in-plane external magnetic field measured at different Hall crosses; (a) close and (b) far.

7.2 Inverse Spin Hall Effect Measurement

7.2.1 Hall Measurement with In-Plane Field

In the insets of Fig. 7.2 (a) and (b) the measurement configurations are depicted (see also Fig. 7.1 (b)). A 10 μA current is applied from the CoFe electrode to the InSb contacts 1 and 10. This allows for a symmetric distribution of current about the $\hat{x}$-axis in order to minimize a parasitic MR due to misalignment. An in-plane magnetic field is applied along the CoFe electrode and swept from -5000 Oe to 5000 Oe. The Hall signal between contacts 2 and 9 is displayed in Fig. 7.2 (a). The Hall slopes are subtracted for clarity. Depending on the magnetic field sweep direction, R_{xy} is increased and decreased for the forward (blue) and backward (red) sweeps , respectively. The signal amplitudes (ΔR_{xy}) are 21 mΩ and 25 mΩ for the forward and the backward sweeps, respectively. Using contacts 3 and 8 with the same current configuration, similar signals are measured with the same features as shown in Fig. 7.2 (b). The ΔR_{xy} is 3 mΩ and 4 mΩ for the forward and the backward sweeps, respectively. In this non-local measurement configuration, the signals for contacts 3 and 8 are about 7 times smaller than those of contacts 2 and 9. However, the relative signals ($\Delta R_{xy}/R_0$) are comparable: 5.8% (forward) and 7.7% (backward) for contacts 2 and 9, while for contacts 3 and 8, they are 5.8% (forward) and 8.3% (backward).

7.2.2 Hall Measurement with Tilted Field

The Hall slope of the ϕ=90° data measured between contacts 3 and 8 is shown in Fig. 7.3 (a) and provides information on the injected current. Due to higher electron density of CoFe, $\sim$1.5 $\times 10^{28}$ m^{-3}, the contribution of current in CoFe to the Hall slope is negligible. Therefore, the current in InSb dominantly contributes to the Hall slope, which is the injected current from CoFe to InSb. The extracted Hall slope from the 90° data between contacts 3 and 8 ($x \sim$55 μm: distance from x=0) is -1.92×10^{-9} V/Oe. With Eq. 3.1 and n=0.65$\times10^{22}$ m^{-3} for the type A InSb film, the calculated current is 26 nA which is 0.26% of total injected current. Since the sign of the Hall slope is negative, the direction of the current in the InSb is $-\hat{x}$ and the direction of the current in the CoFe electrode is $+\hat{x}$. Therefore, 0.26% of the applied current is injected between $\sim$45 μm$< x <$ 110 μm. Due to the fact that the CoFe electrode and InSb form an Ohmic interface, as observed in I-V measurement in Fig. 7.3, most of the current is injected at x=0. On the other hand, the 90° Hall slope is also

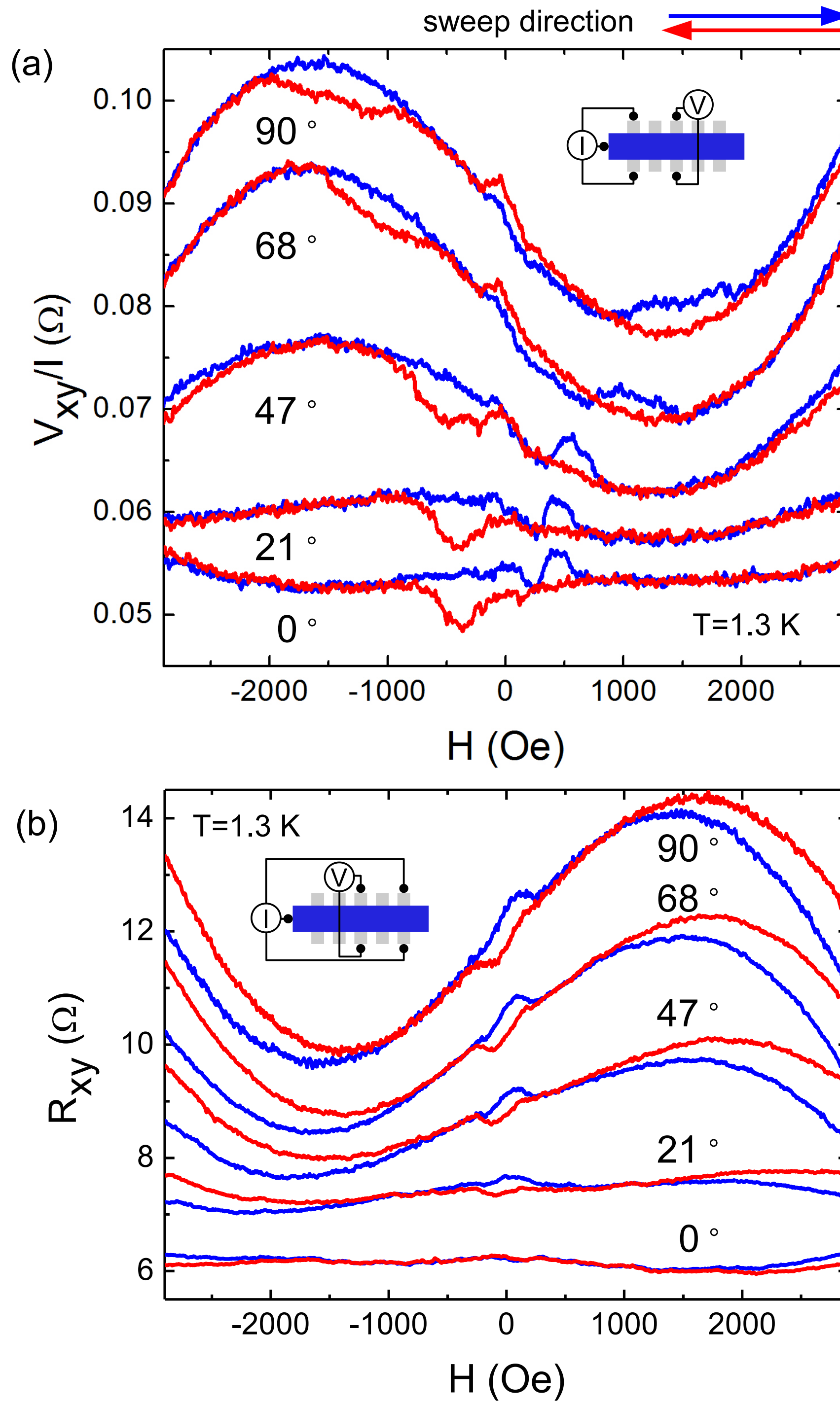

Figure 7.3: Tilting angle ϕ dependence of spin Hall signal measured in different current applications (blue: forward sweep, red: backward sweep).

measured between contacts 3 and 8 with a different current configuration. A 1 μA current is applied from the CoFe to contacts 5 and 6 as depicted in inset of Fig. 7.3 (b). From the extracted Hall slope of 7.0×10^{-8} V/Oe, 95% of applied current is now injected between $\sim$0 μm$< x <$ 65 μm.

Due to the structure of the device, the spin current direction is in $\hat{z}$ and the direction of the spin induced by the CoFe electrode is $\hat{x}$. By the inverse spin Hall relation (Eq. 6.2), the direction of the induced current is in $\hat{y}$. The resulting potential difference between the contacts along in $\hat{y}$-direction depends on the direction of the CoFe magnetization. Although, the Hall signals shows the magnetization dependence as expected, the signal features are not simply consistent with our expectation based on Eq. 6.2. From the magnetic field tilting experiments on this device (Fig. 7.3 (a)) the signal is dependent on the in-plane magnetic field. As the tilting angle increase, the signals shift to higher field, which is due to the decrease of the magnitude of in-plane field, $H= H_{\text{in-plane}}/\cos\phi$. The $1/\cos\phi$ relation between the applied field and the in-plane field explain the in-plane field dependence of our signal as depicted in Fig. 7.4. The R_{xy} peaks at 300-500 Oe are dependent on the direction of the magnetization. The maximum and minimum occur when the magnetization switches. However, for the other measurement configuration (local measurement) as shown in Fig. 7.3 (b), the signals do not shift when the angle increases. The signal appears at 21° and remaining at the same H for tilting angles. Note that the signal H_c $\sim$300 Oe is the same critical magnetic field observed in the other devices.

7.2.3 Relation to the Inverse Spin Hall Effect

On both measurements, the signals disappear at high field with critical field H_c. For the non-local measurement, as depicted in the inset of Fig. 7.3 (a), the signals respond to the in-plane field. On the other hand, the local measurement, as depicted in Fig. 7.3 (b), the signal is evident only when a perpendicular field is applied. Important extracted information from the two measurements are the current directions in the InSb Hall contacts. The slopes of the background signals of both measurements are consistent with the current directions we have calculated. However, as designed for, the device drives the current in $\hat{z}$-direction from CoFe to InSb, which needs to be considered in the non-local measurement shown in Fig. 7.3 (a). We observe an in-plane magnetic field dependence in the non-local Hall measurement, and a perpendicular magnetic field dependence in the local Hall measurement. We think the signal originates from a spin current due to the observation of H_c together with hysteresis. The signal in Fig. 7.3 (a) is consistent with the inverse spin Hall effect,

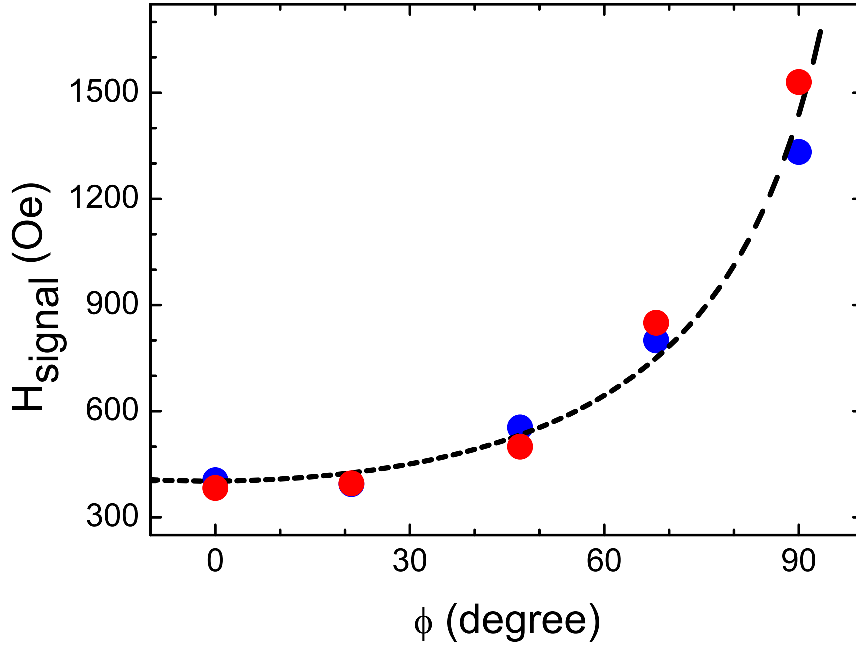

Figure 7.4: H_{signal} depends on the tilt angle (blue:forward sweep, red:backward sweep and black dashed line: $1/\cos\phi$ fit).

although an origin in a Hall effect due to fringing fields cannot be excluded. The small value of the charge current at the location of the Hall measurement also supports an inverse spin Hall origin for Fig. 7.3 (a). The fact that a signal only appears at close to perpendicular fields in Fig. 7.3 (b) may be related to spin precession in this geometry. Yet, the relative independence of critical field on tilting in Fig 7.3 (b) is reminiscent of the interface MR, while the sign change on sweep direction change is not. The interpretation in terms of the inverse spin Hall effect of Fig. 7.3 (b) is hence less certain.

Chapter 8

Summary

Spintronics is considered as a candidate for future electronics. Keys to the realization of semiconductor-base spintronic devices lie in how to overcome obstacles such as spin-polarized electron injection into semiconductors with high efficiency, manipulation of spin carriers in semiconductors, and electrical detection of electron spin in semiconductors. In this dissertation, we present our studies for spin injection into the high mobility, strong spin-orbit coupled semiconductor InSb from ferromagnetic material CoFe. Two InSb films with different electron density (type A: $n = 0.65 \times 10^{22}$ m^{-3}, type C: $n = 8.9 \times 10^{22}$ m^{-3}) are used for our research. The spin coherence lengths (type A: 1.5 μm, type C: 1.2 μm) of two films are characterized by AL, and provide the guidelines for our device fabrication. The InSb/CoFe devices are fabricated with photolithograpy, electron beam lithography, wet etching, and thermal deposition techniques. The low temperature Hall and MR measurements are performed in ^{4}He cryostat with lockin techniques in the presence of external magnetic field. The Hall measurements of fringing fields of CoFe and the approximate magnetic model provide magnetic properties of $Co_{60}Fe_{40}$ electrode such as magnetization switching field and saturation magnetization (1.7×10^6 A/m) in μm scale geometry. The interface MR measurements of InSb/CoFe presents a unique signal having magnetic field symmetric behavior with critical field H_c, weak in-plane angle dependence, and strong temperature dependence. Based on the analysis on the two important factors which are the temperature dependence and the magnetization, we attribute our signal to a ferromagnetic phase induced by spin injection. In the nonlocal lateral spin valve (LSV) measurement, the detected signals are considered to be the spin current signals from five observations which are listed below. Firstly, the signal features of the LSV are the same as the interface magnetoresistance (MR)

results. The H_c of the LSV signals are in the same range as the H_c of interface MR signals. Secondly, the non-local LSV signals are strongly dependent on the temperature in the range of 1.2-3.5 K, a unique characteristic of the interface MR. Thirdly, the injector bias dependence in non-local geometry is the signature of the pure spin current. Fourthly, the signals are dependent on the exact interfaces, which is shown in the results of the injector and the detector exchanged configurations. Lastly, the non-local LSV signals with the magnetized CoFe are dependent on the perpendicular magnetic field, which could be due to spin precession. The Hall and the MR signals are measured locally and non-locally in InSb/CoFe Hall devices. The ferromagnetic CoFe shows the contributions to the Hall signals by fringing field and to the MR signal. The non-local MR signals shows asymmetric behavior which is evidence of spin phenomena. The non-local Hall signals present the switching behavior due to the CoFe magnetization switching at the coercive field, however, it is not sure whether the detected signal is spin Hall effect or fringing field effect. The non-local Hall signals with the perpendicular field show the same H_c as the non-local LSVs. In inverse spin Hall effect measurement in InSb/CoFe Hall device, a non-local and local Hall measurement are performed. The tilted magnetic field measurement presents an in-plane H dependence in the non-local Hall measurement and a perpendicular H dependence in the local Hall measurement. From the properties of the critical field H_c and the observed hysteresis, it can be assumed that an injected spin current lies at the origin of these observations.

Bibliography

[1] G. A. Prinz, Science **282**, 1660 (1998).

[2] W. Thompson, Proc. R. Soc. London **8**, 546 (1856).

[3] P. Grünberg, R. Schreiber, Y. Pang, M. B. Brodsky, and H. Sowers, Phys. Rev. Lett. **57**, 2442 (1986).

[4] M. N. Baibich, J. M. Broto, A. Fert, F. N. Van Dau, F. Petroff, P. Etienne, G. Creuzet, A. Friederich, and J. Chazelas, Phys. Rev. Lett. **61**, 2472 (1988).

[5] S. A. Wolf, D. D. Awschalom, R. A. Buhrman, J. M. Daughton, S. Von Molnar, M. L. Roukes, A. Y. Chtchelkanova, and D. M. Treger, Science **294**, 1488 (2001).

[6] B. Dieny, V. S. Speriosu, S. Metin, S. S. P. Parkin, B. A. Gurney, P. Baumgart, and D. R. Wilhoit, J. Appl. Phys. **69**, 4774 (1991).

[7] J. S. Moodera, L. R. Kinder, T. M. Wong, and R. Meservey, Phys. Rev. Lett. **74**, 3273 (1995).

[8] T. Miyazaki and N. Tezuka, J. Magn. Magn. Mater. **139**, L231 (1995).

[9] M. Julliere, Physics Letters A **54**, 225 (1975).

[10] L. Chua, Appl. Phys. A: Materials Science & Processing **102**, 765 (2011).

[11] J. Åkerman, Science **308**, 508 (2005).

[12] J. M. Kikkawa and D. D. Awschalom, Phys. Rev. Lett. **80**, 4313 (1998).

[13] S. Datta and B. Das, Appl. Phys. Lett. **56**, 665 (1990).

[14] A. Filip, B. Hoving, F. Jedema, B. Van Wees, B. Dutta, and S. Borghs, Phys. Rev. B **62**, 9996 (2000).

[15] B. T. Jonker, O. M. van't Erve, G. Kioseoglou, A. T. Hanbicki, C. H. Li, M. Holub, C. Awo-Affouda, and P. E. Thompson, in *Electron Devices Meeting (IEDM), 2009 IEEE International* (IEEE, 2009), pp. 1–2.

[16] S. Crooker, M. Furis, X. Lou, C. Adelmann, D. Smith, C. Palmstrøm, and P. Crowell, Science **309**, 2191 (2005).

[17] M. Johnson and R. H. Silsbee, Phys. Rev. Lett. **55**, 1790 (1985).

[18] R. Godfrey and M. Johnson, Phys. Rev. Lett. **96**, 136601 (2006).

[19] T. Kimura, J. Hamrle, and Y. Otani, Phys. Rev. B **72**, 014461 (2005).

[20] T. Valet and A. Fert, Phys. Rev. B **48**, 7099 (1993).

[21] O. Madelung, Semiconductors: Data Handbook p. 3rd ed (Springer, Berlin, 2004).

[22] G. Bergmann, Phys. Rep. **107**, 1 (1984).

[23] R. L. Kallaher and J. J. Heremans, Phys. Rev. B **79**, 075322 (2009).

[24] D. L. Partin, M. Pelczynski, P. Cooke, J. Green, J. Heremans, and C. M. Thrush, J. Cryst. Growth **195**, 378 (1998).

[25] P. W. Anderson, Phys. Rev. **109**, 1492 (1958).

[26] S. I. Kobayashi and F. Komori, Prog. Theor. Phys. Supplement pp. 224–248 (1985).

[27] Z. Ovadyahu and Y. Imry, Phys. Rev. B **24**, 7439 (1981).

[28] S. Hikami, A. I. Larkin, and Y. Nagaoka, Prog. Theor. Phys. **63**, 707 (1980).

[29] F. G. Monzon, M. Johnson, and M. L. Roukes, Appl. Phys. Lett. **71**, 3087 (1997).

[30] M. Johnson, B. R. Bennett, M. J. Yang, M. M. Miller, and B. V. Shanabrook, Appl. Phys. Lett. **71**, 974 (1997).

[31] D. J. Monsma and S. S. P. Parkin, Appl. Phys. Lett. **77**, 720 (2000).

[32] D. V. Berkov, C. T. Boone, and I. N. Krivorotov, Phys. Rev. B **83**, 054420 (2011).

[33] X. Lou, C. Adelmann, M. Furis, S. Crooker, C. Palmstrøm, and P. Crowell, Phys. Rev. Lett. **96**, 176603 (2006).

[34] R. Jansen and B. C. Min, Phys. rev. lett. **99**, 246604 (2007).

[35] S. A. Solin, T. Thio, D. R. Hines, and J. J. Heremans, Science **289**, 1530 (2000).

[36] H. Saito, S. Yuasa, and K. Ando, Phys. Rev. Lett. **95**, 86604 (2005).

[37] C. Gould, C. Rüster, T. Jungwirth, E. Girgis, G. M. Schott, R. Giraud, K. Brunner, G. Schmidt, and L. W. Molenkamp, Phys. Rev. Lett. **93**, 117203 (2004).

[38] J. Moser, A. Matos-Abiague, D. Schuh, W. Wegscheider, J. Fabian, and D. Weiss, Phys. Rev. Lett. **99**, 056601 (2007).

[39] A. Matos-Abiague and J. Fabian, Phys. Rev. B **79**, 155303 (2009).

[40] T. Uemura, M. Harada, T. Akiho, K. Matsuda, and M. Yamamoto, Appl. Phys. Lett. **98**, 102503 (2011).

[41] M. Ziese and S. P. Sena, J. Phys.: Condens. matter **10**, 2727 (1998).

[42] B. L. Altshuler and A. G. Aronov, Solid State Commun. **88**, 1033 (1993).

[43] R. P. Peters, G. Bergmann, and R. M. Mueller, Phys. Rev. Lett. **58**, 1964 (1987).

[44] G. Bergman, Phys. Rev. Lett. **48**, 1046 (1982).

[45] L. P. Rokhinson, Y. Lyanda-Geller, Z. Ge, S. Shen, X. Liu, M. Dobrowolska, and J. K. Furdyna, Phys. Rev. B **76**, 161201 (2007).

[46] S. Von Molnar and D. Read, Proceedings of the IEEE **91**, 715 (2003).

[47] O. van't Erve, C. Awo-Affouda, A. Hanbicki, C. Li, P. Thompson, and B. Jonker, Electron Devices, IEEE Trans. on **56**, 2343 (2009).

[48] X. Lou, C. Adelmann, S. Crooker, E. Garlid, J. Zhang, K. Reddy, S. Flexner, C. Palmstrøm, and P. Crowell, Nat. Phys. **3**, 197 (2007).

[49] H. C. Koo, H. Yi, J. B. Ko, J. Chang, S. H. Han, D. Jung, S. G. Huh, and J. Eom, Appl. Phys. Lett. **90**, 022101 (2007).

[50] H. C. Koo, J. H. Kwon, J. Eom, J. Chang, S. H. Han, and M. Johnson, Science **325**, 1515 (2009).

[51] M. Ciorga, A. Einwanger, U. Wurstbauer, D. Schuh, W. Wegscheider, and D. Weiss, Phys. Rev. B **79**, 165321 (2009).

[52] P. Hammar, B. Bennett, M. Yang, and M. Johnson, Phys. Rev. Lett. **83**, 203 (1999).

[53] F. J. Jedema, H. B. Heersche, A. T. Filip, J. J. A. Baselmans, and B. J. Van Wees, Nature **18**, 713 (2002).

[54] T. Kimura, J. Hamrle, Y. Otani, K. Tsukagoshi, and Y. Aoyagi, Appl. Phys. Lett. **85**, 3795 (2004).

[55] M. Johnson, Electron Devices, IEEE Trans. on Electron Devices **54**, 1024 (2007).

[56] L. Gao, X. Jiang, S. H. Yang, J. D. Burton, E. Y. Tsymbal, and S. S. P. Parkin, Phys. Rev. Lett. **99**, 226602 (2007).

[57] G. Schmidt, D. Ferrand, L. W. Molenkamp, A. T. Filip, and B. J. van Wees, Phys. Rev. B **62**, R4790 (2000).

[58] E. I. Rashba, Phys. Rev. B **62**, R16267 (2000).

[59] V. Dugaev, P. Bruno, and J. Barnas, Phys. Rev. B **64**, 144423 (2001).

[60] J. Hirsch, Phys. Rev. Lett. **83**, 1834 (1999).

[61] Y. Kato, R. Myers, A. Gossard, and D. Awschalom, Science **306**, 1910 (2004).

[62] J. Inoue and H. Ohno, Science **309**, 2004 (2005).

[63] J. N. Chazalviel, Phys. Rev. B **11**, 3918 (1975).

[64] G. E. W. Bauer, Science **306**, 1898 (2004).

[65] K. Ando and E. Saitoh, Nat. Commun. **3**, 629 (2012).

[66] S. O. Valenzuela and M. Tinkham, Nature **442**, 176 (2006).

[67] S. O. Valenzuela and M. Tinkham, J. Appl. Phys. **101**, 09B103 (2007).

[68] T. Seki, Y. Hasegawa, S. Mitani, S. Takahashi, H. Imamura, S. Maekawa, J. Nitta, and K. Takanashi, Nat. Mater. **7**, 125 (2008).